TIRC 1 – Cornell University Research Consortium

January 2009

Project Title: **Concrete Deck Material Properties**

RFP No.: **SPR Project C-02-03**
New York State Department of Transportation

Final Report

Principal Investigators:

Kolluru Subramaniam
Civil Engineering Department
Grove School of Engineering
Convent Avenue at 140th Street
The City College/ City University of New York
New York, NY 10031
Tel. (212) 650-6569, Fax. (212)650-6965
E-mail: ksubram@ce.ccny.cuny.edu

Anil K. Agrawal
Civil Engineering Department
Grove School of Engineering
Convent Avenue at 140th Street
The City College/ City University of New York
New York, NY 10031
Tel. (212) 650-8442, Fax. (212)650-6965
E-mail: Agrawal@ccny.cuny.edu

1. Report No. **C-02-03**	2. Government Accession No.	3. Recipient's Catalog No.
4. Title and Subtitle Concrete Deck Material Properties		5. Report Date **January, 2009**
		6. Performing Organization Code
7. Author(s) **Kolluru V. Subramaniam and Anil Agrawal**		8. Performing Organization Report No. **RF 75469**
9. Performing Organization Name and Address **City College of New York, New York, NY 10031**		10. Work Unit No.
		11. Contract or Grant No.
12. Sponsoring Agency Name and Address **NYS Department of Transportation 50 Wolf Road Albany, New York 12232**		13. Type of Report and Period Covered **Final Report**
		14. Sponsoring Agency Code

15. Supplementary Notes
Project funded in part with funds from the Federal Highway Administration

16. Abstract

The two-fold focus of this study was (a) to develop an understanding of the mechanisms responsible for causing cracking in the concrete; and (b) to study the influence of the local materials on the performance of NYSDOT's HP concrete mixture. Recommendations for minimizing the premature cracking in HP concrete decks related to restrained volumetric contraction are developed from the results of this investigation. It is important to reduce the total temperature rise and the temperature gradient across the steel girder to minimize the level of tensile stress in concrete in the first few days after casting, while the concrete goes through the heating and cooling produced by hydration heat. The local materials for use in HP concrete should be carefully evaluated. The type of coarse aggregate used in the mixture produces significant differences in the strength and elastic modulus of concrete. Differences in cementitious material contribute to significant differences in autogenous and drying shrinkage. Recommendations pertaining to cementitious materials are: (a) If silica fume is used, it should only to be added separately to the mix, unless the reactivity of blended silica fume is established and found comparable to silica fume addition; (b)Only the use of Type I/II or Type II cement should be permitted; and (c) When ground granulated blast furnace slag is used, it should be evaluated to ensure that it does not provide high early reactivity.

17. Key Words **Cracking, restrained shrinkage, early-age, concrete deck**		18. Distribution Statement **No Restrictions**		
19. Security Classif. (of this report) **Unclassified**		20. Security Classif. (of this page) **Unclassified**	21. No. of Pages 120	22. Price

Form DOT F 1700.7 (8-72)

Table of Contents

Executive Summary

New York State Department of Transportation (NYSDOT) has adopted a high performance (HP) concrete mix for bridge decks, which was developed with the objective of improving performance and durability of bridge decks. However, premature cracking, which was not load-induced, has been reported in some bridge decks. Cracks in a bridge deck often lead to premature deterioration resulting from corrosion of the steel reinforcement, which is associated with a dramatic reduction in the service life and an increase in the life-cycle maintenance costs. While the mixture composition for HP concrete has been standardized, variations in the composition and properties of the local materials used in making the HP concrete contribute to variations in concrete properties, which has a direct impact on its performance. An investigation of causes of cracking related to local materials in cast-in place High Performance (HP) concrete bridge decks in NY is presented in this report.

The two-fold focus of this study is (a) to develop an understanding of the mechanisms responsible for causing cracking in the concrete; and (b) to study the influence of the local materials on the performance of concrete. A three-phase work plan, where each phase addressed a specific aspect of the problem was developed and implemented.

Phase I – This phase of the project dealt with evaluating the in-situ properties of concrete in existing bridge decks. From an investigation involving surveying and testing cores obtained from bridge decks a qualitative assessment of the cracking as it relates to in-situ concrete properties was developed.

Phase II – Comprised of monitoring the response of HP Concrete in newly constructed bridges. From the analysis of strain and temperature data recorded from steel girder and concrete decks an understanding of the role of the different mechanisms which contribute to stress development in concrete deck was developed.

Phase III – In this phase of project, a laboratory evaluation of the HP concrete, using local materials from different regions of NYSDOT was performed to evaluate the influence of local materials on the potential for restrained cracking.

Since the three phases deal with disparate aspects of evaluating HP concrete performance, the findings of each Phase of work are described separately.

Phase I

- The in-place HP concrete obtained from bridge decks provided compressive strengths in excess of the design value (3000psi).

- The HP concrete in all the bridge decks has a relatively high tensile strength. The tensile strength of concrete in all the bridge decks tested was higher than 660psi.

- The transverse cracking in the HP decks is likely formed at an early age, when the strength of the mortar is smaller than the strength of the aggregate. In mature concrete, the mortar is stronger than the aggregate resulting in aggregate fracture under tensile loading.

- High temperature at the time of placement appears to favor cracking.

- There are no discernable trends between factors such as the span length, girder spacing, the presence of shear keys etc. and the type of cracking observed on the bridge decks.

Phase II

- Thermal effects are important in the first 48 hours after casting. There is a differential movement between concrete deck and steel girder in this period. Full strain compatibility between concrete deck and steel girder is achieved in the first 48 hours following the initial temperature rise and cooling.

- Restraint to thermal contraction/expansion of concrete is significantly smaller than the restraint to shrinkage, which occurs immediately after setting and continues to increase monotonically with time.

- Concrete deck movement in the period associated with cooling following the initial temperature rise is restrained, which could potentially produce tensile stress in concrete. The magnitude of tensile stress at the end of the cooling period depends upon the total temperature rise and the temperature gradient in the steel girder at the end of the heating period.

Phase III

Differences in the <u>aggregate and the cementitious material</u> contribute to significant differences in the development of material properties and potential for restrained shrinkage cracking.

- A larger temperature rise in the first day after mixing is associated with a larger magnitude of residual stress when the concrete reaches thermal equilibrium with the environment. The residual stress at one day contributes significantly to the total magnitude of the stress produced by restrained shrinkage.

- The potential for restrained shrinkage cracking would increase when (a) *there is a rapid increase in elastic modulus concurrent with an increase in shrinkage*; or (b) *the increase in the shrinkage strain occurs when the material has a high elastic modulus*.

Recommendations for minimizing the premature cracking in HP concrete decks related to restrained volumetric contraction are developed from the results of this investigation.

- It is important to reduce the total temperature rise and the temperature gradient across the steel girder to minimize the level of tensile stress in concrete in the first few days after casting, while the concrete goes through the heating and cooling produced by hydration heat. This would decrease the level of tensile stress in concrete due to restrained thermal movement.

- The local materials should be carefully evaluated before use in HP concrete. If silica fume is used, it should only to be added separately to the mix, unless the reactivity of blended silica fume is established and found comparable to silica fume addition. Only the use of Type I/II or Type II cement should be permitted. When ground granulated blast furnace slag is used, it should be evaluated to ensure that it does not provide high early reactivity.

Section 1: Introduction

1.1 Background

Numerous concrete bridge decks have been constructed throughout the state of New York, the vast majority of which have been observed to provide acceptable performance and service life. However, some concrete decks have been observed to crack prematurely [Alampalli and Owens 2000]. Cracking in bridge decks can be traced to loading or material related causes. Load-induced tensile cracking in bridge decks happens at places of high stress which are easy to identify, such as, the areas of high negative moment [Prenger 1992, Ramey et al. 1997]. The premature cracking observed in the bridge decks was of a nature and at locations, which suggests reasons not directly related load-induced stresses [Alampalli and Owens 2000].

Cracking in bridge deck often leads to premature deterioration; cracks accelerate deterioration by permitting the ingress of aggressive agents thereby producing corrosion of the steel reinforcement. Therefore cracking often results in a dramatic reduction in the service life and an increase in the life-cycle maintenance costs.

Concrete bridge decks have been designed primarily on the basis of strength/stiffness related issues alone. It is now becoming evident that strength does not provide sufficient information to identify when early-age cracking may have a high potential for occurring [Waszczuk 1999]. For example, higher strength concrete containing silica fume is often thought to automatically provide improved performance, however, sensitivity to environmental conditions at early-ages may make these mixtures extremely susceptible to cracking [Shah et al 1998]. Increasing evidence suggests that cracking in bridge decks occurs at an early age for causes not directly related to strength development but due to restrained thermal contraction and shrinkage of concrete. It has been shown that when free contraction of concrete is retrained, the magnitude of tensile stress is relatively high compared to traffic loading-induced stress [William et al. 2005]. Cracking results when the tensile stress due to restrained volume changes exceeds the tensile strength of concrete. Cracking resulting from restrained shrinkage and thermal contraction of concrete produces an extensive network of cracks over the entire deck. These cracks usually develop into full-depth cracks.

Early-age cracking in bridge decks due to restrained shrinkage and thermal contraction has been attributed to both material and structural effects [French et al. 1999, Issa 1999, Krauss and Rogalla 1996]. Many factors which contribute to development of tensile stresses have been identified: (a) constraining effects of abutments; (b) non-uniform curing of concrete along the bridge deck; and (c) in-plane and through-thickness temperature variation along the deck. Cracks have been observed when the heat of hydration produces large temperature gradients within the concrete [Issa 1999]. William et al. (2005) suggest that constrained shrinkage is the prime cause for elevated longitudinal stresses and ultimately responsible for crack initiation within the first two days after concrete placement. From a study involving forty bridge decks, it was concluded that the material effects which contribute to increased cracking include increasing slump, water content, water-to-cement ratio, compressive strength and cement content [Schmitt and Darwin 1999]. Increased slump and water-to-cement ratio have been shown to contribute to increased plastic settlement cracking, which occurs along the rebars. Increasing cement content makes the concrete more

susceptible to restrained shrinkage cracking and results in an increased crack density. There is also a high correlation between the temperature at placement and the crack density. Higher temperatures of concrete at the time of placement have been shown to result in higher incidence of cracking in the deck. In addition, data suggests that cracking highly likely if the concrete deck temperature exceeds the temperature of the girder by 20 deg C [Browning and Darwin 2007].

Recommendations for modifications of materials and construction techniques to reduce the amount of cracking in reinforced concrete decks have recently been developed from the results of a pooled-fund study under the direction of Kansas Department of Transportation (KDOT) in conjunction with 14 other DOTs and the Federal Highway Administration [Browning and Darwin 2007]. It is suggested that shrinkage cracks can be reduced by decreasing the volume of water and cement and maintaining an air content above 6 percent. In addition, for low cracking –high performance concrete, a maximum cement content of 535 lb/ft^3 (317 kg.m^3), a maximum water-to-cement ratio of 0.42, an air content of 8.0+1.0 percent, a slum of 1.5 to 3.0 inches (38 to 75mm) and Type I/II cement, are recommended.

Considerable research has been performed to identify the different mechanisms, namely, volumetric changes associated with thermal and shrinkage strains, which are responsible for tensile stresses in the concrete deck [ACI 209 2005; French et al. 1999, Weiss et al. 1998a, Mohr and Hansen 1997]. Some quantitative information about the magnitude of volumetric change associated with these mechanisms has been obtained under controlled laboratory conditions. However, quantitative information and co-relations between the material composition, the in-situ material properties and cracking in the bridge decks are not available. Very few field studies that carefully identify the causes of tensile stress in the material and the role of the material properties in deck cracking have been undertaken so far.

New York State Department of Transportation (NYSDOT) has adopted a high performance (HP) concrete mix for bridge decks, which was developed with the objective of improving performance and durability of bridge decks. The mixture composition by weight of the component materials has been standardized (Section 500 of Standard Specifications) and the materials used in HP concrete should meet the requirements of Section 700 of NYSDOT Standard Specifications [NYSDOT 2002]. The local materials available for construction, especially the aggregates used in producing the HP concrete, can however vary widely between geographic locations. This could potential have a significant impact on the in-situ properties of concrete. The exact composition of the cementitious materials can also vary between the Regions because only the amounts and types of pozzolanic materials are specified. The variabilities in the chemical compositions of the different types of pozzolanic materials and their reactivities introduce additional variations in the rate of property development of the concrete. Despite these different characteristics it is essential that the HP bridge decks exhibit long service life without excessive deterioration caused by cracking related to material causes.

1.2 Research Need Statement

To insure that premature deterioration does not occur, it is essential that (a) the mechanisms responsible for causing cracking in the concrete are identified; and (b) the influence of the local materials on the performance of concrete is investigated. There is clearly a need for (a) developing an fundamental understanding of the mechanisms that could

potentially lead to tensile stress development and cracking in bridge decks; and (b) assessing the influence of local materials on the performance and cracking potential of HP concrete. Developing an understanding of the cause of cracking should begin with an evaluation of concrete from existing bridges with and without distress. This information combined with measured response from instrumented bridges would help determine the role of the different mechanisms which contribute to stress development in concrete deck. Since the material response of concrete, which has a direct bearing on the tensile stress development, is directly influenced by the local materials used in the HP mix, the role of local materials has to be investigated. Finally, the influence of local materials on the potential for cracking, needs to be evaluated.

The need for additional research identified in the previous paragraph forms the basis for this study. From the findings reported here, guidelines can be developed to improve the material and the construction practices to minimize the potential for premature cracking, thereby providing long-lasting, low-maintenance durable concrete decks.

1.3 Objectives

The specific objectives of this study were:

- To evaluate concrete material properties in existing bridge decks at different locations in Region 7 of NYSDOT.
- To correlate the in-situ material properties in existing decks with the observed cracking.
- To monitor the in-situ movements and strains in HP concrete bridge decks associated with hydration and ambient temperature changes.
- To assess the contributions of temperature and shrinkage to stresses in the concrete deck and steel girders.
- To determine the development of material properties of HP concrete from different Regions of New York State.
- To assess the influence of local materials on the development of material properties and unrestrained free shrinkage of concrete.
- To assess the influence of local materials on the potential for restrained shrinkage cracking of concrete.

1.4 Outline of Research Study

The goal of this study is to investigate causes of cracking in HP concrete decks in New York related to local materials. The work is organized in three phases to address the research needs outlined before. The scope and description of work in each phase is given below.

Phase I: Investigation of Existing Bridge Decks

This phase of the project deals with evaluating the in-situ properties of concrete in existing bridge decks. The work in Phase I involves the following: planning and executing bridge surveys; collating information from the surveys to assess the nature, extent and severity of damage; developing a systematic procedure for obtaining cores from the bridge deck; conducting an experimental program for evaluating the in-place material properties of concrete using cores extracted from bridge decks; evaluating the in-situ concrete properties;

and developing a qualitative assessment of the cracking as it relates to in-situ concrete properties.

Phase II: Investigation of Newly constructed HP Bridge Decks

Phase II deals with monitoring the response of HP concrete in newly constructed bridges. Work in the phase includes developing an instrumentation plan for collecting temperature and strain data from bridges, analyzing the data to evaluate the early movements of the girders and the bridge deck and developing an understanding of the role of the different mechanisms which contribute to stress development in concrete deck.

Phase III: Evaluation of the Influence of Local Materials on Performance of HP Concrete

This phase of the project deals with laboratory evaluation of the HP concrete, using local materials from different regions of NYSDOT. Materials used in newly constructed bridge decks from different regions of New York were sent to the material laboratory of Civil Engineering department at City College of New York. An experimental program was conducted to evaluate the HP concrete mixtures and to determine the role of the local materials on the observed material behavior.

1.5 Outline of Work and Research Methods

Since the three phases deal with disparate aspects of evaluating performance of HP concrete, each Phase of work is describes separately. The research methods used in each phase are outlined and the results of each phase are presented individually in three separate sections. A brief summary of each section is given below.

Phase I – Following bridge surveys, concrete cores were obtained from five bridge decks in Region 7. The in-place material properties of concrete obtained by testing the cores are presented and analyzed. Based on the results of the testing program, observations about the nature of cracking in the bridge decks are presented.

Phase II – Two bridges were selected for instrumentation. Temperature and strain data were collected from thermocouples and vibrating wire strain gages embedded in the concrete deck and from those attached to the girders. Data was collected for a period extending from one day before casting of the slab, through casting, setting and early strength gain of the concrete slab up to 28 days of age. The temperature and strain data collected from the bridge decks are presented in this report. Analyses of temperature and strain measurements are presented.

Phase III – The local materials which were used in three newly constructed bridges located in three different regions in the State of New York were evaluated. The results of the laboratory evaluation of HP concrete are presented. Specifically the following information is reported: (a) the development of the material properties with age especially the tensile strength, the elastic modulus and compressive strength; (b) unrestrained autogenous and drying shrinkage strains with time; and (c) the potential for cracking when the free shrinkage is restrained.

From the results of this investigation, the key findings and recommendations pertaining to minimizing the potential for early age cracking in HP concrete decks are summarized and presented.

Section 2: Phase I Investigation
(Evaluation of HP Concrete in Existing Bridge Decks)

2.1 Introduction

Phase I of the research project involves evaluating the in-place properties of concrete in existing bridge decks. Bridges in Region 7 of NYSDOT were selected for evaluation. The broad objectives of this study were to evaluate the in-situ material properties of concrete and to develop a qualitative understanding of the nature of cracking observed in the bridge decks.

2.2 Objectives

The specific objectives of Phase I research are:
- To evaluate concrete material properties in existing bridge decks at different locations in Region 7 of NYSDOT.
- To relate the in-situ material properties in existing decks with the observed cracking.

2.3 Scope of Work

The work in Phase I involves the following: planning and executing bridge surveys; collating information from the surveys to assess the nature; extent and severity of damage; developing a systematic procedure for obtaining cores from the bridge deck; conducting an experimental program for evaluating the in-place material properties of concrete using cores extracted from bridge decks; evaluating the in-situ concrete properties; and developing qualitative assessment of the cracking as it relates to in-situ concrete properties. Following bridge surveys, concrete cores were obtained from five bridge decks in Region 7. The in-place material properties of concrete obtained by testing the cores are presented and analyzed. From the analysis of data, observations about the nature of cracking in the bridge decks are presented.

2.4 Bridge Selection and Bridge Deck Survey

A review of bridge database from Region 7, available with the New York State Department of Transportation (NYSDOT), was performed. The candidate bridges for evaluating material properties were selected after reviewing the results of bridge deck surveys. Representative bridge decks, both cracked and uncracked, were selected.

2.4.1 Criteria for selecting bridge decks for further evaluation

Criteria for selecting bridge decks included factors which provide for a reasonable comparison of results between the different decks and included the following: number of spans; number and type of girders; the magnitude and frequency of live load; nature and type of supports and bearings; and ambient environmental conditions. Specifically, the following factors were considered:

1. Type of Construction: Single span bridges with concrete deck over steel girders with elastomeric bearing supports were considered. A steel-girder bridge was selected for evaluation because such bridges have been shown to exhibit the greatest extent of

cracking in concrete decks [Darwin et al. 2004]. Concrete deck on steel girders/stringers construction is also the predominant type of construction for highway bridges in New York. In bridges with a single span the structural effects arising from continuity can be eliminated.

2. Concrete mix: Since NYSDOT has adopted high performance (HP) concrete mix for bridge decks, only HP decks were considered for this study.

2.4.2 Selection of Bridges for Evaluation

Initially, from the available database, 19 bridges were selected following the criteria listed above (details of the bridges in Appendix A). Additional criteria listed below were used to arrive at the final list of bridges for further evaluation.

1. Type of Cracking exhibited by the bridge deck: Shrinkage usually results in transverse cracks, which form perpendicular to the length of the bridge deck. Thus it was decided to select bridges which exhibited transverse cracks. In addition, bridge decks which exhibit no or minimal cracking and longitudinal and/or diagonal cracking were also selected for comparison. Care was taken to ensure other criteria such as type of construction and concrete mix were comparable in these bridges. The information about cracking was obtained from the existing bridge deck survey reports.

2. Truck loading: Candidate bridges selected for evaluation should be subjected to comparable loading to eliminate load-induced effects in cracking.

Based on a review of design drawings, evaluation of the condition surveys and the bridge deck inspection (performed by the NYSDOT), the following five bridges in Region 7 were selected for Phase I testing:

1. BIN 1000440-Jefferson County – Rte. 3 over South Sandy Creek
2. BIN 1008840-St. Lawrence County – Rte 11 over West Branch St. Regis
3. BIN 3369170-Lewis County – Vorce Rd. over Deer River
4. BIN 1021350-Franklin County – Rte. 30 over Trout River (Constable)
5. BIN 1023970-Franklin County – Rte. 37 over Salmon River (Fort Covington)

The bridges selected for further evaluation have the following characteristics:

(a) Single span – All the bridges selected are single span bridges. The first two bridges are built with integral abutments, while the last three bridges are simply-supported on elastomeric bearings.

(b) Steel Girder – All the bridges selected have steel girder which support a concrete deck.

(c) High performance concrete (HP) – The bridge decks were made using HP concrete.

(d) Nature of cracking — First three bridges contain longitudinal cracks in their concrete deck, approximate parallel to the traffic. The last two bridges contain transverse cracks, approximate perpendicular to the direction of traffic.

(e) Nature of loading – The bridges selected for evaluation were located on State highways and country roads, which ensured low to moderate truck traffic.

2.5 Bridge Deck Survey and Locations of Cores

The bridge identified for Phase I testing were surveyed on April 22 and 23, 2004. The exact location and length of cracks on the bridge were catalogued and cross-checked with the existing bridge deck surveys available with NYSDOT. Only cracks which were visible to the un-aided eye from a distance of 3 ft from the surface of the concrete were included in the survey report. The approximate locations and patterns of cracks from the bridge deck survey are shown in Figures 1 to 5. It is interesting to note that the bridges with integral abutments exhibited longitudinal cracking over the locations of the girders. These cracks were the widest at the support and typically extended for a short distance in the longitudinal direction. The transverse cracks in BIN 1023970 were located over the mid-span region of the bridge. These cracks were spaced at 2-4 ft intervals.

The exact location and number of cores to obtain from each bridge deck were identified after compiling the information from the existing bridge surveys and the field observations. The following criteria were used while determining the locations of cores:

1. Obtain a minimum of one core through an existing crack – This core would provide information about the depth of the crack.
2. Obtain a minimum of two cores from concrete immediately adjoining the crack – for tensile and compressive strength determination
3. Obtain a minimum of four cores at a healthy area of the deck – for tensile and compressive strength determination

The approximate locations and the number of cores obtained from each bridge deck are shown in Figures 1 through 5. Each circle in the drawing represents one location for obtaining a core. The number inside each circle shows the core number which was used to identify the core. For example;

Indicates – Core Sample Number
4 from a specific location
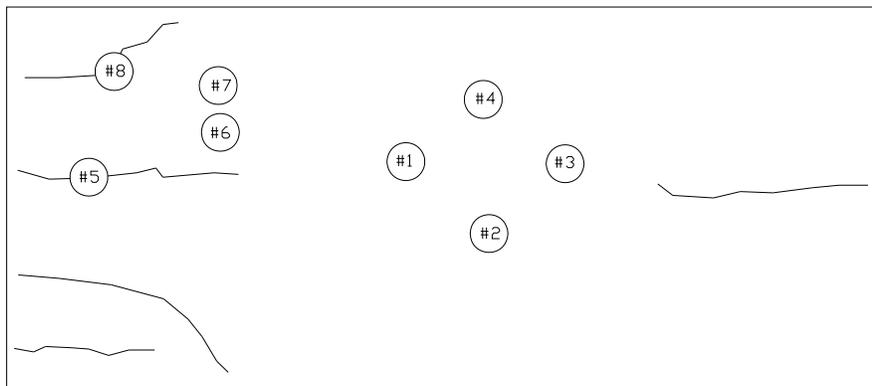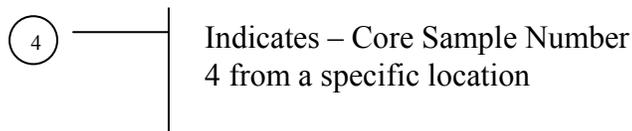
Figure 1: The locations of cores obtained from BIN 1000440-Jefferson County – Rte. 3 over South Sandy Creek
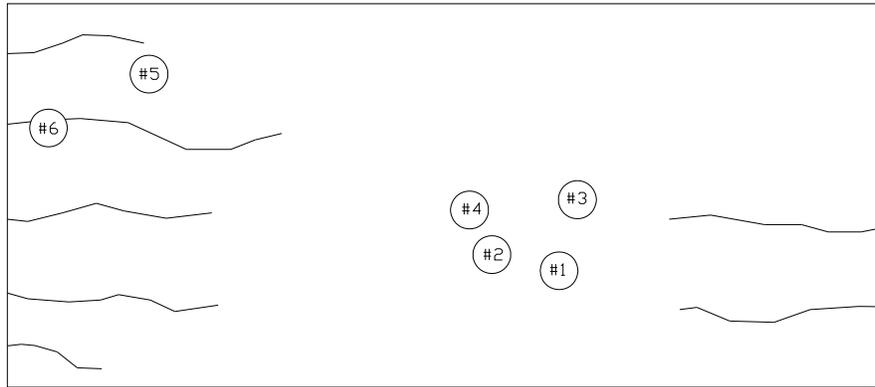
Figure 2: The locations of cores obtained from BIN 1008840-St. Lawrence County – Rte 11 over West Branch St. Regis
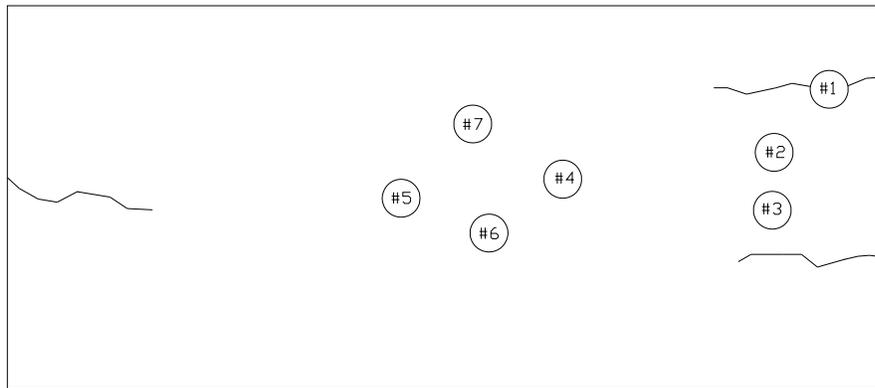
Figure 3: The locations of cores obtained from BIN 3369170-Lewis County – Vorce Rd. over Deer River
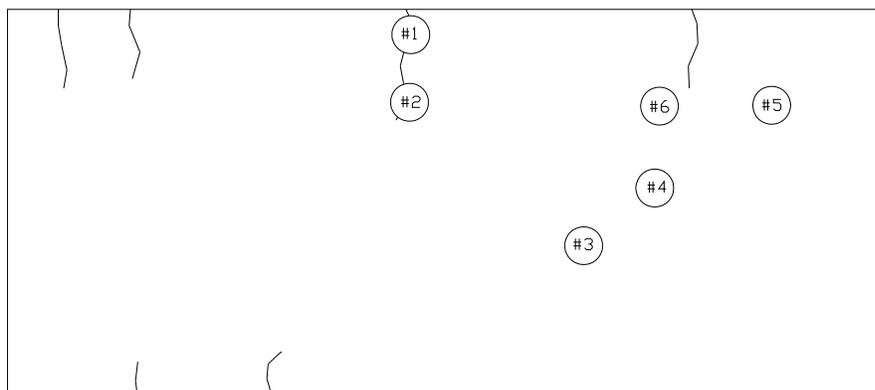
Figure 4: The locations of cores obtained from BIN 1021350-Franklin County – Rte. 30 over Trout River (Constable)
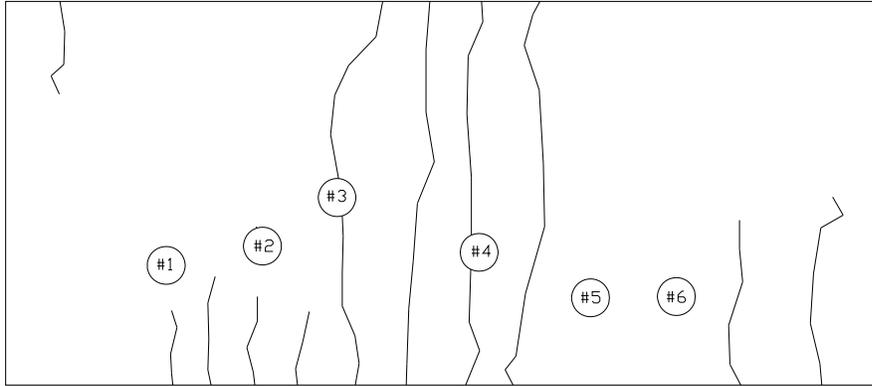
Figure 5: The locations of cores obtained from BIN 1023970-Franklin County – Rte. 37 over Salmon River (Fort Covington)

2.6 Experimental Protocol and Test Procedures

This section lists the different test procedures and the measurements performed on cores obtained from the bridge decks and the information obtained from each measurement. The test program consisted of evaluating cracked deck core specimens using image analysis and obtaining material properties of concrete from the uncracked deck cores. The following tests were performed on the cores obtained from the bridge decks:

(a) *cores from cracked areas*: optical measurements to determine the nature of cracking (through or around the aggregates), the crack width and crack profile along the depth.

(b) *cores obtained from uncracked areas*: (1) Dynamic Elastic Modulus; (2) Elastic modulus and Compressive Strength; and (3) Tensile Strength using split cylinder test.

Image analysis was performed directly on cores obtained from the cracked areas of the bridge deck. Specimens for mechanical testing were obtained after cutting the cores to the desired length. The test procedures used to obtain the different material properties are listed in the following sections.

2.6.1 Image analysis

Image analysis was performed on cracked concrete cores to determine the nature of cracking in bridge decks. Specifically, the parameters obtained from the image analysis were: (a) the type of cracking (through or around the aggregate); (b) crack width; and (c) length of crack with respect to the thickness of deck. Sufficient data was collected to provide for a statistical evaluation of these parameters.

The test setup used for image analysis comprised of a high resolution digital camera (1024x1024 pixels), which was interfaced with a computer using an image acquisition board as shown in Figure 6. For each cracked specimen digital images were captured by placing the camera perpendicular to specimen. Photographs were captured by placing the crack in the center of the image. Two images corresponding to the opposite faces of the cracked specimen were captured. Digital photographs were taken of all cracked specimens with the digital camera and stored in the computer for later analysis.
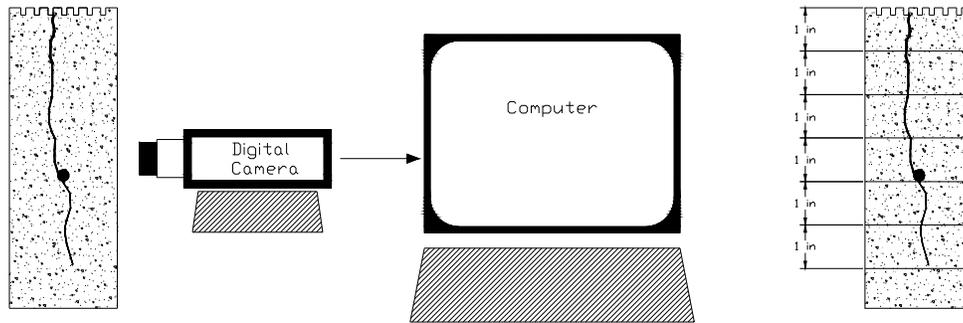
Figure 6: Test setup for Image Analysis of cracked cores

Image analysis for each core specimen consisted of compiling the information about the different parameters as function of depth from the surface. This was accomplished by optically slicing each image into 1 inch thick slices as shown in Figure 6. Within each slice of the specimen, the following parameters were measured: (a) the number of aggregates with cracks through and the number of aggregates with cracks around the interface; and (b) the crack width. The information from all the slices from one specimen were used for: (a) determining the crack profile (the width of the crack as function of depth from the surface); and (b) performing a statistical evaluation of the number of aggregates that the crack passed through and number of aggregates that the crack passed around.

2.6.2 Ultrasonic pulse velocity testing

Specimen preparation for ultrasonic pulse velocity testing comprised of cutting the cores obtained from the uncracked areas of the bridge decks. Inspection of the uncracked cores revealed that both ¾ in epoxy coated rebars and 1/5 in diameter wire mesh reinforcement were present. The criterion followed while cutting the cores to obtain specimens was to maximize the length of concrete after excluding steel rebars with a diameter larger than or equal to ¾ inches. The specimens were ground using a hand-held grinder to make the cut-surfaces parallel to each other and to reduce the discontinuities in the contact surface between pulse meter and concrete.

The length of each specimen was measured using Vernier calipers. The length of the specimen required for calculating the pulse-velocity was obtained as the average of four measurements along the perimeter of the cylinder. The transit time of the ultrasonic pulse through the cylinder was obtained using a commercially available V-meter manufactured by James Instruments. The reading of ultrasonic transit time was obtained by attaching the ultrasonic transducers to the surfaces of circular faces of the concrete specimen using a couplant. The couplant was used to remove any air-gap between the porous surface of concrete and the transducer. The experimental test setup for ultrasonic pulse velocity measurement is shown in Figure 7. All specimens were tested five times and the transit-times in microseconds were recorded for each specimen.

Figure 7: Ultrasonic pulse velocity setup

2.6.3 Split Tension testing

Split-tension tests were performed to determine the tensile strength of concrete specimens obtained from the bridge deck cores. Split tension tests were performed on specimens obtained after excluding steel rebars larger than ¾ in in diameter. Prior to each test the length and the diameter of each specimen were recorded as the average of four independent measurements. All specimens were tested as per the requirements of ASTM C496 – 96. The specimen loading rate was applied in the range of 100 to 200 psi/min up to failure. The maximum applied load was recorded for each test. The experiment setup for the split cylinder test is shown in Figure 8.

Figure 8: Split tension test setup (ASTM C496 – 96)

2.6.4 Compression testing

Compression testing was performed to obtain the Young's modulus and the compressive strength of concrete. Core from the uncracked areas of the bridge deck were used to prepare specimens. Specimen preparation for compressive testing consisted of cutting the cores to the desired length and capping the specimens. The specimens were capped as per the specifications given in ASTM C 617 – 98. Two types of specimens were used for compression testing. The first set of specimens was obtained after cutting cores to exclude rebar larger than ¾ in. The length and the diameter of each specimen were determined as the average of four independent measurements, before capping. These specimens were tested as per the provisions of ASTM C-39 to obtain the compressive strength. The specimens were loaded at a rate equal to 22.60 kips/min up to failure. The maximum load at failure was recorded. The second set of specimens, which were primarily used for determining the Young's modulus, included the steel rebars. These specimens were cut at the ends to provide a flat surface and capped before testing. The length and the diameter of each specimen were determined as the average of four independent measurements, before capping. The applied load was cycled between 5 and 40% of the compressive strength. Four load cycles were applied at a loading rate equal to 22.60 kips/min. During each load cycle, the deformation of the concrete was measured using an LVDT that was attached over a gage length equal to 2 inches. The load and the deformation of the specimen were recorded at one second time interval during each load cycle. Following the load cycles, the specimens were loaded up to failure and the maximum load was recorded. The experiment setup used for determining the elastic modulus and the compressive strength are shown in Figures 9(a) and (b), respectively.
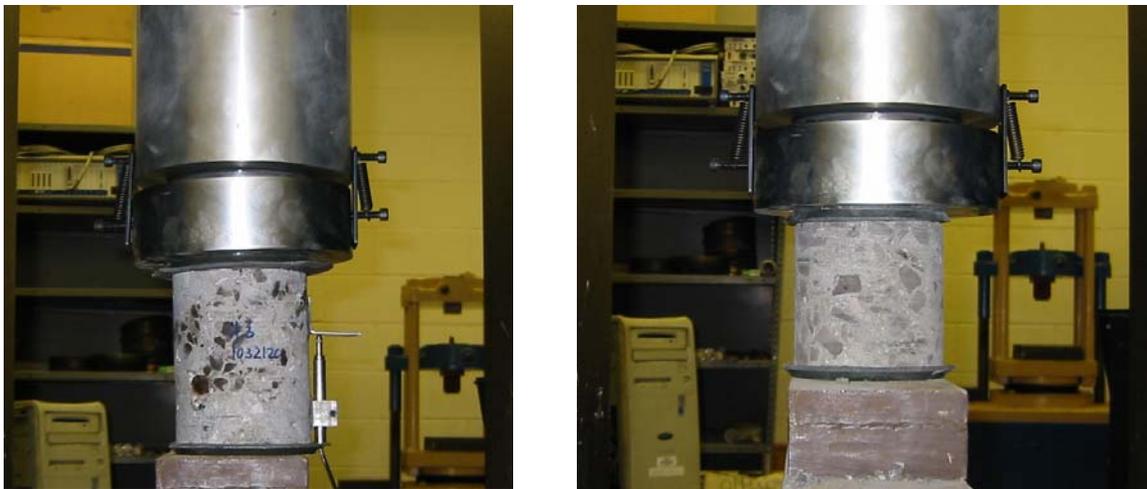
Figure 9: (a) Concrete elasticity modulus set up; (b) ASTM C39/C 39M set up

2.7 Test Results

The results of the Phase I experimental test program using the cracked and the uncracked cores are tabulated in Appendices B and C, respectively. The test results from the image analysis, the ultrasonic velocity measurements and the mechanical tests are summarized in the next few sections.

2.7.1 Image analysis

The results of the image analysis showing the width of the crack, the number of fractured and the number of un-fractured aggregates (ie. where the crack passed through the aggregate vs. where the crack passed around the aggregate) at different locations along the height of the core, obtained from the 1 in optical slices, are tabulated in Appendix B. The data from the different slices in the image analysis allows for a statistical evaluation of the relative percentages of cracked and uncracked aggregates at the location of a crack. The crack widths measured in each slice were used to generate the crack profile in the specimen. The compiled results for each bridge are presented next.

BIN 1000440-Jefferson County – Rte. 3 over South Sandy Creek

Results of the image analysis of the two cracked cores, core number 5 and 8 are presented in Table 1 and Figure 10. Core 5 did not retain integrity and therefore could not be used to calculate the average crack width. The compiled results indicate that the crack in the cores primarily passed around the aggregate.

Table 1: Compilation of data from cracked cores for BIN 1000440

Core #	% of crack around aggregate
8	94.7%

Core #	% of crack length w/respect core length
5	47.0%
8	50.0%
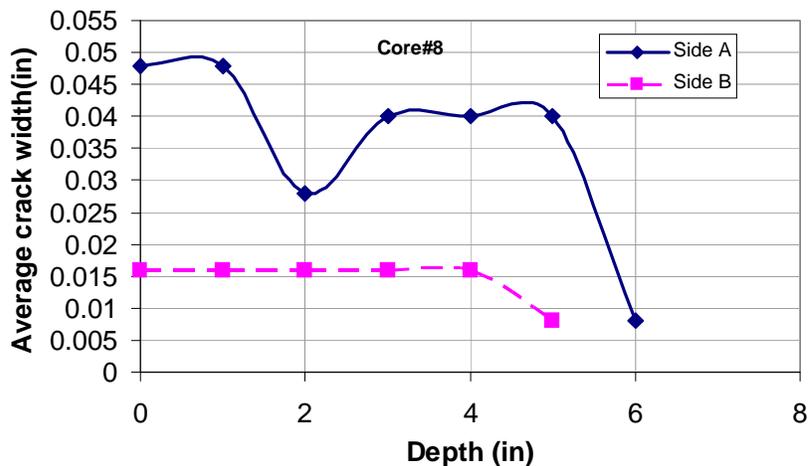
Figure 10: Crack profiles as a function of depth for BIN 1000440

BIN 1008840-St. Lawrence County – Rte 11 over West Branch St. Regis

Results of the image analysis performed on two cracked cores, cores number 5 and 6 are summarized below in Table 2 and Figure 11. The cracks were all formed around the aggregates in both cores. The crack profile from core 5 indicates that while the crack width on the surface is large, it decreases very rapidly with depth. The crack in core 6 was very fine and was confined to a small region close to the surface.

15

Table 2: Compilation of data from cracked cores for BIN 1008840

Core #	% of crack around aggregate
5	100.0%
6	100.0%
Core #	% of crack length w/respect core length
5	89.2%
6	44.0%
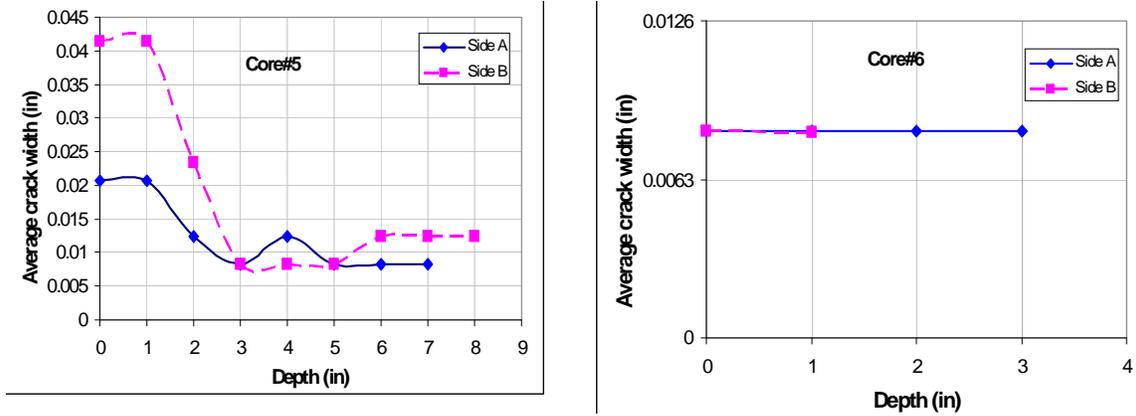
Figure 11: Crack profiles as a function of depth for BIN 1008840

BIN 3369170-Lewis County – Vorce Rd. over Deer River

Results of the image analysis on the single cracked core provided, core number 1, are presented below in Table 3 and Figure 12. The crack in this core appears to be confined to a small depth close to the surface of the bridge deck and formed around the aggregates. The crack widths were very small and hard to measure accurately.

Table 3: Compilation of data from cracked cores for BIN 3369170

Core #	% of crack around aggregate
1	100.0%
Core #	% of crack length w/respect core length
1	13.3%
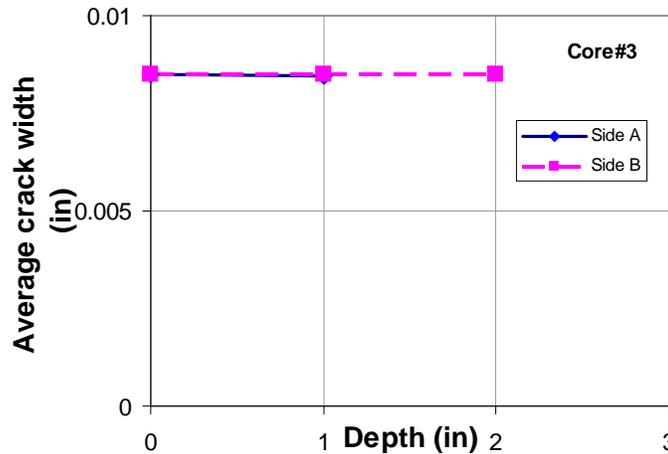
Figure 12: Crack profiles as a function of depth for BIN 3369170

BIN 1021350-Franklin County – Rte. 30 over Trout River (Constable)

The results of the image analysis performed on two cracked cores provided, cores number 1 and 2, are summarized below in Table 4 and Figure 13. The cracks appear to be predominantly around the aggregates. Careful inspection of the specimen revealed that the cracks passed around most of the aggregate. The aggregate which were found to be fractured (instance when the crack passed through the aggregates) appeared different than the surrounding aggregate. These aggregates had a different color and aspect ratio when compared with the other aggregates in the bulk of the sample. If these aggregate are excluded from the analysis, all the cracks were found to pass around the aggregates.

Table 4: Compilation of data from cracked cores for BIN 1021350

Core #	% of crack around aggregate
1	57.6%
2	65.6%
Core #	% of crack length w/respect core length
1	67.9%
2	77.6%
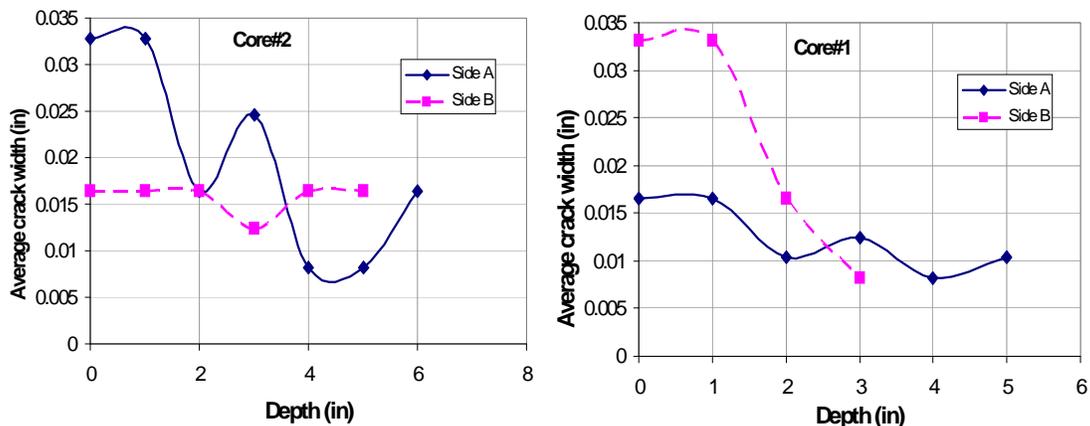
Figure 13: Crack profiles as a function of depth for BIN 1021350

17

BIN 1023970-Franklin County – Rte. 37 over Salmon River (Fort Covington)

The results of the image analysis performed on two cracked cores provided, cores number 1 and 2 are summarized below in Table 5 and Figure 14. The cracks in the cores were primarily formed around the aggregates. Some aggregates were found to be split by the cracks. However, these aggregates had a different aspect ratio when compared with the other aggregate found in the bulk of the sample. The crack profile from cores 1 and 2 indicate that while the crack width on the surface is large, it decreases very rapidly with depth.

Table 5: Compilation of data from cracked cores for BIN 1023970

Core #	% of crack around aggregate
1	85.2%
2	62.4%
Core #	% of crack length w/respect core length
1	92.2%
2	95.2%
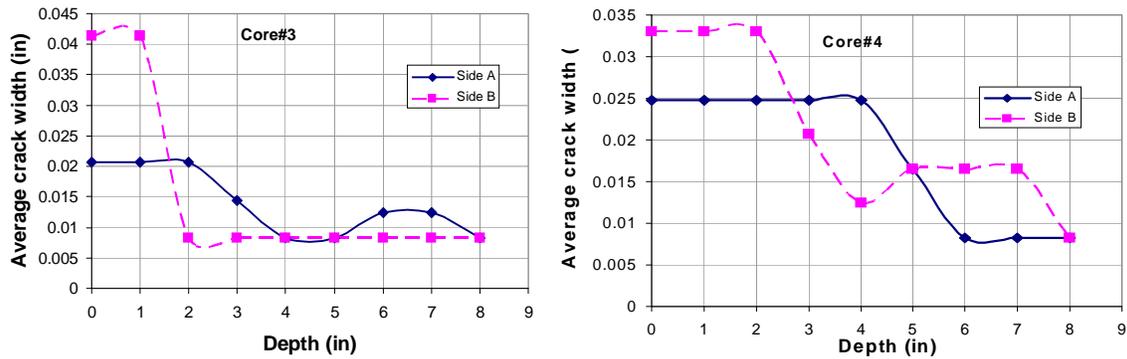
Figure 14: Crack profiles as a function of depth for BIN 1023970

2.7.2 Ultrasonic pulse velocity testing

The ultrasonic pulse velocity was determined by dividing the length of each specimen with the transit time for the pulse recorded using the V-meter. Ultrasonic pulse velocity provides an indication of the uniformity and the quality of concrete. High pulse velocity readings are generally indicative of good quality concrete. A general relation between concrete quality and pulse velocity from Leslie and Cheeseman (1949) is given in Table 6. The values of the ultrasonic pulse velocity for all the samples tested are tabulated in Appendix C. The pulse velocity from all the samples from a given bridge deck were found to be relatively high and in close agreement with each other. The average value of the ultrasonic pulse velocity for each of the bridge decks are shown in Table 7. It can be observed that the pulse velocity from all the bridges is consistently higher than 12000 m/s. This implies the quality of concrete is relatively "Good" as per Table 6.

Table 6. Quality of Concrete and Pulse Velocity

General Conditions	Pulse Velocity ft/sec
Excellent	Above 15,000
Good	12,000-15,000
Questionable	10,000-12,000
Poor	7,000-10,000
Very Poor	below 7,000

The dynamic elastic Young's modulus was estimated for the concrete using the empirical equation provided by the vendor of the V-meter (Equation 1). In this equation, the pulse velocity, V, is in ft/s and the dynamic elasticity modulus, E_c, is obtained in psi. The values of dynamic elastic modulus obtained from the average value of pulse velocity for each bridge deck are shown in Table 7. The relatively high values of the dynamic modulus, values higher than $3x10^6$ psi, further suggest that the concrete in the bridge decks was of relatively good quality.

$$Ec=-3.137E-15*V^6+2.564E-10*V^5-8.706E-6*V^4+1.572E-1*V^3-1.593E3*V^2+$$
$$+8.587E6*V-1.923E10 \hspace{3cm} (1)$$

Table 7: The ultrasonic pulse velocity and the dynamic modulus for all the bridges tested

BIN	Ultrasonic pulse velocity (ft/s)	Elastic Modulus (psi)
1000440	13542.16	2.966E+06
1008840	15544.33	5.816E+06
3369170	15808.28	6.379E+06
1021350	14081.69	3.504E+06
1023970	14448.64	3.946E+06

2.7.3 Compression testing

Compression testing was performed on specimen prepared from cores obtained from the uncracked areas of the bridge to determine the Young's modulus (E_c) and compressive strength ($f_c^{/}$). Testing for determining the elastic modulus were performed using specimens which included the ¾ in rebars. Compressive strength tests were performed on both specimens, which contained ¾ in rebars and those without the ¾ in rebar. Since the length/diameter (L/D) ratio of the specimens tested was less than two, a correction factor given in ASTM C39/C 39M was applied in order to obtain the compressive strength, $f_c^{/}$, from the maximum load recorded in a compression test. The correction factor was only applied to specimen with L/D in the range, $1.75 \leq L/D \leq 1$. To determine the correction factor, a polynomial equation shown below was developed using the values given in ASTM C39/C 39M (Equation 2). The value of compressive strength, $f_c^{/}$, was obtained by multiplying the peak stress with the correction factor. For specimens with L/D less than 1.0, no correction value was applied to the compressive stress at failure, f_c, which was obtained by dividing the maximum load by the cross-sectional area of the specimen. The values of E_c, $f_c^{/}$ and f_c obtained from cores from all the bridge decks are shown in Appendix C. The average values of $f_c^{/}$, E_c and fc for each bridge deck are tabulated in Table 8. It can be seen that the values of $f_c^{/}$ obtained from specimens with and without the rebars are comparable. The value of f_c

obtained from specimen with L/D <1, however, is significantly higher than the $f_c^{/}$ values. There appears to be no consistent correlation between the values of f_c and $f_c^{/}$. In specimens with L/D<1.0, the end friction at the platens plays a significant role in determining the load response of the specimen. Small changes in the length of the specimen could potentially result in significant changes in the maximum load.

$$Correction\ Factor = (0.213 * (\frac{L}{D})^3) - (1.04 * (\frac{L}{D})^2) + (1.767 * (\frac{L}{D})) - 0.07 \qquad (2)$$

Table 8: The compressive strength and the elastic modulus for all the bridges tested

BIN	specimens w/o rebars		specimens with rebars	
	fc'$_{average}$ L/D>1 (psi)	fc$_{average}$ L/D<1 (psi)	fc'$_{average}$ L/D>1 (psi)	Ec (psi)
1000440	5749	6821	5518	4596000
1008840	-	6856	7201	-
3369170	6046	9249	5405	3410000
1021350	5910	9017	6251	3582000
1023970	-	7959	6375	3315000

The values of compressive strengths for bridges with BIN numbers 1000440, 1008840, 3369170, 1021350 and 1023970, available in the NYSDOT survey reports are, 6525, 6980, 6010, 6860 and 7295 psi, respectively. A correlation between the $f_c^{/}$ values obtained with specimens containing the rebars and those provided by NYSDOT is shown in Figure 15. The diagonal line on the graph represents a one-to-one correspondence between the two values and hence the condition of perfect correlation. It can be seen that the values of compressive strengths from the two sources do exhibit a high degree of correlation. It can also be observed that the values of $f_c^{/}$ obtained in the lab testing are smaller than the values provided by NYSDOT. Nevertheless, the compressive tests indicate that the concrete in the bridge decks had adequate compressive strength (higher than 5500 psi).
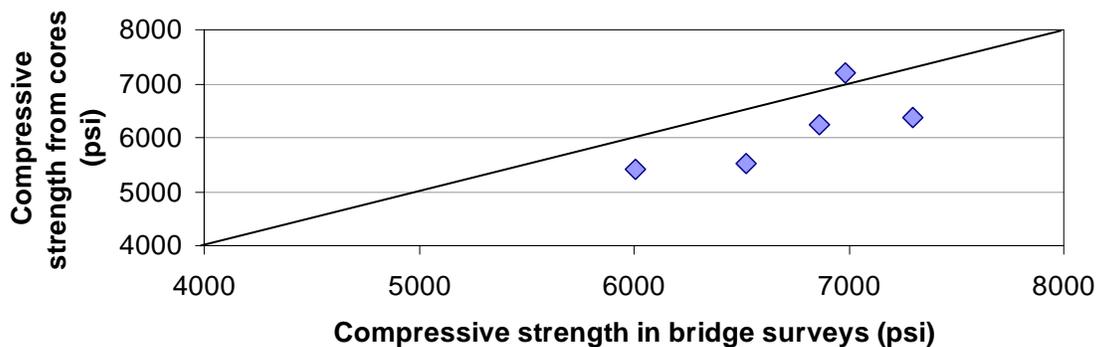
Figure 15: A comparison of the values of compressive strength obtained in the lab testing with those provided by NYSDOT.

The information from the pulse velocity and the compressive strength suggests that the concrete in the bridge decks was of uniform quality and had sufficiently high compressive strength.

2.7.4 Tension testing

The maximum load recorded in a split tension test was used to determine the tensile strength of concrete as shown in Figure 16. The failure in split tension tests is produced by splitting of the cylinder along the diameter of the specimen, joining the points of load application. All specimens were visually inspected after failure. Failure cracks in all the specimens tested (all specimens from all bridges) were found to pass through the aggregate. The failure surfaces of few typical samples are shown in Figure 17. This is an indication that load-induced cracks in mature concrete will primarily pass through the aggregate. This distinguishing characteristic helps identify load-induced cracks in mature concrete.

Split tension Strength

$$f'_t = \frac{2P}{\pi L d}$$
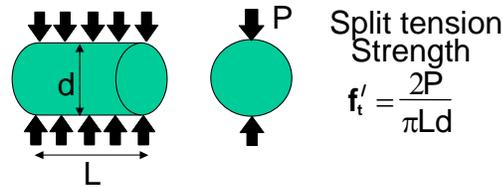
Figure 16: Split tension test

Figure 17: Specimens after performing split-cylinder testing as per ASTM C496 – 96

The results of the tensile strength obtained using the specimens prepared from the cores are shown in Appendix C and are summarized in Table 9. The values of tensile strength from the five bridge decks compare favorably with each other. The magnitude of the tensile strength appears to be of relatively high, which suggests a high resistance to cracking.

Table 9: Split cylinder tensile strength for all bridges

BIN	ft'$_{average}$ (psi)
1000440	663
1008840	715
3369170	717
1021350	730
1023970	678

The results of mechanical tests performed on cores obtained from the healthy (uncracked) areas of the bridge deck suggest the following:
- *The concrete in the bridge decks had adequate compressive strength. The compressive strength from lab tests compare favorably with those available with NYSOT. The lab tests provide compressive strengths which are higher than 5000psi.*
- *The concrete in all the bridge decks has a relatively high tensile strength. The tensile strength of concrete in all the bridge decks tested was higher than 660psi.*
- *The concrete appears to be of good quality and relatively uniform across the bridge deck*

2.8 Analysis of Test Results

An analysis of results is provided in this section. The in-place material properties obtained by testing the cores are correlated with the observed cracking in the bridge decks. The results from the experimental program are reconciled with other information such as the type of concrete used, the location of cracks in the bridge deck, the type of embankment and support, the number of traffic lanes and average length of the crack on the surface of the bridge deck etc., to analyze the nature of cracking in each of the bridges selected in Phase I.

BIN1000440-Jefferson County – Rte. 3 over South Sandy Creek

The characteristic features of this bridge are:
1. This is a single span bridge with one traffic lane in each direction
2. The bridge is built with integral abutments.
3. The bridge deck exhibits longitudinal cracking close to the abutments at locations approximately over the steel girders. These cracks are found only close to the abutments. On the surface of the deck, the cracks are the widest close to the abutment.

A quick summary of the test results from cores obtained from the bridge deck is as follows:
1. Image analysis of the cores obtained from the cracked areas revealed that the cracks were formed around the aggregates. Statistically 94.7% of the total crack length is around aggregates.
2. The split tension tests (ASTM C 496-96) on specimen from uncracked areas suggest the following for mature concrete in the bridge deck: (a) a relatively high value of tensile strength (average split tensile strength is equal to 633 psi) is obtained; and (b) load induced cracks in specimens at failure pass through aggregates.

The observed cracking, where the crack primarily passes around the aggregate, when compared with the fact that load-induced cracking in mature concrete passes through the

aggregate <u>suggests that the cracks in the bridge deck were formed at an early age</u> (when the concrete has not attained full design strength). Also the high tensile indicates high resistance to cracking at a later age.

Concrete cracks orientation on this bridge are longitudinal, approximately parallel to the direction of the traffic. The cracks appear to be widest at the abutment and the width decreases away from the abutment. The location and the nature of the cracks and the type of abutment used suggest a restraint of the concrete slab from the abutment, which results in the development of high early age tensile stresses in concrete. However, there is insufficient information from the present test series to conclude about the cause of cracking; it is uncertain if the cracks in the bridge deck were load-induced or were produced due restrained shrinkage/thermal effects.

BIN1008840-St. Lawrence County – Rte 11 over West Branch St. Regis

The characteristic features of this bridge are:
1. This is a single span bridge with one traffic lane in each direction
2. The bridge is built with integral abutments.
3. The bridge deck exhibits longitudinal cracking close to the abutments at locations approximately over the steel girders. These cracks are found only close to the abutments.

A quick summary of the test results from cores obtained from the bridge deck is as follows:
1. Image analysis of cores obtained from the cracked areas revealed that the cracks were formed around the aggregates. Statistically, 100% of the total crack length is around aggregates.
2. Split cylinder tests on mature concrete from uncracked areas indicates a high tensile strength of concrete and that in all specimens tested the load-induced cracks at failure pass through aggregates.
3. The values of the tensile strength and the ultrasonic pulse velocity determined from the different cores obtained from different location on the bridge deck indicates that the concrete is relatively homogeneous and of uniform quality across the bridge deck.

Following the same approach used in the previous case, it can be inferred that the <u>cracks in the bridge deck were formed at an early age</u> since these cracks were found to pass around aggregates. Also, the high tensile strength of mature concrete (average value for the tensile strength is equal to 715 psi) suggests a high probability that the cracks in the concrete bridge deck were formed at an early age.

The cracks in the bridge deck are longitudinal, oriented approximate parallel to the direction of the traffic. Location of the cracks is approximated over the steel girders that support the deck. The location and the nature of the cracks and the type of abutment used may suggest a restraint of the concrete slab from the abutment, which results in the development of high early age tensile stresses in concrete. However, there is insufficient information from the present test series to conclude about the cause of cracking; it is uncertain if the cracks in the bridge deck were load-induced or were produced due restrained shrinkage/thermal effects.

After reviewing the information from the previous bridges there appears to be evidence, which suggests that the longitudinal cracking is influenced by the restraint provided by the integral abutment. This needs further investigation to establish whether these cracks are produced by the action of loads or if they are a result of restrained shrinkage/thermal effects.

BIN3369170-Lewis County – Vorce Rd. over Deer River

The characteristic features of this bridge are:
1. This is a single span bridge with one traffic lane in each direction
2. The bridge is supported on elastomeric bearings at the piers
3. The bridge exhibits curvature in its elevation view
4. There are longitudinal cracks in bridge deck and in the approach slabs. The orientation of the cracks is approximately parallel to the direction of traffic.

Tests on cores from cracked areas reveal that the cracks were observed to pass around aggregates. Statistically, 100% of the total crack length is around aggregates. Based on laboratory results on mature concrete, ASTM C 496-96, it was observed that in all specimens tested failure cracks pass through aggregates. Following the same approach outlined before, we can conclude that cracks in the bridge deck were formed at an early age. Also the tensile strength of the mature concrete, (average tensile strength is 717 psi) suggests a high resistance to cracking at a later age.

In this case, unlike the previous bridges, the restraint from the abutment is not an issue. The bridge girders are supported on elastomeric bearings. The longitudinal cracks were also observed in the approach slabs. During the field survey conducted by the PI, it was noted that the cracks had very small widths on the surface of the decks and extended for distance of few feet from the support. Further, the bridge has a significant curvature in the elevation view. The exact cause of these longitudinal cracks in this bridge deck requires a more detailed analysis which includes consideration of the geometry of the bridge.

BIN1021350-Franklin County – Rte. 30 over Trout River (Constable)

The characteristic features of this bridge are:
1. This is a single span bridge with one traffic lane in each direction
2. The bridge is supported on elastomeric bearings at the piers
3. The bridge deck exhibits transverse cracking, approximately perpendicular to the direction of traffic.

Test on cores from the cracked areas reveal that cracks predominantly pass around the aggregate. Statistically an average of 61.55% of the total crack length is around aggregates. Based in laboratory results on mature concrete, it was observed that in all specimens tested, the load-induced cracks in the failed specimens were observed to pass through aggregates. Further a relatively high value of tensile strength was obtained from the split cylinder tests (the average tensile strength is equal to 730 psi). Therefore, the experimental evidence suggests that the cracks in the concrete were formed at an early age.

The orientation of the cracks on this bridge deck is in the transverse direction, approximately perpendicular to the direction of the traffic. The cracks are located in the mid-span region of the bridge. Considering the following:

(a) Location of the cracks over areas of high compression stress produced by the action of loads

(b) The bridge is supported on elastomeric bearings, which do not provide restraint to horizontal movement of the bridge

suggests a high probability of restrained shrinkage/thermal strains to be the cause of cracking in this bridge deck. However, during the field survey conducted by the PI, it was noted that the cracks had very small widths on the surface of the decks and do not extend across the entire width of the deck. The cracks extended for distance of few feet from the free edge of the slab.

BIN1023970-Franklin County – Rte. 37 over Salmon River (Fort Covington)

The characteristic features of this bridge are:

1. This is a single span bridge with one traffic lane in each direction
2. The bridge is supported on elastomeric bearings at the piers
3. The bridge deck exhibits <u>extensive</u> transverse cracking, approximately perpendicular to the direction of traffic. The cracks are uniformly spaced, approximately 4 - 5 feet apart.

Test on cores from cracked areas reveal that cracks are predominantly observed to pass around aggregates. Statistically, an average of 73.95% of the total crack length is around aggregates. Laboratory tests on mature concrete indicate a high tensile strength (average tensile strength is equal to 678 psi) and that the load-induced cracks at failure pass through the aggregates. Following the same approach outline previously it can be inferred that the cracks in the bridge-deck were formed at an early age.

The cracks are oriented in the transverse direction, approximate perpendicular to the direction of the traffic. Location of the cracks is approximately over areas of high compression stress, close to the middle span of this single span bridge. In addition cracks are equally spaced over this area; spacing between cracks is relatively uniform at 1.5 m. – 2 m. The girders are supported on elastomeric bearings. The location of the cracks, the crack spacing and the type of support used suggests a high-probability of restrained shrinkage and/or temperature strains being the cause of cracking in this bridge deck.

The analysis of results in the previous paragraphs provides an insight into the age of cracking in the five bridges selected for analysis. However, determination of the cause of cracking requires a careful analysis several factors, which are:

1. Loading on the bridges
2. Use of shear studs to provide composite action between the girder and the slab
3. The span of the bridge
4. Ambient temperature and humidity during casting and in the early-age of the concrete

Some of these factors are summarized in the Table 10 below for the five bridges.

Table 10: Compiled data for the bridges in Phase I

BIN	Span (ft)	Girder Spacing (ft)	Stud Shear	Date of Pour	Weather during Pour	Temperature	ConcTemp	Clouds	EvaporationRate
1000440	130	10.8		11/8/2000	overcast, drizzle	46	64	cloudy	0.25
1008840	141	9.02	yes	10/12/1999	40-55 deg overcast; Approaches - 10/14/99 45-55 deg overcast	40		Cloudy	
3369170	150	6.23		9/17/1997	50-65 degp.cloudy; slabs 9/17/97 55-68 deg cloudy	65		Cloudy	
1021350	108	9.51	yes	9/4/1997	42-62 deg clear	42		Clear	
1023970	143	8.63		7/2/1998	42-33 deg cloudy	70	70	Cloudy	

No discernable trends between factors such as the span length, girder spacing, the presence of shear keys etc. and the type of cracking observed on the bridge decks can be inferred. The high temperature at the time of casting in the bridge which exhibits extensive transverse cracking (BIN 1023970), however, supports the argument that restrained shrinkage and/or temperature strains are the probable cause of the observed cracking.

Section 3: Phase II Investigation
(Monitoring the Response of HP Concrete Decks after Construction)

3.1 Introduction

The primary focus of Phase II testing is to evaluate development of early-age tensile stress in the concrete deck slab of the steel-girder bridges. Candidate bridges for Phase II testing were identified after reviewing the statewide Capital Program. This task was performed after meeting with the NYSDOT Bridge Deck Task Force. Criteria used to select candidate bridges for instrumentation were similar to those adopted for selecting bridge decks for Phase I testing. The following factors were considered: the number of spans; number and type of girders; the magnitude and frequency of live load; and ambient environmental conditions. Single span, steel girder bridges with HP deck supported on elastomeric bearings were selected.

Five bridges were selected for Phase III testing and two of these bridges were used for Phase II testing. In Phase III of testing, material samples were collected from the bridge deck sites and sent to the Materials laboratory in the Civil Engineering Department of the City College of New York for material tests. In addition to collecting samples for laboratory testing, the bridges selected for Phase II testing were instrumented using strain-gages and thermocouples prior to casting the deck.

One bridge each in Regions 1 and 3, were selected for instrumentation. Temperature and strain data were collected from thermocouples and vibrating wire strain gages embedded in the concrete deck and from those attached to the girders. Data was collected for a period extending from one day before casting of the slab, through casting, setting and early strength gain of the concrete slab up to 28 days of age. The data was analyzed to evaluate the early movements of the girders and the bridge deck. The temperature and strain data collected from the bridge decks are presented in this report. An analysis of the data combining the strain and temperature information to assess the movement of the bridge deck and the girder and the level of stress in the concrete is presented. Finally, the implications of these findings in the identifying potential for cracking due to restrained thermal and shrinkage cracking in bridges are discussed.

3.2 Objectives

The specific objectives of Phase II evaluation were:

- To monitor the in-situ movements and strains in HP concrete bridge decks associated with hydration and ambient temperature changes.
- To assess the contributions of temperature and shrinkage to stresses in the concrete deck and steel girders.

3.3 Scope of Work

The work presented here comprises of Phase II testing, which deals with evaluating newly constructed bridges. Two bridges were selected for instrumentation. Temperature and

strain data were collected from thermocouples and vibrating wire strain gages embedded in the concrete deck and from those attached to the girders. Data was collected for a period extending from one day before casting of the slab, through casting, setting and early strength gain of the concrete slab up to 28 days of age. The data was analyzed to evaluate the early movements of the girders and the bridge deck. The temperature and strain data collected from the bridge decks are presented. Results from analysis of temperature and strain measurements obtained from newly constructed bridges are presented.

3.4 Criteria for selecting bridge decks for further evaluation

After consulting with the technical working group, it was decided to select bridges for further evaluation based on the following criteria:

1. <u>Type of Construction</u>: It was agreed that the bridges selected for study should comprise of concrete deck on steel girders. It was decided to evaluate bridges with single spans. In bridges with a single span the structural effects arising from continuity can be eliminated.
2. <u>Concrete mix</u>: Since NYSDOT has adopted high performance concrete (HP), it was agreed to study bridges which have HP decks.

3.4.1 Selection of Bridges for Evaluation

From the available database, 5 single span, simply supported bridges were initially selected for further evaluation. After reviewing the drawings and talking with the Engineers-in-Charge of the bridges, it was decided to instrument two bridges, one each in Regions 3 and 1. The selection of two bridges was limited by the availability of two data loggers for use with strain gages. The bridges were selected for strain gages installation based on the ease of access to the steel girders and low skew angle. The bridge in Region 3 (over Seneca river) was determined to be suitable for installing strain gages since the bridge has negligible skew and provided easy (relatively) access to the steel girders. The decision to instrument the bridge in Region 1 was based on proximity to Albany, which allowed for shorter commute to the site. A description of the two instrumented bridges is given below.

Region 1 – Rte. 385 over Murderskill (BIN 1047370)

<u>Description</u>: The bridge is located over a shallow creek. It is a simply-supported, single-span bridge with a skew equal to 32 degrees. The width and span of the bridge are 11.8 m and 41.5 m, respectively. The concrete deck slab is 240 mm in thickness and is supported over five steel girders spaced at 2.50 m across the width. Two rows of shear stud connectors spaced at 300 mm are provided on each steel girder. The steel girders have a varying cross-section along the span and are supported over elastomeric bearings at both abutments. The placement of the rebars was completed on August 3, 2005 and the concrete deck slab was cast on the next day. Figure 18 gives the details about the dimensions of the concrete slab, the cross-section of the steel girder along the span and the cross-section of the composite bridge section.
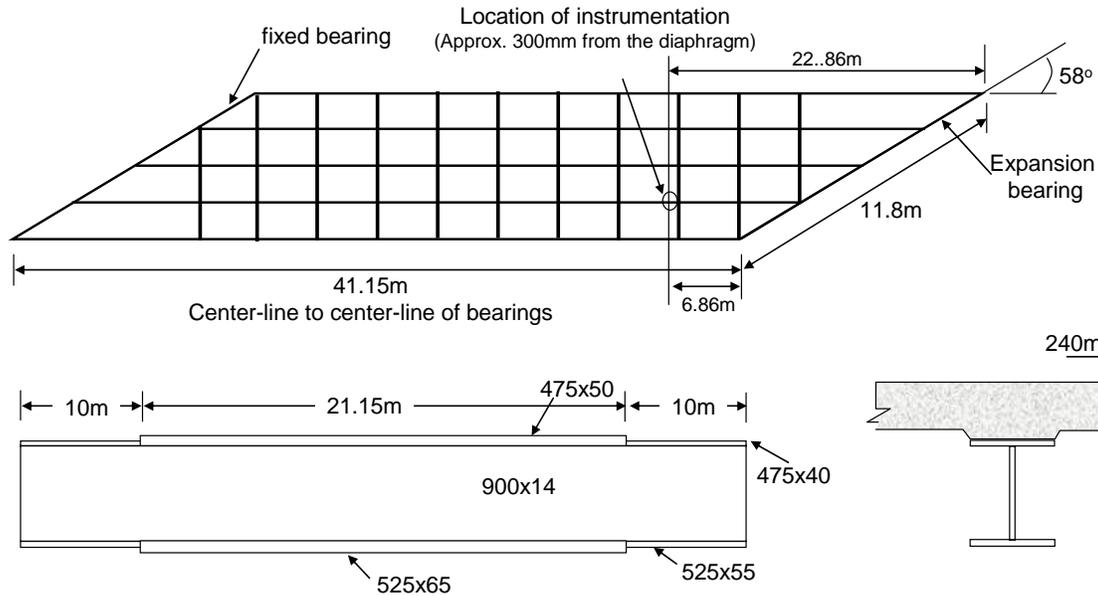
Figure 18: Plan view of the bridge deck slab, elevation of the steel girder and the cross-section of the composite bridge section.

Region 3 – Bridge on Rte. 96 over Seneca River (BIN 1035080)

<u>Description:</u> The bridge is located over a shallow river and was constructed in three stages. Stages I and II were of equal width equal to 7.53 m and comprised of a 240 mm concrete deck supported over three steel girders. The girders are spaced 2.92 m apart. Three rows of stud shear connectors are provided along the span at 175 mm spacing. The steel girders are supported over fixed bearings at one abutment and expansion bearings at the other abutment. The third stage of construction was the closure pour of width equal to 1.04 m, which is symmetric about the center line of the bridge. Stage I of the construction was instrumented. The placement of the rebars was completed on June 19, 2005 and concrete deck was cast on the next day. Details about the dimensions of the concrete slab, the cross-section of the steel girder along the span and the cross-section of the composite bridge section are shown in Figure 19. Photograph of the bridge deck site after the rebars were in place is shown in Figure 20. The orange bucket seen in the photograph corresponds with the location of the sensors in the bridge.
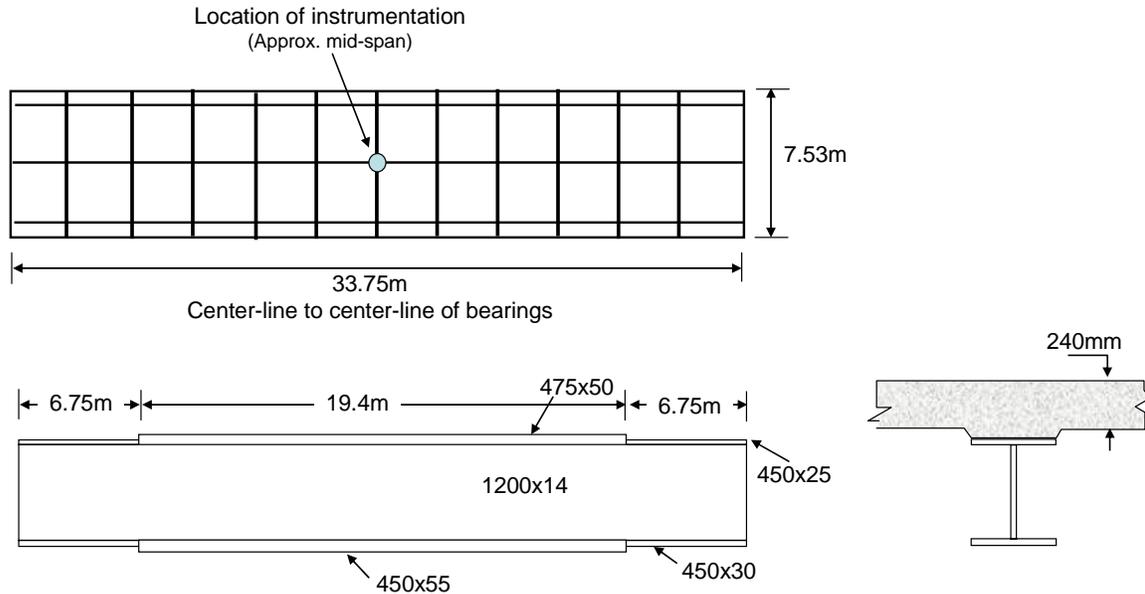
Figure 19: Plan view of the bridge deck slab, elevation of the steel girder and the cross-section of the composite bridge section.

Figure 20: Photograph of the formwork and rebars, prior to casting concrete for the bridge deck in Region 3 (Courtesy Jonathan Kunin, NYSDOT).

3.5 Bridge Instrumentation

This section provides details about the instrumentation, installation and layout of sensor and the data collection procedures. The instrumentation for each bridge comprised of the following:

(a) Three embedded vibrating wire strain gages placed in the bridge deck;

(b) Two embedded thermocouples placed in the concrete deck;

(c) Two surface-mounted vibrating wire gages attached to the flanges of the steel girders; and

(d) Two surface mounted thermocouples, which were attached to the steel girder

The specifications for installing the sensors, the location of the sensors and the data collection procedures are given in Appendix D. The strain gages and the thermocouples in both bridges were placed in the same vertical plane as shown in Figure 21. The approximate locations of the sensors in both bridges are shown in Figures 18 and 19. In Region 3, the sensors were placed approximately at the mid span location and close to the middle of the entire width of the bridge. Instrumentation was placed on the middle of the three girders in the structure. In Region 1, the location of the instrumentation was approximately 7.0 m from one of the abutments on the second girder.

Thermocouples

The instrumentation plan allows for measuring the temperature of concrete after casting, through set and early strength gain. Temperature was obtained from two points, at different depths inside the slab. (as shown in Figure 21). The gage located close to the top/bottom surface of the bridge deck was in the same plane as the top/bottom layer of steel reinforcement. In addition, temperature of the steel girder, directly below the concrete and the ambient air temperature were also recorded. One surface mounted thermocouple gage was attached to the bottom surface of the top flange of the steel girder approximately at the mid span location. In Region 3, a second thermocouple gage was attached to the web of the girder close to the top flange. The ambient air temperature directly below the top flange of the steel girder was monitored by leaving one thermocouple exposed to the air.

Strain Gages

The strain in concrete was measured from immediately after casting using embedded vibrating wire strain gages. Strain was obtained from two points, at different depths inside the slab. The strain gages were installed after the formwork for the concrete deck was in place and prior to pouring the concrete. Two embedded vibrating wire gages were placed in the longitudinal direction (direction of traffic) as shown in Figure 21. The gage located close to the top/bottom surface of the bridge deck was in the same plane as the top/bottom layer of steel reinforcement. In addition, a third embedded vibrating wire gage was placed in the transverse direction, located in the same vertical plane as the other two gages (shown in Figure 21). The strain gages were attached to the rebars using plastic ties after the formwork and the rebars for the bridge deck had been placed.

Two vibrating wire strain gages were attached to the steel girder. One gage was attached to the bottom surface of the top flange of the steel girders in the longitudinal direction (direction of traffic) as shown in Figure 21. The second gage was attached to the bottom flange. The strain gages were epoxy mounted to the steel girders.

Data was recorded from the thermocouples and the strain gages at five minute intervals using data-loggers. For Region 3, data collection was initiated at 14:55PM in the afternoon and casting started at 8:00AM the next day. Data collection from Region 1 was started on the day before casting at 12:20PM in the afternoon. Casting was started approximately 7:45AM in the morning.

Section A-A

Section B-B
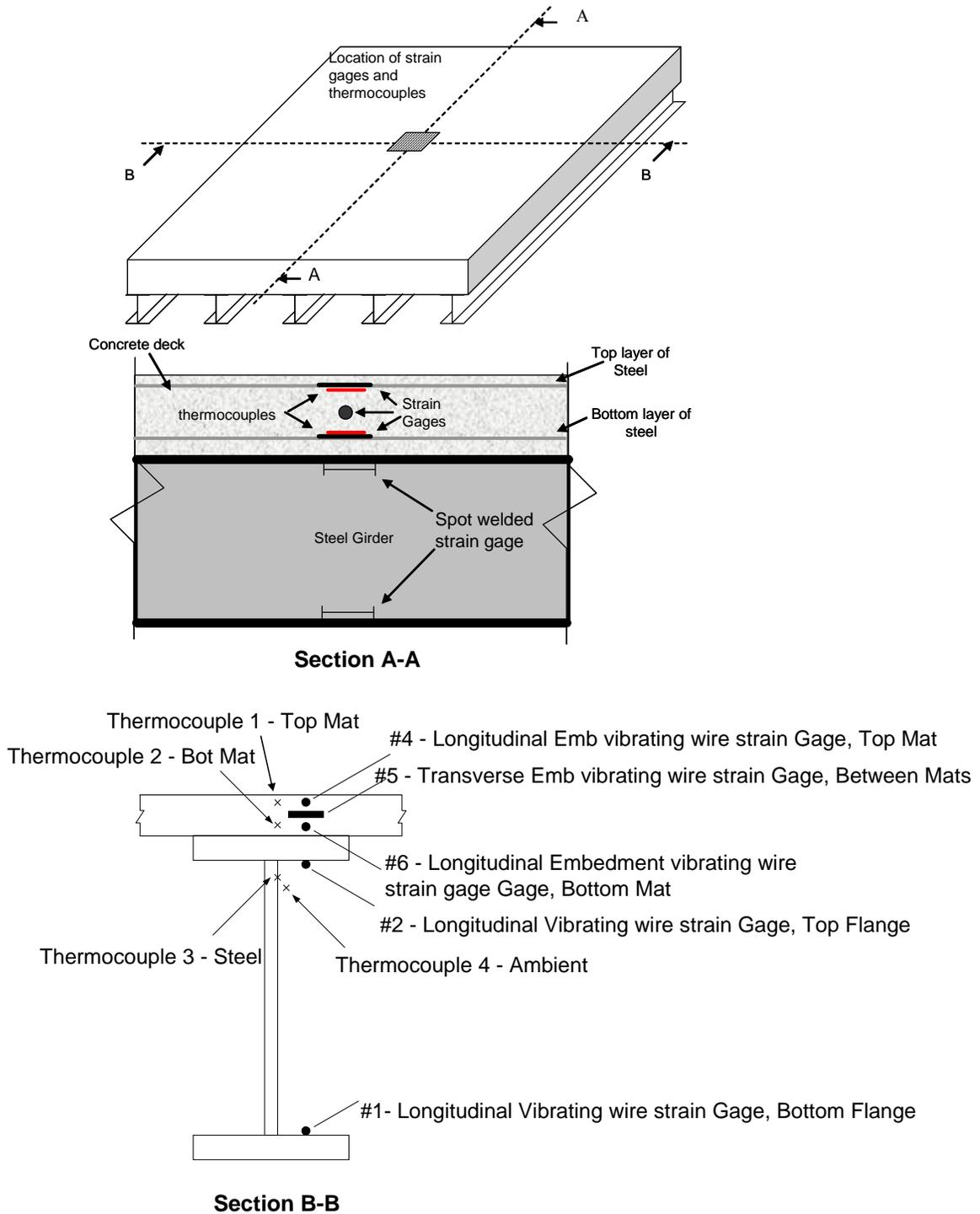
Figure 21: Location and layout of the thermocouple and train gage sensors in the bridge in Region 3 (Instrumentation for Region 1 is similar except Thermocouple 3 not present).

3.5.1 Measured Parameters and their significance

<u>Temperature</u>

The temperature values from the concrete deck and the steel girder were recorded directly in Celsius units by the data logger. The following information was obtained from the recorded temperatures:

(a) the temperature differential through the deck during the temperature rise due to heat released from cement hydration and the subsequent cooling to ambient levels;

(b) the temperature differential within the concrete deck during a day produced by heating which occurs from solar radiation; and

(c) The temperature rise in steel girder during hydration and subsequent daily temperature variation due to heating of the deck from solar radiation.

Strain in concrete deck

The recorded strains from concrete provide information about the thermal expansion and contraction of concrete. The strain measured in concrete in the early age, when concrete has very low stiffness, is indicative of the expansion of concrete due to the heat released during hydration. Subsequent strains in concrete are produced by a combination of temperature change and shrinkage. Any differential strain, due to differential shrinkage and/or temperature distribution between top and bottom is indicative of bending or curling of the slab.

Strain in steel girders

The changes in strain resulting from (a) dead load produced by the concrete deck; (b) temperature change produced by hydration and subsequent cooling to ambient temperature levels; and (c) daily temperature cycles, were recorded. Initially, after casting the concrete slab, the change in the recorded strain corresponds to the additional deflection of the steel girder produced by the weight of the slab. Subsequent variations in strain after placing the concrete are a result of stress transfer between concrete and steel. Since the steel beam is elastic throughout the process, the strain measured on the steel beam is indicative of composite action.

3.4.2 Interpreting data from vibrating wire strain gages

The strain recorded by the data-logger from the vibrating wire strain gage corresponds with the change in the tension of a steel wire due to applied mechanical and environmental loads. Strain is measured from the tension in a steel wire, which is stretched between two gage points. The gage points are attached to the structural member. Due to applied stress, any movement between the gage points produces a change in the tension of the wire. The tension in the wire is determined from the resonant frequency of the vibrating wire. Temperature changes can also produce changes in the tension of the wire. Therefore, when temperature changes are involved it is important to provide temperature compensation for the recorded strains.

The strain recorded by a vibrating-wire strain gage attached to the surface of a steel member for three different cases comprising of a) unrestrained free thermal movement; b) partial restraint to thermal movement; and c) fully restrained against thermal movement is illustrated in Figure 22. If we consider the thermal movement produced by a drop in temperature (ΔT is negative), the relationship between the strains measured by the vibrating

wire strain gage, the stress in the steel member and the actual strain which produces displacement of member is explained below for each of the three cases.

(a)

$\sigma_a = 0$ $\alpha\Delta T$
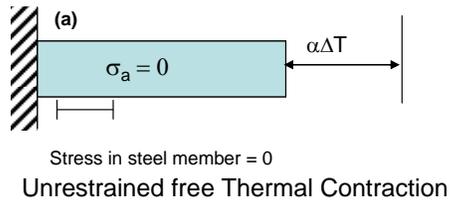
Imposed strain produces movement of gage points = $\alpha\Delta T$ (comp)

Increase in strain of wire due to thermal contraction = $\alpha\Delta T$ (tension)

Net strain recorded by gage = 0

Stress in steel member = 0

Unrestrained free Thermal Contraction

(b)

ε_{meas} ε_{true}

σ_b $\alpha\Delta T$
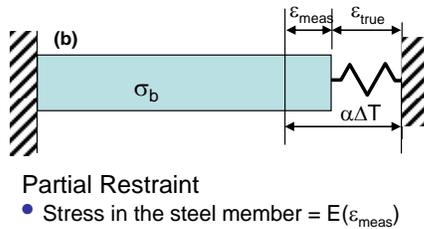
Imposed strain produces movement of gage points = ε_{true} (comp)

Increase in strain of wire due to thermal contraction = $\alpha\Delta T$ (ten)

Net strain recorded by gage, $\varepsilon_{meas} = \alpha\Delta T - \varepsilon_{true}$ (tension)

Partial Restraint

• Stress in the steel member = $E(\varepsilon_{meas})$

(c) $\varepsilon_{meas} = \alpha\Delta T$

$\sigma_{\text{Full restraint}} > \sigma_b$
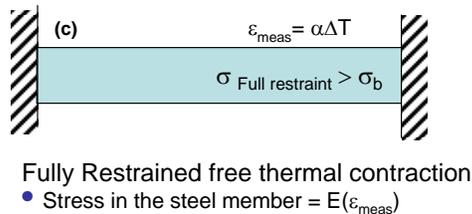
Imposed strain produces movement of gage points = 0

Increase in strain of wire due to thermal contraction = $\alpha\Delta T$ (tension)

Net strain recorded by gage, $\varepsilon_{meas} = \alpha\Delta T$ (tension)

Fully Restrained free thermal contraction

• Stress in the steel member = $E(\varepsilon_{meas})$

Figure 22: Relation between ε_{meas} and ε_{true} for the cases of (a) unrestrained; (b) partially restrained and (c) fully restrained thermal contraction of a steel member.

Unrestrained thermal contraction – In this case, the drop in temperature produces a free contraction of the steel member and hence there is no stress in the structural member. The thermal movement of the steel member produces a relative movement between the gage points of the vibrating wire gage equal to $\alpha\Delta T$. This would produce a decrease in the tension of the steel wire. Concurrently, there is an increase in tension of the steel wire associated with the drop in temperature due to thermal contraction of the wire which is equal to $\alpha\Delta T$. Therefore the net change in tension of the wire due to the two counteracting effects is equal to zero. Hence the vibrating wire would read a strain equal to zero.

Partially restrained thermal contraction – In this case, the thermal contraction produced by the drop in temperature, ε_{true} is smaller than the unrestrained thermal contraction, $\alpha\Delta T$. The gage points of the vibrating wire strain gage are subjected to a movement produced by ε_{true}, which produces a decrease in tension of the wire. Concurrently, there is an increase in the tension of wire associated with the drop in temperature due to thermal contraction of the wire, which is equal to $\alpha\Delta T$. Since the free thermal movement is restrained, ε_{true} is smaller than $\alpha\Delta T$. Thus there is a net increase in the tension of wire due to these two effects. The increase in tension of the wire corresponds to the level of restraint of the free thermal movement of steel. The vibrating wire strain gage would thus record a tension strain, ε_{meas} while the steel structural member undergoes a contraction equal to ε_{true}. To recover the strains

due to thermal movement, the strain due to free thermal contraction, $\alpha\Delta T$ should be added to the measured strain, ε_{meas}. The partial restraint to the free thermal contraction of the structural member results in tensile stresses which are proportional to the level of restraint. The level of restraint is equal to the difference between the free thermal contraction and the actual strain the structure. From Figure 22, the level of restraint is therefore equal to ε_{meas}.

<u>Fully restrained thermal contraction</u> – In this case there is no movement of the steel member due to the temperature change. Thus the gage points of the vibrating wire strain gage experience no relative movement. There is however an increase in the tension of the wire due to thermal contraction, which is equal to $\alpha\Delta T$. Thus, there is a net increase in the tension of wire due to the decrease in temperature. The vibrating wire strain gage would record a net tension strain, ε_{meas} equal to $\alpha\Delta T$, while the true strain in the steel member, ε_{true} is equal to zero. Thus the true strain can be obtained by adding the free thermal strain, $\alpha\Delta T$ to the measured strain. The structural member is in tension due to the restrained movement and the stress is proportional to $\alpha\Delta T$.

When using vibrating-wire strain gages, a distinction must be made between the measured strain (ε_{meas}) and the true strain (ε_{true}). ε_{meas} is the strain measured using the vibrating wire strain gage for changes in applied loading and temperature. ε_{true}, which corresponds to the actual movement of the structure due the changes in the load and temperature, is obtained by adding $\alpha\Delta T$ to ε_{meas}.

Another point to note is that when the vibrating wire strain gage is attached to a steel structural member, ε_{meas} is equal to the level of restraint to free thermal movement. <u>Thus the strain recorded by the vibrating wire strain gage multiplied by the elastic modulus of steel provides the stress in steel structural member due to restraint to its free thermal movement.</u> If the load-induced strain is subtracted from ε_{meas}, the resulting strain is proportional to the stress due to restraint of thermal movement.

3.6 Results of Instrumentation

The temperatures recorded from the concrete and top flange of the steel girder for Regions 3 and 1 are shown in Figures 23 and 24, respectively. The temperature of the top and bottom of the slab, at depths corresponding to the top and bottom steel rebar are plotted in the graph. The time equal to zero on the graph corresponds with the time when casting was started. The ambient temperature recorded at the Elmira station (for Region 3) and the Albany Station (for Region 1) by the National Oceanic and Atmospheric Administration (NOAA) is also plotted in the figure for comparison. From the temperature profiles the following observations can be made.

a. There is a 10-20 deg C daily variation in the ambient temperature. There is a steady increase in the average ambient temperature after casting.

b. Before casting, there is a large temperature differential between the top and bottom flanges of the steel girder approximately 12 hours before casting. In Region 3, the temperatures of the top and bottom flanges are approximately 43 and 26 deg C, respectively, when the ambient temperature is equal to 25 deg C. As the ambient temperature decreases, the temperature differential also decreases.

35

c. Initially, after casting there is a rapid temperature rise due to the heat released by concrete.

d. In Region 3, the maximum temperature of concrete occurs approximately 9.5 hours after casting while the maximum temperature in top flange of the girder occurs approximately 12.0 hours after casting. In Region 1, there is a similar time lag between the maximum temperatures recorded in the concrete and the top steel flange.

e. 72 hours after casting, the changes in temperature of the steel girder and the concrete deck reflect the changes in the ambient temperature. There is an increase in the average temperature of the girders and the deck which corresponds well with the increase in the average ambient temperature between 48 and 144 hours.

f. After 72 hours, there is a slight lag between the ambient temperature changes and those recorded from the concrete deck and the girder.
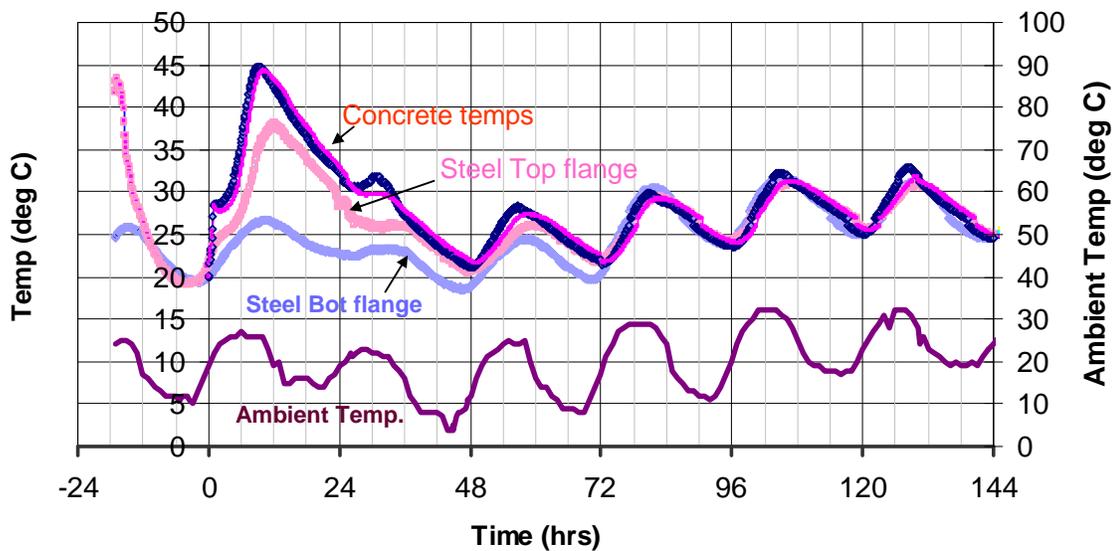

Figure 23: Temperature recorded from the bridge deck and steel girder for the bridge in Region 3.
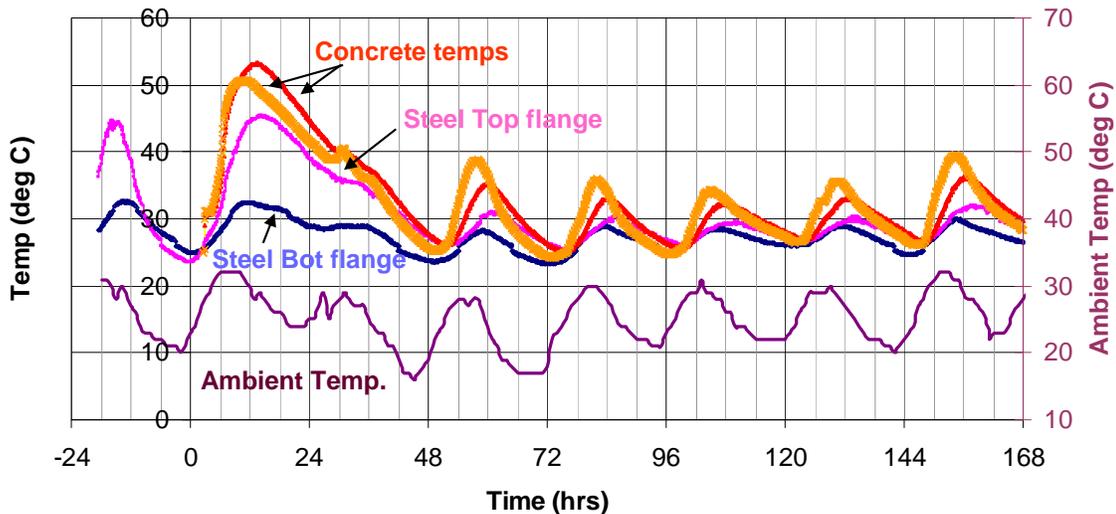

Figure 24: Temperature recorded from the bridge deck and steel girder for the bridge in Region 1.

Comparing the temperature variations recorded from the 2 bridges, the following can be observed

1. The temperature rise in both steel and concrete is higher in Region 1 than in Region 3.

2. In Region 3, the temperature profile across the entire cross-section becomes uniform 72 hours after casting. There is however a temperature differential between the concrete and the steel and also across the depth of concrete slab in Region 1. The temperature differential increases with heating during the day and decreases with cooling. The relative pattern of temperature differential between steel and concrete remains constant with time.

There are two possible contributing factors for the temperature rise in Region 1 being higher than that for Region 3: a) The average ambient temperature for Region 1 was higher than that for Region 3; and b) the dimensions of the concrete slab in Region 3 are smaller than the dimensions of the slab in Region 1. Explaining the temperature profiles in the bridge requires an understanding of the heat flow patterns in the bridge.

The heat flow patterns in the bridge in the time corresponding to a) before casting; b) in the first 48 hours after casting; and c) after 48 hours of casting are shown in Figure 25.

- Before casting only the top flange of the steel girder receives direct solar radiation. The stay-in-place form work shields the bottom flange from direct exposure to the sun. This sets up a temperature differential between the top and bottom flanges in the steel girder. The temperature differential results in conduction of heat from the top flange to the bottom flange. The web and the bottom flange lose heat to the environment through the radiation and the convection mechanisms. Subsequently, in the evening when the ambient temperature decreases and the solar radiation not present, the entire steel girder radiates heat to the environment. Some heat is also transferred to the air through the convection mechanism.

- In the first 48 hours after casting, there is internal heat generated inside concrete which is controlled by the hydration reaction. The temperature of the concrete is higher than the ambient temperature. While the ambient temperature controls the rate of hydration reaction, the concrete loses heat to the surroundings through radiation and convection. The incident solar energy is also absorbed by the concrete during the day. The amount of thermal energy absorbed by concrete would depend upon its thermal properties such as absorption coefficient. The radiant heat energy absorbed by the concrete and the ambient temperature serve as external input to the exothermic hydration reaction, thereby influencing its rate, which in turn controls the internal heat generated within concrete. The recorded temperatures indicate that the concrete is at a higher temperature than the steel girder throughout the 48 hour period. Hence, there is a flow of heat from concrete to the steel girder by the conduction mechanism. This sets up a temperature differential between the top and the bottom flanges of the steel girder. The temperature differential results in conduction of heat to the bottom flange. The web and the bottom flange lose heat to the environment through the radiation and the convection mechanisms.

- After 48 hours the temperature of concrete shows 24 hour cycles, which closely follows the ambient temperature. During the day, the concrete is heated by the solar radiation. This creates a temperature differential between the concrete and the steel girder, which results in heat flow from concrete to steel by conduction. The temperature changes

produced in concrete and steel depend upon the radiation input on the concrete surface, the thermal conductions of concrete and steel. During the cooling period when the there is no incident solar radiation and the ambient temperature decreases, the concrete, which is hotter than the surrounding air, radiates heat to the environment. Heat is transferred from the steel girder to the surrounding air by radiation and convection. This sets up heat flow from within the concrete slab to the concrete surface and the steel girder. The existence of temperature gradient across concrete after 48 hours may be related to efficiency of heat transfer between concrete and steel and also to the mass of concrete, which results in thermal inertia.

The exact temperature distribution in the steel and concrete during the three stages depends upon several factors such as the thermal conductivities of concrete and steel, the thermal absorption of concrete, the input thermal energy, the internal heat generated within concrete during hydration, the radiant energy input from the solar radiation, wind velocity etc. This problem is further complicated by the fact that the thermal properties of concrete change as a function of time.
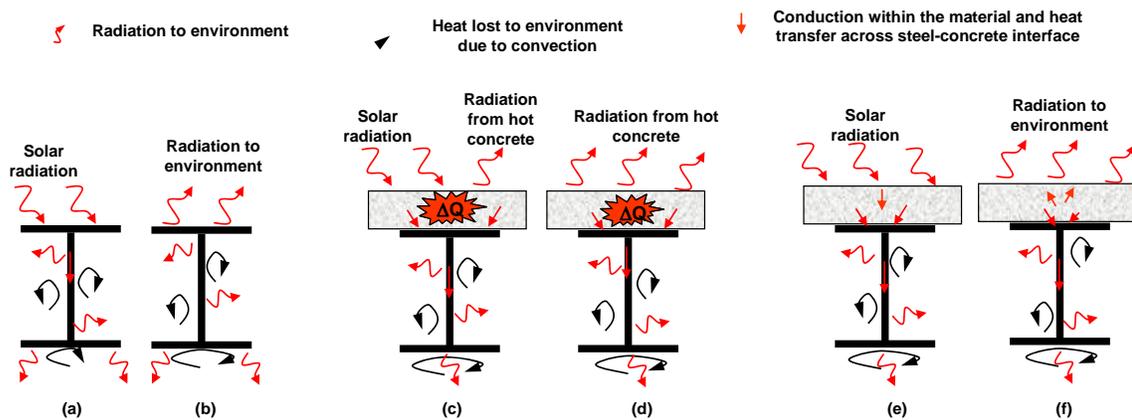
Figure 25: Heat flow patterns in the steel girder and concrete slab: (a) during day before casting; (b) during evening and in the night before casting; (c) during the day in the first 48 hours after casting; (d) during the evening and night in the first 48 hours after casting; (e) during the day 48 hours after casting; and (f) during the evening and night after 48 hours of casting.

3.6.1 Strain results

A comparison between ε_{meas} and ε_{true} for the top and bottom flanges for Region 3 are shown in Figure 26(a) and (b). Time zero in the graph corresponds with the start of casting. For the period before casting, there is an increase in ε_{true} for both the top and bottom flanges with an increase in temperature (variation in temperature shown in Figure 23). ε_{meas} of the top flange in this time period, however, indicates compression. This suggests that the free expansion of the top flange is restrained by the bottom flange, which is at a lower temperature.

Immediately after casting, there is a jump in the strains, both ε_{meas} and ε_{true}, corresponding to the additional dead load of the concrete slab. The polarity of the strains indicates that the top and bottom flanges are in compression and tension, respectively due to the load-induced moment. In the first 12 hours after casting, ε_{true} of the top flange shows an increase which

corresponds with an increase in its temperature. ε_{meas} in this time period increases in compression due to restraint of the free thermal expansion of the top flange. Following the initial temperature rise, the level of compression indicated by ε_{meas} decreases with a decrease in temperature. After 48 hours, ε_{meas} shows a cyclic diurnal variation. ε_{meas} in the bottom flange shows an initial tension due to the moment associated with the weight of the deck slab, after which it remains relatively constant. It can be seen that ε_{true} shows a significant deviation from ε_{meas} after casting both in daily variation and in the average value during a day. The variations in ε_{true} for both the top and bottom flanges after the initial jump associated with the slab weight correspond well with the variation in their respective temperature.
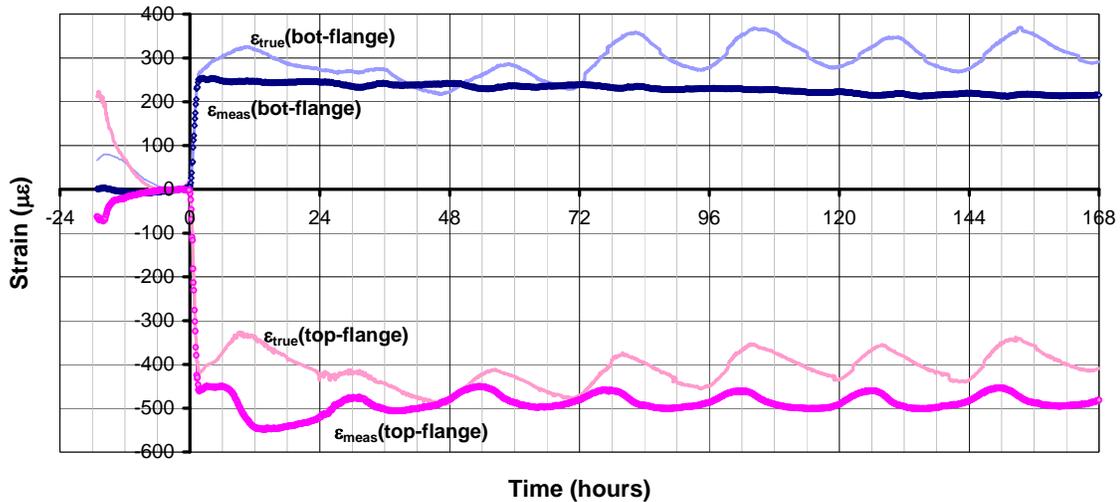
(a)
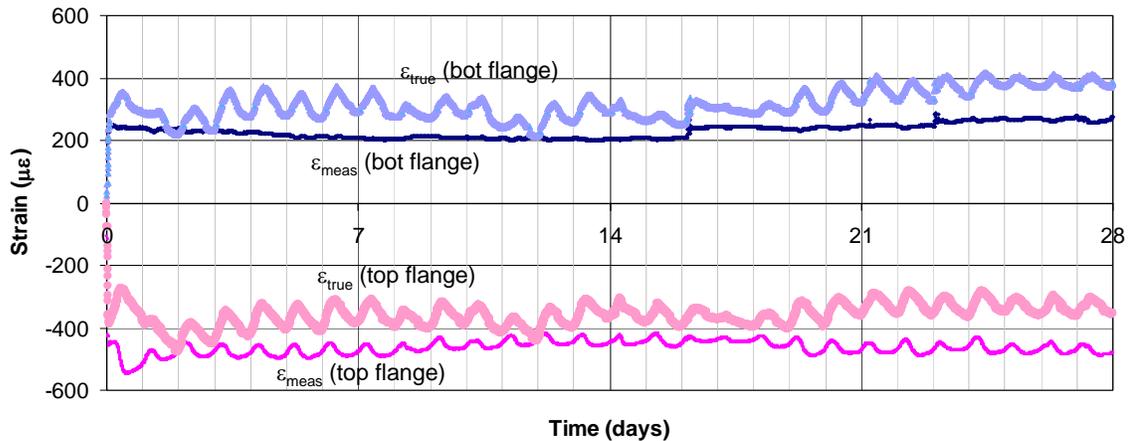
(b)

Figure 26: Comparison of ε_{meas} and ε_{true} for top and bottom flanges of steel girder from Region 3: (a) in the first week; and (b) in the first 28 days after casting.

The temperatures and ε_{true} from the top and bottom flanges of the steel girder after casting for Regions 3 and 1 are shown in Figures 27 and 28, respectively. It can be seen that after the initial change in strain associated with the weight of the slab, there is a continuous change in strain for both flanges. There is an initial increase in both temperature and strain in the first

10-12 hours followed by a steady decrease in both quantities up to 48 hours. After 48 hours, there is a close correspondence between the measured temperature and strain.
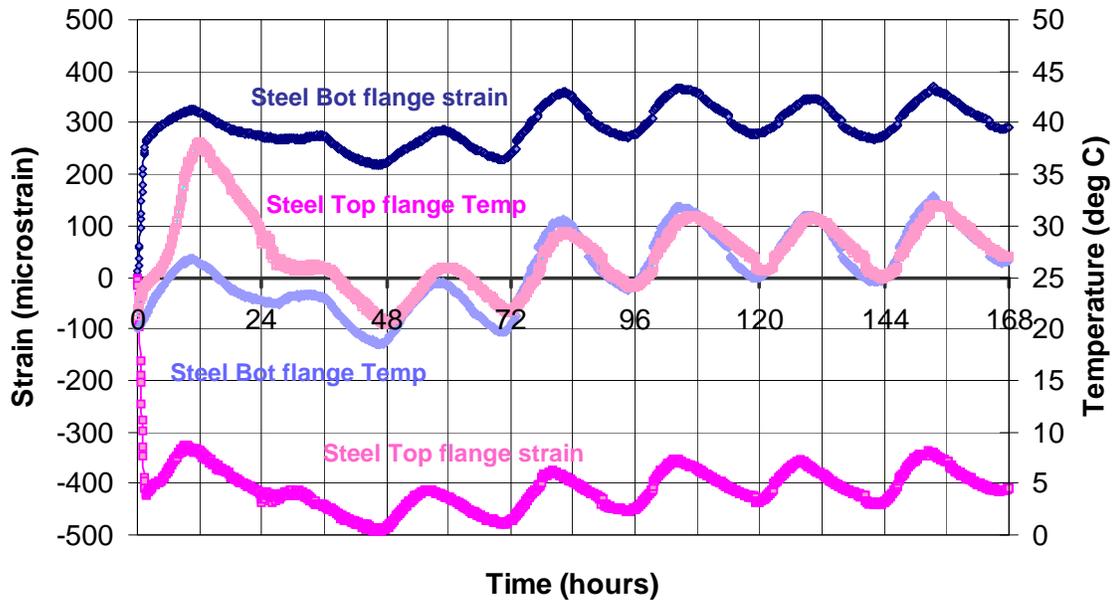
Figure 27: ε_{true} and temperature variation in the top and bottom flanges of the steel girder for Region 3 as function of time after casting.
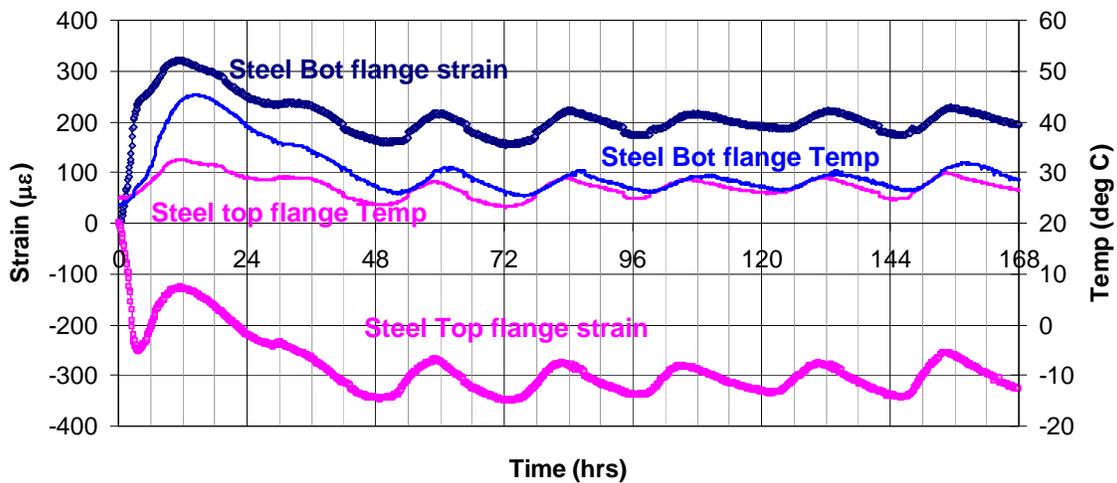
Figure 28: ε_{true} and temperature variation in the top and bottom flanges of the steel girder for Region 1 as function of time after casting

A comparison of ε_{true} from the top flange of the steel girder and the concrete deck after casting for Regions 3 and 1 are is shown in Figures 29 and 30, respectively. In both regions the time zero in the graph corresponds with the time of casting. The strain in the top flange has been set equal to zero at the time corresponding with the initiation of casting. Additional observations which can be made from both regions are given below

- There is an initial decrease in strain of the top flange corresponding with additional dead load of the concrete slab/deck. The initial increase in temperature associated with heat released from concrete produces an expansion in both the concrete and steel followed by a decrease in strain up to 48 hours of time.

- In the first 48 hours after casting there is a larger change in the strain recorded in the concrete deck than that in top flange of steel girder. The strain in concrete due to thermal expansion is larger than that measured in the top flange of the girder. There is also a larger decrease in concrete strain after the initial increase than that of the top flange.

- The variation of strain in the concrete slab and the top flange of the girder are identical after 48 hours of casting. This suggests that complete strain compatibility is established between the top flange of the girder and the concrete slab.

- The variation of strain in the concrete slab and the top flange of steel girder after 48 hours correspond well with the ambient temperature variation. The strain cycles appear to follow the daily temperature cycles. The increase in the average daily temperature corresponds with an increase in the average strain of the daily strain cycles.
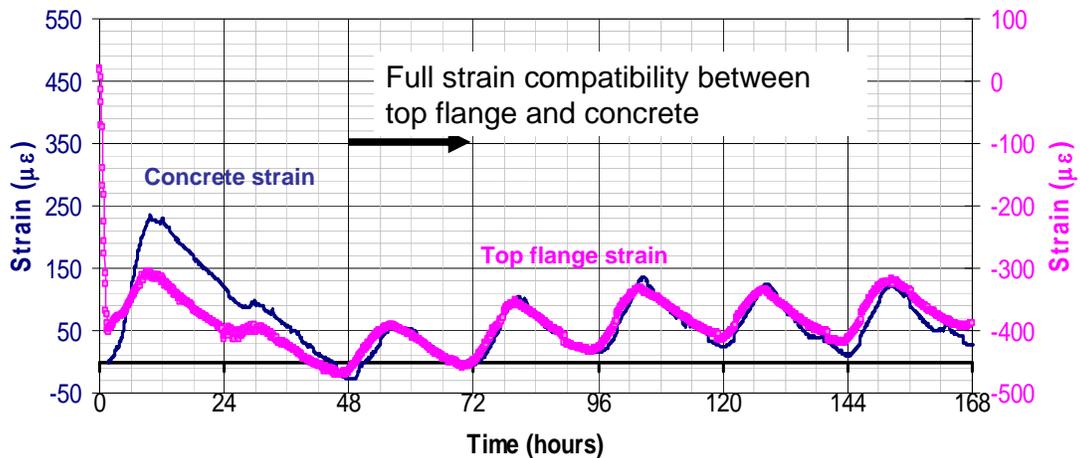
Figure 29: ε_{true} in the top flange of the steel girder and concrete slab for Region 3 as function of time after casting.
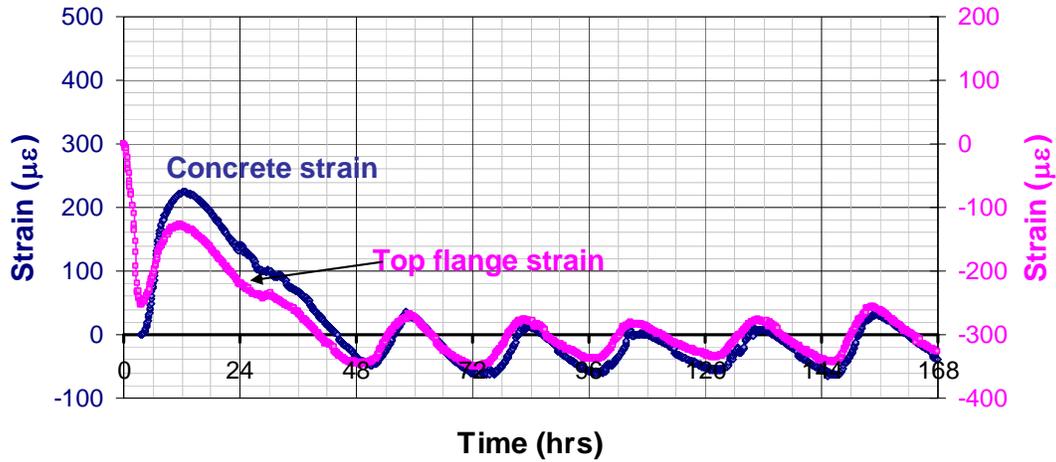
Figure 30: ε_{true} in the top flange of the steel girder and concrete slab for Region 1 as function of time after casting.

3.7 Analysis of Results

While the results of the strains and temperature from both bridges are qualitatively similar, the bridge without skew allows for direct interpretation of strains. This can be evaluated considering the free thermal movements of the slab and the girders separately. There is no change in shape associated with the thermal expansion/contraction of a rectangular plate. Thus, the measured strain along orthogonal directions, in the direction of the span and perpendicular to the span of the bridge, correspond with the movement of the edges of the plate. The principal directions of thermal contractions of the bridge deck and the girders coincide in the case of a rectangular slab. Free thermal expansion or contraction of a skew plate results in a change in shape. In a skew slab, the measured strains in the two orthogonal directions do not coincide with the free movements of the edges. The measured strains in a skew slab cannot be directly related to the dimension changes along its boundaries. Thus the principal directions of the free thermal expansion/contraction of the concrete deck and the girder do not coincide with each other.

This is illustrated in Figure 31, considering the free thermal contraction of a portion of the slab (both with and without skew) labeled 0123 (Figure 31a and 31b for bridges without and with skew, respectively). In both cases the segment 01 of the slab coincides with the segment AB located in the girder along its axis. The final configuration of the slab due to thermal movements associated with a reduction in temperature is shown as $0'1'2'3'$ (Figure 31a and 31b for bridges without and with skew, respectively). In the plan view, the lower left corner of the slab and Point A of the line segment before and after thermal strains are aligned. It can be seen that the edges of the skew slab do not remain parallel after thermal contraction. There is thus a significant rotation of lines initially aligned with the edges of the slab. If free thermal contraction of the slab is allowed, the line segments in the concrete slab initially aligned with the axis of the girder would not be aligned with the axis of the girder after thermal deformation. The deformation of the steel girder due to temperature stains is along the axis of the beam.

In a bridge structure, the free thermal movement of the slab is not permitted because of the restraint from the girders. The longitudinal restraint caused by the girders and transverse restraint caused by the diaphragms would force the edges of the deck slab to remain parallel to the axis of the girder. The resulting state of stress in the deck with skew is significantly more complex than in the case of the concrete deck without skew. Predicting stress from the measured strains therefore requires a full three-dimensional analysis of the structure.

While two bridges, one each in Regions 3 and 1 were instrumented with both strain gages and thermocouples, the bridge in Region 1 had a significant skew, approximately equal to 32 degrees. The results of the bridge from Region 3 are hence analyzed in greater detail, since the lack of skew provides a means of relating the measured strains with stresses in the materials without a full 3-dimensional analysis.
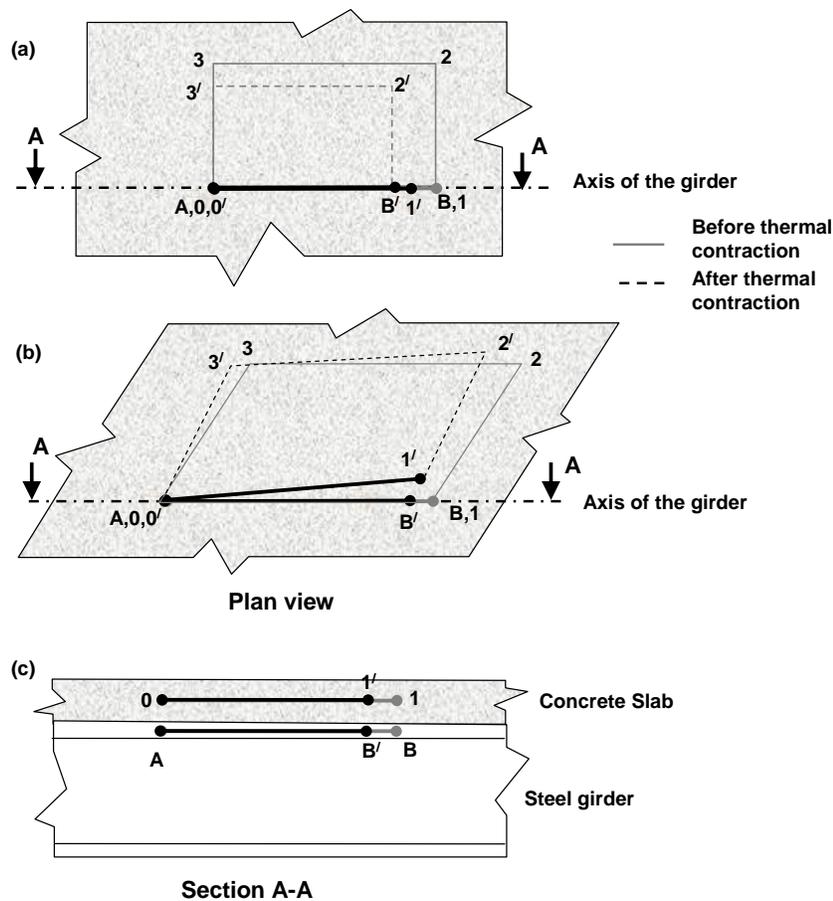
Figure 31: Movements f the girder and the slab due to unrestrained thermal deformations: (a) plan view of a rectangular slab; (b) plan view of skew slab; and (c) Elevation of a section through the axis of steel girder.

3.7.1 Strain Analysis for Region 3 (Bridge without skew)

The true strain in the top steel flange after the initial strain drop due to the concrete slab is subtracted is shown in Figure 32. The ε_{true} for concrete obtained from the embedded strain

gage is also shown in the figure. The free thermal strain of the rebar due to the temperature changes recorded in the concrete, which is calculated by multiplying the coefficient of thermal expansion of steel by the temperature change after casting is shown by the line labeled $\alpha\Delta T$. It can be seen that initially after casting the expansion measured in concrete corresponds well with the free thermal strain of the rebar. There is a deviation between the free thermal strain of the rebar and the ε_{true} of concrete approximately 8-9 hours after casting. It is interesting to note that while the temperature in concrete starts to decrease after 9.5 hours, the strain in concrete does not decrease until 12.0 hours after casting. The contraction of the concrete corresponds in time with the observed decrease in strain in the top flange. This suggests that the free thermal contraction of the concrete is restrained by the top flange. Therefore tensile stresses may develop in the concrete immediately following the temperature rise produced by cement hydration. During the cooling period which lasts up to 48 hours, there is a larger decrease in ε_{true} of concrete than that of the top flange. This suggests that there is relative movement between the concrete deck and the top flange within this period. After 48 hours the ε_{true} of the concrete deck is parallel to that of the top flange, which indicates full strain compatibility.
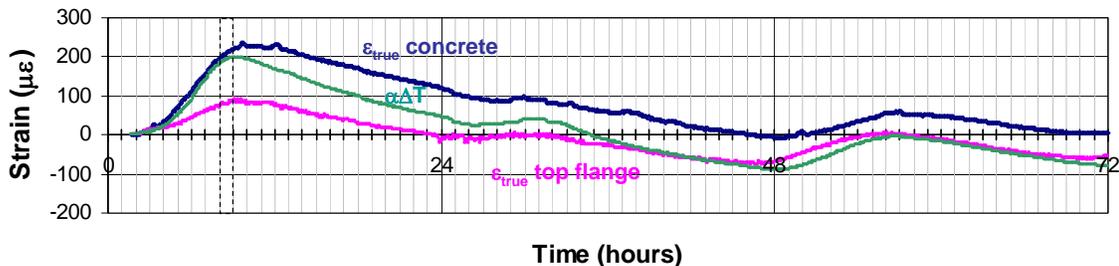
Figure 32: ε_{true} of the concrete slab and the steel girder for a period after completion of casting.

A comparison of the ε_{true} and the unrestrained thermal strains for the measured temperature change for the top and bottom flanges are shown in Figures 33 (a) and (b), respectively. The unrestrained thermal strains are obtained by multiplying the temperature change by the co-efficient of thermal expansion of steel (12.2×10^{-6} m/m/^{o}C). The strain due to the bending moment associated with the weight of the slab has been subtracted from the ε_{true} for both flanges. The difference between the unrestrained thermal strain and ε_{true} represents the level of restraint to free thermal movement. It can be seen that the ε_{true} for the bottom flange is approximately equal to the unrestrained thermal strain indicating little restraint to its thermal movement. There is however a significant difference between the unrestrained thermal strain and ε_{true} for the top flange before and after casting of the slab. This indicates a significant level of restraint to its thermal movement. The restraint to the thermal movement of the top flange before casting comes primarily from the remaining steel girder. After casting, initially, before setting, the contribution of concrete to the level of restraint is not significant. The contribution of concrete to the level of restraint increases with time after casting as concrete gains in stiffness.
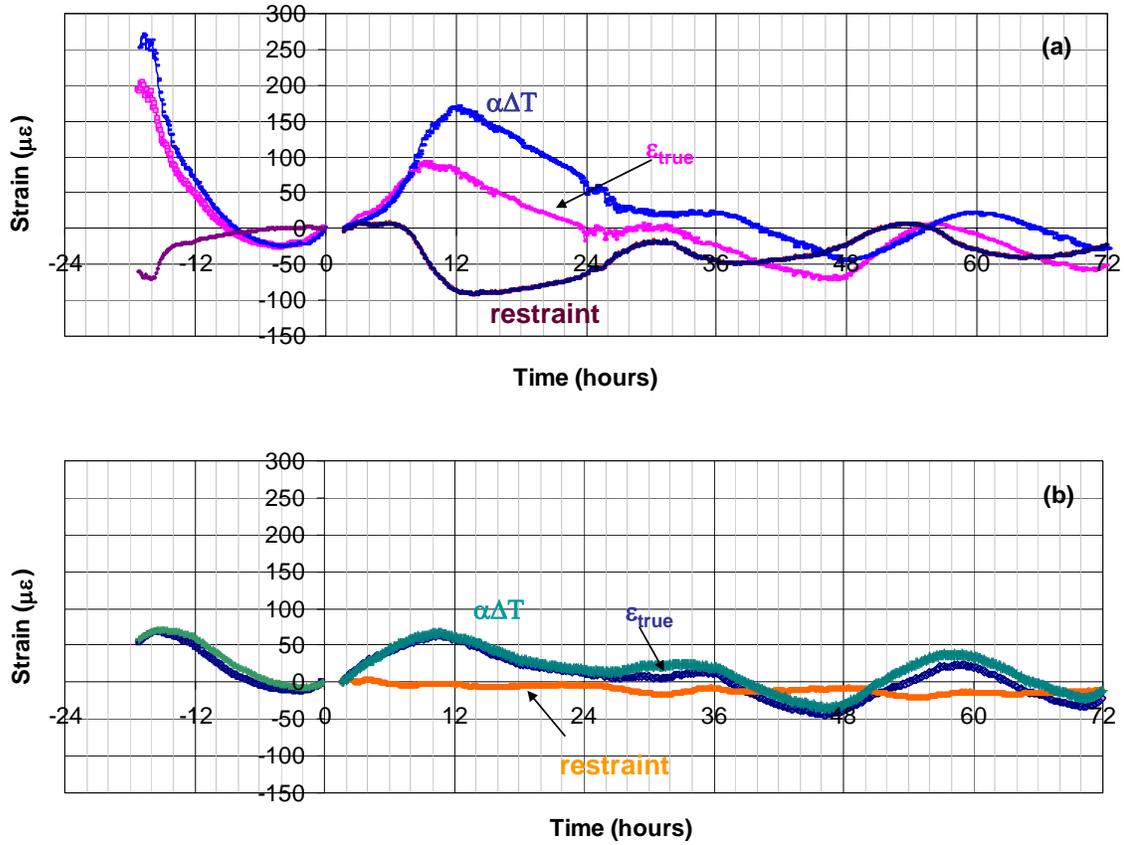
Figure 33: ε_{true} in the flanges of the steel girder for a period after completion of casting: (a) top flange; (b) bottom flange.

Non-uniform heating of the beam results in stresses in the steel since the free expansion of the top flange with rising temperature cannot proceed freely. The stress due to restrained thermal movement can be evaluated using the method of strain suppression (Timoshenko and Goodier1970). The resulting stresses in the at a location, y, from the neutral axis of the beam due to temperature distribution, $T(y)$ is given as

$$\sigma_x(y) = -\alpha E T + \frac{\alpha E}{A} \int\limits_{-c_1}^{c_2} T b \, dy + \frac{(\alpha E)y}{I} \int\limits_{-c_1}^{c_2} T b y \, dy \tag{1}$$

where b is the width of the beam as a function of y, c_1 and c_2 are the location of the bottommost and topmost fibers of the beam, I is the moment of inertia of the beam and α is the co-efficient of thermal expansion. The stress at location y_1 can be rewritten as

$$\sigma_x(y_1) = -\alpha E T(y_1) + \frac{\alpha E}{A} \int\limits_{-c_1}^{c_2} T(y_1) dA(y) + \frac{(\alpha E)y_1}{I} \int\limits_{-c_1}^{c_2} T(y) y \, dA(y) \tag{2}$$

The first integral corresponds with the average temperature over the area of the entire beam. The second integral corresponds with the first moment of the temperature about the neutral axis.

45

In a typical bridge girder, the areas of the top and bottom flanges are larger than the area of the web and the moment of areas of the flanges is significantly larger than that of the web. The contribution of the temperature distribution in the web to the restrained stress can be thus be neglected. Further, the temperature of the top and bottom flanges can be assumed to be constant over the entire area of each flange. The stress in the top flange due to restrained thermal movement can therefore be simplified as

$$\sigma_x(c_2) = -\alpha E T_2 + \frac{\alpha E}{A}[A_1 T_1 + A_2 T_2] + \frac{\alpha E c_2}{I}[T_2 A_2 c_2 - T_1 A_1 c_1]$$

(3)

where A_1 and A_2 are the areas of the bottom and top flanges, T_1 and T_2 are the temperatures of the bottom and top flanges and c_1 and c_2 are the distances from the neutral axis to the bottom and top flanges..

The measurements from the steel girders for both bridges prior to casting indicate that the temperatures of the top and the bottom flanges are approximately equal during a few hours before casting. Thus it can be assumed that the temperature is relatively uniform across the entire cross-section of the girder during this period. Therefore the stress due to restraint of free thermal expansion can be assumed to be zero in this period. For computing the stresses in the steel girder before casting, the stress in the top flange at the time of casting is assumed to be zero. The stress in the top flange was then computed using Equation 3 for the time extending backwards from the time of casting up to the time of initiation of data collection. A comparison of the ε_{meas} and the computed strain for the top flange is shown in Figure 34. The computed strain due to restrained thermal movement was obtained by dividing the stress obtained from Equation 3 by the modulus of elasticity of steel. It has previously been established that ε_{meas} obtained from the vibrating wire strain gage mounted on a steel substrate is directly proportional to the stress due to restrained thermal movement. The temperature differential between the top and the bottom flanges during this time is also shown for comparison. It can be seen that there is favorable comparison between the ε_{meas} and that predicted by Equation 3. This suggests that the prediction obtained from Equation 3 provides an accurate estimate of the stress in the top flange due to the restraint of its free thermal movement from the remaining girder.
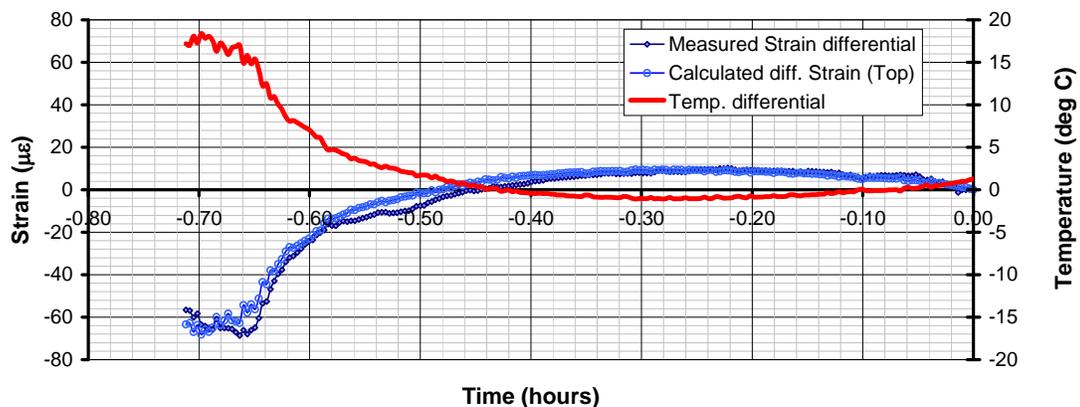
Figure 34: Comparison of measured and predicted strains in the top flange of the steel girder before casting of the concrete slab.

ε_{meas} in the top flange after casting contains contributions from load-induced strain due to the weight of the slab and the restrained thermal movement. The sum of the load-induced strains and the restrained thermal movement, which was computed using Equation 3 from measured temperatures, is shown in Figure 35. The weight of the slab is entirely supported by the steel girder and hence the load-induced strain was calculated using the Euler-Bernoulli beam equation and the section properties of the steel girder. The ε_{meas} from the top flange and the temperature differential between the top and bottom flanges are also shown in Figure 35. It can be seen that immediately after casting the calculated strain agrees very well with ε_{meas} up to Point O. Following Point O, as the temperature difference between the top and the bottom flanges increases, the calculated value of strain deviates significantly from ε_{meas}. The deviation between the calculated and the measured strains indicates that the strain computed using only the contribution of the steel girder is not accurate. The computed level of restraint obtained using only the steel girder is also smaller than that from measurement. This indicates that the concrete deck also contribute to the level of restraint of the free thermal movement of the top flange. The occurrence of Point O in the strain response corresponds approximately in time with the indication of restraint to free thermal contraction of concrete in Figure 32. The predicted strain deviates from the measured strain obtained considering the response of steel girder alone at a time when the free contraction of the concrete slab is restrained by the top flange. This suggests that there is an initiation of the composite action between the top flange and the concrete slab at this time.
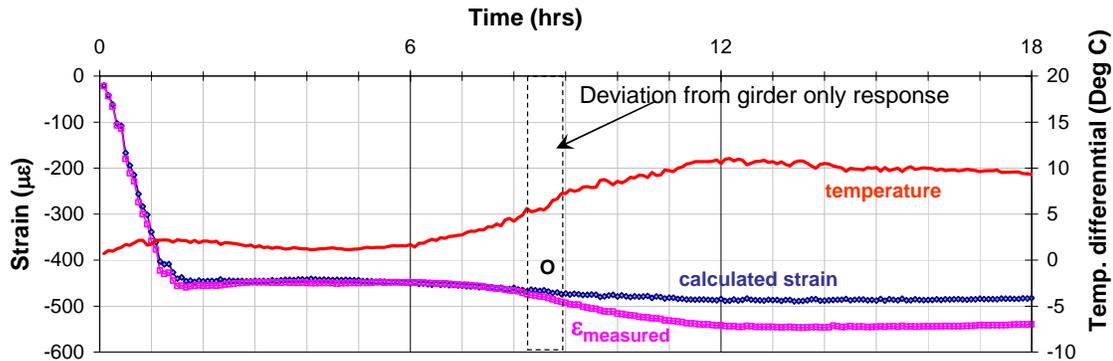
Figure 35: Comparison of measured and predicted strains in the top flange of the steel girder during and after casting of the concrete slab.

Immediately after casting, the strain measured by the vibrating wire strain gage corresponds with the load induced strain from the weight of the concrete deck. Subsequently, the variation in ε_{meas} is due to the restrained free thermal expansion of the flange. While the strain due to the imposed loading is of a constant magnitude, the strain due to restrained thermal expansion varies with time. Initially after casting, since the concrete has negligible stiffness, the stress in the top flange due to restrained thermal expansion can be computed using Equation 3. With time as the concrete gains stiffness, there is additional restraint from the concrete. This is illustrated in Figure 36, where the strain in the top flange due to weight of the slab is shown by the line OO'. The deviation of the ε_{meas} from the line OO' indicates the level of restraint against thermal movement. It can be seen that in the first 12 hours after casting, the level of restraint indicated by ε_{meas} is higher than that calculated by considering flanges alone. The influence of concrete in providing restraint to the motion of the top flange

is evident by comparing Points O', A, B and C. The temperature differential between the top and the bottom flanges is equal at these points. The ε_{meas} at A, B and C indicates a higher level of compression in the top flange due to restrained thermal expansion than that at O'. This suggests a higher level of restraint to the free movement of the top flange than that provided by steel girder alone. It can be inferred that the additional restraint is provided by the concrete deck slab as the concrete gains in stiffness.
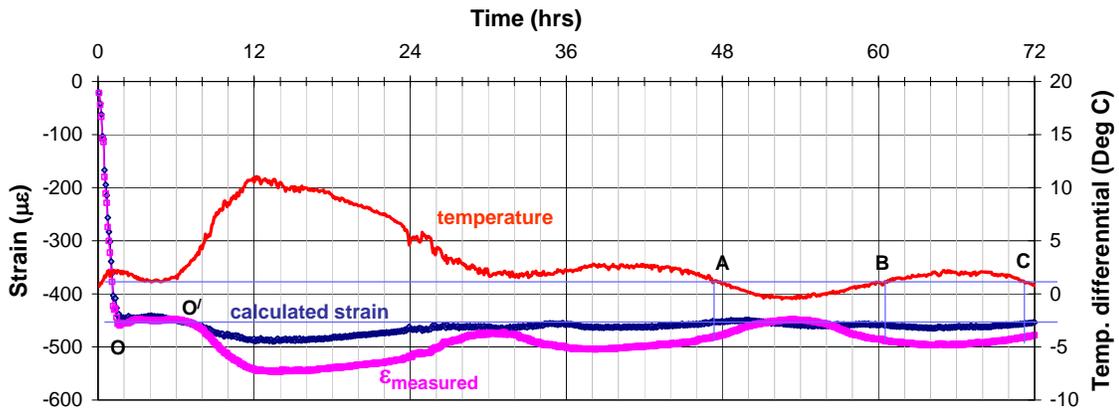

Figure 36: Comparison of measured and predicted strains in the top flange of the steel girder during and up to 72 hours after casting of the concrete slab.

3.7 Discussion

Compiling the information presented so far the following can be summarized:

- There is an expansion of the top flange in the first 12 hours due to the heat released by cement hydration, which is followed by a cooling period lasting up to 48 hours. During the temperature rise there is a temperature gradient across the depth of the steel girder. Thus the free expansion of the top flange is restrained by the web and the bottom flange. During the cooling period, the total contraction of the steel flange would therefore be smaller than the free contraction for the given temperature drop.

- Initially after casting, the expansion strain of concrete corresponds well with the free expansion of the rebar produced by the increase in temperature. Limited strain compatibility between concrete and the top flange is established within the first 10hours after casting. The measured temperature in concrete decreases after 10 hours while the measured strain does not decrease till after 12 hours, which corresponds with the measured decrease in the top flange strain. There is however a relative movement between the concrete deck and the top flange up to 48 hours. The concrete contracts more than the top flange of steel.

- Full strain compatibility is established between the concrete deck and the steel girder after 48 hours. The variation in the top-flange strain corresponds well with its measured temperature variation after the first 48 hours.

It has been reported in literature that the coefficient of thermal expansion of the concrete with a W/C of 0.45 decreases sharply from 32 x 10^{-6}/°C to a value around 10 x 10^{-6}/°C during the

cooling period and then remains almost constant [Kada et al. 2002]. By the time cooling starts, strain compatibility is initiated. If we consider the co-efficient of thermal expansion of steel is $12.2 \times 10^{-6}/^{\circ}C$, the free contraction of the deck is constrained by the top flange. The extent of free contraction depends upon the total temperature drop. The level of constraint, in turn depends upon the difference of free contractions of concrete deck and top flange. However, since the free expansion of the top flange was restrained during the temperature, the total contraction of the top flange would be smaller than the free thermal contraction. This would increase difference between the free thermal contraction of the concrete deck and the total contraction of the top flange resulting in an increase in the tensile stress in concrete at the end of the cooling period. The level of constraint to the top flange depends upon the temperature gradients in the steel beam during the temperature rise. Thus the total magnitude of tensile stress in concrete would depend upon the magnitude of temperature rise and the temperature gradients in the steel girders.

The mechanisms which contribute to stress development in concrete can now be analyzed and are presented in Figure 37. Following the initial expansion, the free contraction of the concrete deck is restrained by the top flange. This would produce tensile stresses in concrete. However, since the creep in concrete is very high at this age, the stress would be decreased quite rapidly. The relative motion observed between the concrete and the top flange could potentially be attributed to two mechanisms which also serve to decrease the stress in the material: (a) creep flow of concrete at early age; and (b) damage in concrete the form of cracking.

After 48 hours the strains in the concrete and the top flange agree well with the measured temperature variation in the two materials. Stress in concrete due to temperature in this stage would be a result of difference in the co-efficient of thermal expansions of the two materials, since the temperature difference between the top flange and concrete deck remains constant (Figure 32). Thus it appears that the role of thermal effects is important in the first 48 hours after casting.

As concrete sets and hardens, there is also a volumetric contraction associated with autogenous shrinkage. Autogenous shrinkage is produced by self-dessication and is common in mixes with low ratio of water/cementitous materials. Autogenous shrinkage starts after the initial setting of concrete and continues to increase with age. The rate of autogenous shrinkage is highest in the first few days after casting and it slows with increasing age of concrete. At a later stage when the concrete is exposed to drying, drying shrinkage acts as a third active mechanism that produces tangible volume change. Drying shrinkage on the other hand, is produced by the drying of concrete, which results in a water loss from the concrete through evaporation. The rate of drying shrinkage is highest after the end of moist curing and it decrease with age of concrete.

The restraint conditions for shrinkage are more severe than those for thermal contraction of the bridge deck (both autogenous and drying). Temperature changes in the girders closely follow those in the deck. Measured strains indicate that the thermal contraction and expansion of the girders coincide with those of the concrete deck. The true strains in both the steel girder and the concrete deck appear to follow the temperature changes. Therefore, the restraint to thermal contraction/expansion of concrete is significantly smaller compared to the restraint to shrinkage, which occurs immediately after setting and continues to increase monotonically with time.

Tensile stress develops in concrete because the free contraction of the concrete deck is restrained by the steel girders. The magnitude of the tensile stress for a given strain is directly proportional to the elastic modulus of the material. Considering the fact that the shrinkage and the elastic modulus of concrete continuously increase as a function of age after casting, there will be a continuous evolution of stress in the material. The stress development in concrete is also influenced by creep/relaxation, which produces a decrease in the magnitude of stress .The magnitude of the tensile stresses at any time is lower than that obtained from an elastic analysis because of the beneficial influence of creep, which produces a relaxation of the stress. The creep coefficient of the concrete also continuously changes with age as the concrete gains strength. Therefore, the tensile stress in restrained concrete continuously increases with time on account of continuing shrinkage and an increase in the elastic modulus with age while the stress relaxation produced by creep decreases the rate of increase of the tensile stress with age. The tensile strength of concrete, and hence its ability to resist cracking, also increases with time. Cracking results when the tensile stress exceeds the tensile strength of concrete.
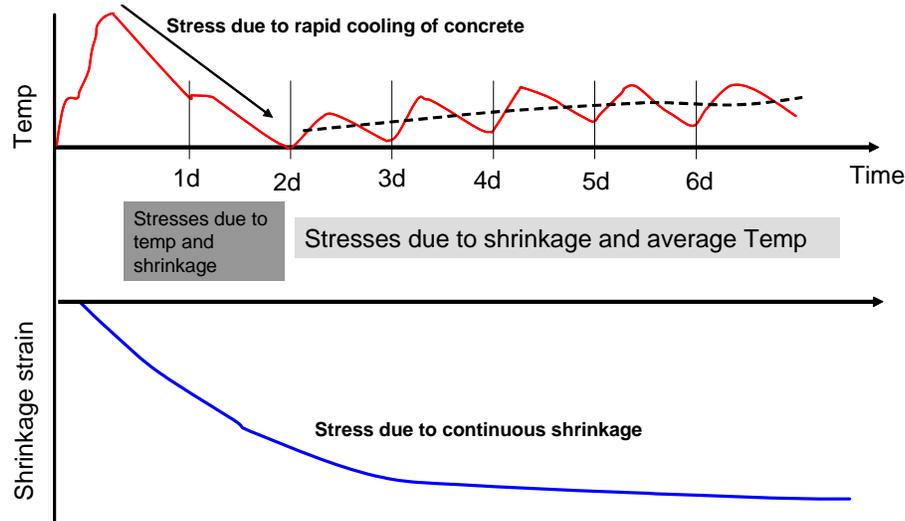
Figure 37: Factors which contribute to tensile stresses in concrete slab.

The results from this study can now be combined with those available in the literature to arrive at an understanding of restrained temperature and shrinkage stresses in bridge decks. In single span bridges, if the girder and the deck slab are free to expand or contract at the supports, there is partial restraint to the thermal contraction immediately following the initial temperature rise produced by hydration. This may result in tensile stress development at the end of the contraction period. If the ends of the deck slab or the girder are constrained at the ends, such as decks which are integral with abutments, there would be a significant tensile stress in the concrete at the end of the cooling period. The stress would increase further with time due to shrinkage. Therefore, the probability of cracking in such bridges is very high. This has been confirmed by an observation of increased cracking in such bridges [Darwin et al. 2004].

In multiple span bridges, where the ends of the girders and deck slab at the abutments are allowed free movement, two separate cases need to be considered. In the first case, where the

girders and the deck are not continuous over the supports, the influence of the thermal movement would be similar to that in a single span bridge with similar support conditions. For bridges where the girders are simply supported and the deck is designed for continuity over the supports, the influence of temperature changes is considerably different. At a pier the girders would contract in the opposite directions. This would create significant tension in the deck slab over the supports. Restrained shrinkage and load induced moments would further increase the level of tensile stress. This would therefore favor cracking in a location over the support even if the deck slab is designed for load-induced moments as reported by Ramey et al. (1997).

Extending the results presented here to bridges with skew requires careful consideration [Farney and Zoghi 2006]. A bridge without skew allows for direct interpretation of strains. There is no change in shape associated with the thermal expansion/contraction of a rectangular plate. Thus, the measured strains along orthogonal directions (along the length and perpendicular to the length of the bridge) correspond with the movement of the edges of the plate. The principal directions of thermal contractions of the bridge deck and the girders coincide in the case of a rectangular deck slab. Free thermal expansion or contraction of a skewed plate, however, results in a change in shape. In a skewed deck slab with parallel skewed supports the movement is not solely in the longitudinal direction. The acute corners of a bridge tend to expand and contract more than the obtuse corners. The measured strains in the two orthogonal directions do not coincide with the free movements of the edges [AASHTO/NSBA 2004]. The measured strains in a skew deck slab cannot be directly related to the dimension changes along its boundaries. Thus the principal directions of the free thermal expansion/contraction of the concrete deck and the girder do not coincide with each other. The longitudinal restraint caused by the girders and transverse restraint caused by the diaphragms would force the edges of the deck slab to remain parallel to the axis of the girder. The resulting state of stress in the deck with skew is significantly more complex than in the case of the concrete deck without skew. Predicting stress from the measured strains therefore requires a full three-dimensional analysis of the structure.

In the current study no significant through-thickness temperature variation was recorded in the concrete deck, 48 hours after casting. Some previous studies have indicated the presence of a temperature gradient across the bridge deck thickness [D'Ambrosia et al. 2005]. Explaining the temperature profiles in the bridge requires an understanding of the bridge's heat flow patterns. The exact temperature distribution in the steel and concrete at any time depends upon several factors such as the thermal conductivities of concrete and steel, the thermal absorption of concrete, the input thermal energy, the internal heat generated within concrete during hydration, the radiant energy input from the solar radiation, wind velocity etc. This problem is further complicated by the fact that the thermal properties of concrete change as a function of time [Wojcik et al. 2001].

The research presented here provides an insight into the early age response of concrete in a steel girder bridge with a composite deck. The level of stress depends upon material, structural and environmental effects. Material composition and environmental conditions influence the expected levels of expansion and contraction. For a given material composition, the stress in the concrete deck depends upon the stiffness of the girders and the fixity conditions of the girders and the deck. Design practices which ensure that the thermal movements of the girders and the concrete deck slab are in phase throughout the length of the

51

bridge would help minimize thermal-stress in concrete. Construction practices which would reduce total increase in temperature, and the rate of temperature decrease of concrete, relative to the top flange in the initial 48 hours after casting would decrease the early-age stress in concrete due to thermal movement. The temperature rise in concrete can be minimized if the temperature rise by hydration is out-of-phase with the daily temperature variation. This can be achieved by casting in the late afternoon or early evening as suggested by Wojcik et al. (2003). The level of shrinkage can be minimized through a control of material mixture design, use of admixtures and good curing practices. The analysis presented here is based on observations from a single-span, simply supported bridge with no skew. Generalized recommendations applicable to other cases require additional research.

3.9 Conclusions and Findings

From the analysis of data, the following conclusions can be drawn:

1. Thermal effects are important in the first 48 hours after casting. There is a rapid increase in the temperature followed by a period of cooling when the temperature of the concrete deck approaches the ambient temperature. Further variations in measured temperatures correspond well with the changes in ambient conditions.

2. Initially after casting, the expansion strain of concrete corresponds well with the free expansion of the steel reinforcement produced by the increase in temperature. Limited strain compatibility between concrete and the top flange is established by the end of the thermal heating produced by hydration. There is however a relative movement between the concrete deck and the top flange during the cooling period following initial heating. The concrete contracts more than the top flange of steel.

3. Full strain compatibility is achieved between steel and concrete when concrete cools to ambient temperature following an initial heating produced by hydration. Following the cooling period, measured strains in both the girder and the deck correspond well with the ambient temperature changes.

4. The restraint conditions do not effect thermal contraction of the bridge deck the same way as shrinkage (both autogenous and drying). Temperature changes in the girders closely follow those in the deck. Measured strains indicate significant thermal contractions and expansions of the girders which coincide with the ambient temperature changes. Therefore, the restraint to thermal contraction/expansion of concrete is significantly smaller than the restraint to shrinkage, which occurs immediately after setting and continues to increase monotonically with time.

5. Strains measured from the instrumented bridge primarily reflect the temperature movements of the deck and the girder and do not provide an indication of the stress in concrete. Assessment of the stress in concrete requires full structural analysis, which considers a continuous change in the material properties of concrete with time**.**

Section 4 Phase III Investigation
(Influence of Local Materials

4.1 Introduction

Available data suggests that the cracking in HP concrete possibly occurs at an early age, before it is open to traffic. This indicates the cause of cracking in such cases is related to the restrained volumetric contraction of concrete. Further, since the mixture proportion of HP concrete are standardized, the apparent lack of any relation between the observed cracking in HP bridge decks and variables such as the type, span length, or support condition, suggests that the local materials play a significant role in determining the performance of concrete in bridge decks. The role of local materials in determining the extent of free volumetric contraction of concrete and the development of strength therefore, needs to be evaluated. Guideline for proper selection of materials to minimize the potential for cracking in HP concrete decks can then be developed.

In this study local materials from different bridge decks were used in a laboratory test program to evaluate the shrinkage and the potential for restrained shrinkage cracking. Three bridge deck sites were selected for evaluation, one each in Regions 1, 3, and 9, of NYSDOT. Bridge decks were identified after reviewing the statewide Capital Program. This task was performed after meeting with the NYSDOT Bridge Deck Task Force and the Technical Working Group (TWG). Criteria similar to those specified in Subtask 1a for Phase I were used to select candidate bridge decks. Single span bridges with concrete deck and steel girders were selected. Material from each bridge deck site was supplied to the researchers by NYSDOT. The laboratory evaluation for obtaining the relevant material properties of concrete was conducted. Description of the materials used in the test program, specimen details, test procedures and the results of the test program are described in the subsequent sections.

New York State has a variety of geological regions and each of the NYSDOT's regions includes parts of one or more of these regions. The policy of NYSDOT has been to use local aggregates in production of concrete and asphalt wherever possible. As a result, even in the same NYSDOT Region, different concrete producers may use widely varying aggregates. Although throughout this report, the materials for each of these bridges have been identified by the Region in which they are located, the mixes tested should in no means be considered indicative of all concrete produced for bridge decks in the NYSDOT Region.

4.2 Scope of Work

The local materials which were used in three newly constructed bridges located in three different regions in the State of New York were evaluated in this study. Results of the experimental evaluation of HP concrete are presented. Specifically, the following were evaluated: (a) the development of the material properties with age especially elastic modulus and compressive strength; (b) unrestrained autogenous and drying shrinkage; and (c) the potential for cracking when the free shrinkage is restrained. Materials used in one newly constructed bridge deck in each region were sent to the material laboratory of Civil Engineering department at City College of New York. An experimental program was

conducted to evaluate the HP concrete mixtures and to determine the role of the local materials on the observed material behavior.

4.3 Specific Objectives

The specific objectives of the work reported here are:
1. To determine the development of material properties of HP concrete from different Regions of New York State.
2. To assess the influence of local materials on the development of material properties and free shrinkage of concrete.
3. To assess the influence of local materials on the potential for restrained shrinkage cracking of concrete.

4.4 Material Description

A detailed description of the materials used in the HP concrete in Regions 1, 3 and 9 is provided in this section. Mixture designs utilized in constructing the bridge decks are tabulated in Tables 11 to 13, for Region 1, 3 and 9 respectively.

Table 11: Concrete Mixture Design for Region 1

Material	Saturated Surface Dry Weight (Kg.)	Solid Volume (m^3)
Water	162	0.162
Cement	300	0.095
GGBFS	81	0.028
Silica Fume	24	0.011
Air		0.065
Fine Aggregate	656	0.252
Coarse Aggregate #1	520	0.193
Coarse Aggregate #2	520	0.193
	2263.000	1.00

Table 12: Concrete Mixture Design for Region 3

Material	Saturated Surface Dry Weight (Kg.)	Solid Volume (m^3)
Water	162	0.162
Cement	300	0.095
Fly Ash	80	0.034
Silica Fume	25	0.011
Air		0.065
Fine Aggregate	657	0.248
Coarse Aggregate #1	419	0.156
Coarse Aggregate #2	628	0.229
	2271.00	1.00

Table 13: Concrete Mixture Design for Region 9

Material	Saturated Surface Dry Weight (Kg.)	Solid Volume (m³)
Water	162	0.162
Cement + Silica Fume (blended cement)	325	0.103
Fly Ash	80	0.034
Air		0.065
Fine Aggregate	655	0.248
Coarse Aggregate #1	510	0.194
Coarse Aggregate #2	510	0.194
	2242.00	1.00

Portland Cement

Type II cement was used in Region 1. Region 3 used Type I/II cement. Cement blended with silica fume was used in Region 9. Table 14 summarizes the cement brand and the type used by each Region.

Table 14: Cement brand & type used by each region

Regions	Region#1	Region#3	Region#9
Cement	Cement Brand: Lehigh Type II, Low Alkali	Cement Brand: Essroc Type I/II	Cement Brand: Lafarge Whitehall Type SF (blended sfilica fume)

Fly Ash and Ground granulated blast-furnace slag

In Regions 3 and 9, 20% of weight of cement was replaced with Class F-fly ash while in Region 1, 20% of weight of cement was replaced with ground granulated blast-furnace slag (GGBFS). In Region 9, fly ash was supplied by ISG Resources Lansing. Information regarding fly ash used in Region 3 and the GGBFS used in Region 1 were not available.

Microsilica – Silica Fume

Densified Silica fume replaced 6% of the weight of cement in Regions 1 and 3 while in Region 9, cement blended with silica fume (Type SF cement supplied by Lafarge) was used. Source (brand) and composition of silica fume used in Regions 1 and 3 were not available. All silica fume, however, comes from the same source with same characteristics.

Fine Aggregate

Fine aggregate used in Regions 1, 3 and 9 were obtained from local quarries and comprised of natural sand. Table 15 shows the specific gravity and fineness modulus of sands used in each region.

Table 15: Specific gravity and fineness modulus (FM) of fine aggregates

	Specific gravity	Fineness Modulus (FM)
Region#1	2.60	2.75
Region#3	2.65	NA
Region#9	2.70	2.70

Coarse Aggregate

Locally available coarse aggregate was used in each region. Coarse aggregates from Regions 3 and 9 were gravel while the Region 1 coarse aggregates were crushed stone. Table 16 shows the specific gravity and type of coarse aggregates used in each region. Figure 38 shows the coarse aggregate #1 and 2 used in each region.

Table 16: Specific gravity & type of coarse aggregates used in each region

	Region#1	Region#3	Region#9
Coarse Aggregate #1	Type:Crushed Stone Specific Gravity=2.69	Type:Gravel Specific Gravity=2.72	Type:Gravel Specific Gravity=2.63
Coarse Aggregate #2	Type:Crushed Stone Specific Gravity= Not given	Type:Gravel Specific Gravity=2.72	Info not given

Figure 38: Coarse aggregate #1 and #2 used in the different regions.

Chemical Admixtures

Three different chemical admixtures were used in the Class HP concrete mixtures.

Air Entraining Admixture

Table 17 lists the brand of air entraining agent used in each region. The prescribed dosage as a percentage of weight of cement was 0.188% for region 1 and 3 and 0.216% for region 9.

Table 17: Brand of air entraining agent used in each region

	Region#1	Region#3	Region#9
Air Entraining Agent	Master Builders(BASF) MB-VR	GRACE Chemical Darex II AEA	Master Builders(BASF) MB-VR

Retarder

Table 18 lists the brand of retarder agent used in each region. The prescribed dosage as a percentage of weight of cement was 0.313% for region 1 and 3 and 0.314% for region 9.

Table 18: Brand of retarder used in each region

	Region#1	Region#3	Region#9
Retarder	Master Builders(BASF) Pozzolith 100-XR	GRACE Chemical Daratard 17	Master Builders(BASF) Pozzolith 100-XR

Water reducer (WR)

In all Regions, ADVA R 100 water reducer produced by Grace Construction Products was used. The dosage of water reducer was adjusted to achieve a slump in the range 75-125 mm (3 - 5 inches).

4.5 Specimen Preparation and Testing

Different specimens were used for determining different aspects of material behavior. All the specimens were cast following the same procedure and cured under identical conditions. Specimen preparation comprised of the mixing followed by placing and finishing operations. Details of specimen preparation procedure and number and type of specimens used in this study are described below.

4.5.1 Mixing Procedure

The mixing procedure followed the specification and provisions given in ASTM C192 (1994). Materials were measured separately with a precision of $\pm$ 0.01 kilograms ($\pm$ 0.02 lbs), except for chemical admixtures where precision of $\pm$ 0.1 grams was used. It should be noted that all the admixtures after measurement were premixed with water before the mechanical mixing. Following ASTM C192 (1994), the drum mixer was damped and drained before mixing the concrete. The slump test was carried out following the specification given in ASTM C143 (1994) and the dosage of HRWR was adjusted to achieve the desired slump. After mixing, concrete was poured in a tray and manually mixed using a shovel to avoid segregation.

4.5.2 Placing and Finishing Operations

After mixing, the fresh concrete was taken into an environmental chamber, where temperature and relative humidity were kept constant at 30°C (86°F) and 40%, respectively. The specimens were cast inside the environmental chamber. Following ASTM C192 (1994), fresh concrete was placed in the forms in 3 layers. Each layer was approximately one third the volume of the form. Each layer of concrete was tamped twenty five times with a steel rod. After filling the form, the specimens were vibrated on a vibration table for ten seconds. The excess concrete was removed by troweling off the top surface flush with top of the form.

4.5.3 Curing/Drying Conditions

After finishing operations, all specimens were covered with plastic sheets. Specimens were demolded 24 hours after casting. and cured in the environmental chamber where relative humidity and temperature was kept constant; temperature and relative humidity during the curing for all specimens were set to 30°C (86°F) and 40%, respectively.

4.5.4 Measurement of Mechanical Properties

All material properties were determined at 1, 3, 7, 14 and 28 days of age. Three specimens shall be tested at each age. Details of the test program describing the test procedures for obtaining the mechanical properties are given below.

4.5.4.1 Elastic Modulus and Compressive strength

Compressive testing was performed using a closed-loop test machine to determine the elastic modulus and the compressive strength of concrete. Before testing, the ends of the specimens were prepared using a sulfur-capping compound to ensure uniform contact with the loading platen of the test machine. The elastic modulus was determined using a standard 100 mm x 200 mm (4 in x 8 in) cylinder with a surface mounted compressometer following the procedure given in ASTM C-469 (1994). The compressive strength was determined by applying load up to failure at a constant rate as specified in ASTM C-39 (1994).

4.5.4.2 Tensile Strength

The tensile strength was determined using the split cylinder tests performed on standard 100 mm x 200 mm (4 in x 8 in) cylindrical specimens as per the provisions of ASTM C 496 (1994).

4.5.5 Shrinkage Measurements

In the test program both free and restrained shrinkage tests were performed. Free shrinkage measurements comprised of determining volume changes in concrete when no external constraint is imposed on its movement. Ring specimens were used to evaluate the performance of concrete under restrained conditions. Further information regarding the test procedures are given below.

4.5.5.1 Free Shrinkage

Free shrinkage measurement were performed using prismatic and ring specimens. Autogenous and drying shrinkage was measured using the prismatic specimens. The ring specimens, which are primarily companion specimens for the restrained ring specimens, were used to obtain free shrinkage from concrete subjected to similar conditions as those encountered in the restrained ring specimens.

4.5.5.2 Free Shrinkage – Prismatic Specimens

Concrete was cast inside the environmental chamber into four prismatic forms made of plexiglass with dimensions given as, width: height: length = 75 mm (3 in): 75 mm (3 in): 300 mm (12 in). The forms were lined with Teflon sheets to reduce friction between the

concrete and the wall of the forms. After placing and finishing operations, the members were covered with plastic sheets to prevent moisture loss. 8 hours after casting, linear variable differential transformers (LVDTs) were attached to both ends of each specimen to measure the axial deformation of the specimen associated with shrinkage and/or thermal expansion of concrete. The LVDTs were reacted off of elevator bolts, which were embedded into the concrete at the time of casting. The elevator bolts had a head diameter equal to one inch and provided a larger area of contact with concrete in order to minimize any relative movement of the bolt inside the concrete. During casting, the elevator blots were firmly attached to the walls of the form using two nuts placed on either side of the form. The distance between the bolts was measured using a caliper, before casting and was taken as the initial gauge length for calculating axial strain in the specimens due to free shrinkage or thermal expansion. The nuts holding the elevator blots outside the form were removed before attaching the LVDTs. The bolt securing the individual pieces of the formwork were also removed to allow free movement of concrete, before initiating readings from the LVDTs. Data from the LVDTs were collected at regular intervals of time up to demolding.

The specimens were demolded 1 day after casting. During demolding, the LVDTs were detached from the specimen and the data acquisition program was stopped. Two specimens were completely wrapped with Aluminum tape to prevent any moisture loss; the purpose of these two sealed specimens was to measure the autogenous shrinkage. The remaining two specimens were left to dry from all sides for total shrinkage measurements. The LVDTs were attached to the two ends of each prismatic member after demolding and the data acquisition was restarted. Data was continuously acquired at 1 minute intervals up to a minimum of 28 days. The schematic figure and photographs of the test setup used for shrinkage measurements from prismatic members, before and after demolding are shown in Figures 39 and 40.
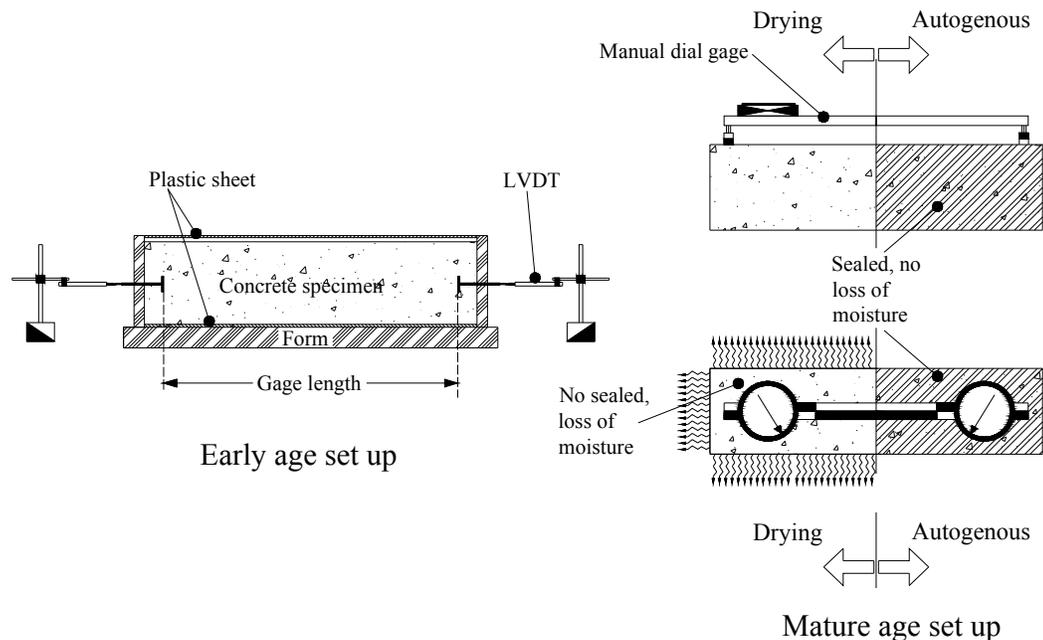
Figure 39: Setups for measurements of linear free shrinkage from prismatic specimens

Figure 40: Experimental Setups for free shrinkage measurements from Prismatic specimens

4.5.5.3 Free Shrinkage – Ring Specimens

The ring specimens for free shrinkage measurements were cast using two concentrically placed cylindrical molds. The inner and outer molds were placed on a wooden base, which was covered with plastic sheet. The outer form was made of plastic and had a diameter equal to 450 mm(18 in) and the inner form was made of cardboard with a 300 mm (12 in) diameter. The surfaces of the molds in contact with concrete were covered with plastic to prevent loss of moisture and to provide a smooth surface finish. Two holes were made on diametrically opposite sides of the inner cardboard form for placing elevator bolts. The elevator bolts were secured to the cardboard form during casting. Concrete was cast inside the environmental chamber and the specimens were covered with a plastic sheet to prevent any loss of moisture. After initial setting of concrete, the nuts securing the elevator bolts to the cardboard form were removed and LVDTs were reacted off of the free end of the bolts. LVDTs were positioned in the center of the molds and attached to each specimen to measure change in the diameter produced by shrinkage or expansion of concrete. The distance between the heads of the elevator bolts embedded in concrete was measured using calipers before casting and was used as the gauge length for determining the radial strain in the specimens. Data from the LVDTs was collected continuously at 5 minute intervals up to demolding.

The data collection was stopped during demolding. The inner and outer curved surfaces of the rings were wrapped with aluminum tape while the top and bottom surfaces were left to dry. The LVDTs were reattached to the concrete rings and data was recorded at 5 minute intervals up to a minimum of 28 days. Setups for shrinkage measurements of ring specimens, before and after demolding are shown in Figures 41 and 42.

Figure 41: Experimental Setup for free shrinkage measurements from unrestrained ring specimens
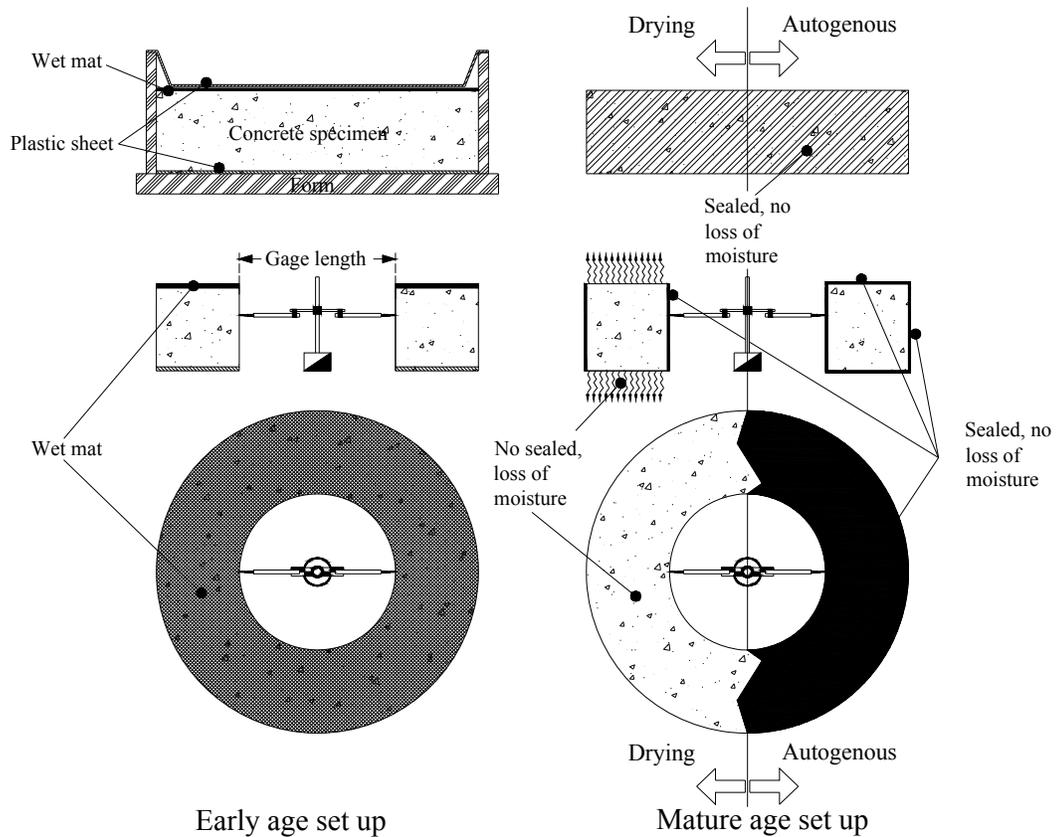
Figure 42: Setups for measurement of radial strain in unrestrained ring specimens

4.5.5.4 Restrained Shrinkage Measurements

Ring specimens which comprised of a concrete ring cast around a steel ring were used to assess the potential for cracking under restrained shrinkage and to measure the development of stress in concrete due to restraint to volumetric contraction resulting from shrinkage. The nominal dimensions of the inner radius, the outer radius and the height of concrete in the ring

specimens were equal to 152.4 mm (6 in), 228.6 mm (9 in) and 76.2 mm (3 in), respectively. Steel rings with two different thicknesses equal to 12 mm (½ in) and 18 mm (3/4 in) were used in this study to achieve different levels of restraint. Four samples were cast for each region; two for each steel thickness. Each steel ring was equipped with two strain gages mounted in the tangential direction. Strain gages were attached to the interior face of the steel ring. The gages were positioned one inch from the top and bottom of the ring along the same generatrix, as shown in Figure 43.

The mold for restrained shrinkage consisted of a wooden base covered with plastic sheet, an outer form made of plastic with diameter of 18 inches and an inner ring made of steel with a 12 in diameter. The inside surface of the outer form was covered with a plastic sheet. The casting and finishing operations for the ring specimens were performed inside the environmental chamber, which was maintained at 30°C (86°F) and 40% relative humidity (RH). The steel rings were placed inside the chamber for one day before casting to allow the rings to reach thermal equilibrium prior to placing the concrete. The specimens were covered with plastic sheets immediately after casting. The data acquisition from the strain gages was initiated immediately after completing the casting operation. In addition, thermocouples were attached to the steel rings to record temperature changes. After 1 day, the specimens were demolded and the outside surface of the concrete was covered with an aluminum tape. The concrete was allowed to dry from the top and bottom surfaces. Data from the strain gages was collected up to a minimum of 28 days of age or cracking in the concrete, whichever occurred earlier. Setups for shrinkage measurements of ring specimens, before and after demolding are shown in Figures 43 and 44.
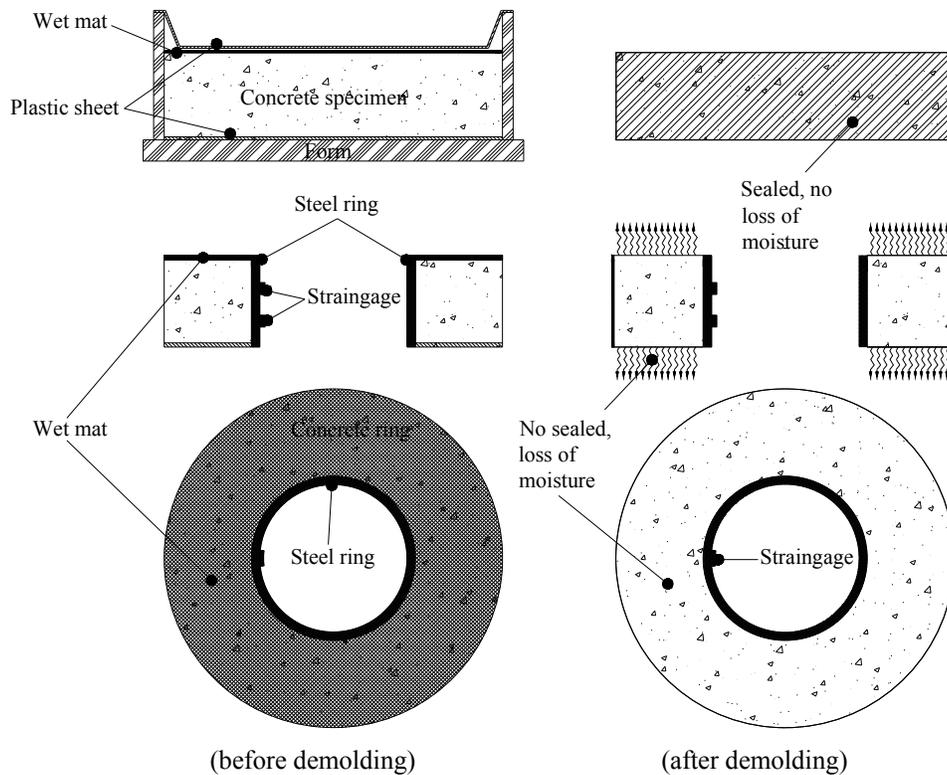
Figure 43: Setup for restrained shrinkage measurements using the ring specimens.

Figure 44: Photographs of experimental setup for restrained shrinkage measurements using ring specimens

4.6 Development of Mechanical Properties with Age

The results of the experimental test program to determine the development of strength and elastic mechanical properties of HP concrete using local materials from Regions 1, 3 and 9, are summarized in this section.

4.6.1 Compressive strength Development

The compressive strength gain for the three regions is shown in Figure 45. It can be seen that rate of compressive strength development for all regions was rapid up to seven days following which the rate of compressive strength gain decreased, eventually reaching an asymptotic value at approximately fourteen days of age. The 28-day compressive strengths for Regions 1, 3 and 9 were 41.2, 38.5 and 44.3 MPa (5.97, 5.58 and 6.43 ksi), respectively. The values of compressive strength from Regions 1 and 9 were comparable up to 7 days of age. At any age, the compressive strength for Region 3 was noticeably smaller when compared to the corresponding values from Regions 1 and 9. The rate of strength gain in Region 3 was also lower than the corresponding rate of strength gain in Regions 1 and 9. Concrete from all three regions achieved minimum compressive strengths equal to 20.7 and 34.5 MPa (3.0 and 5.0 ksi) by 2 and 7 days of age.
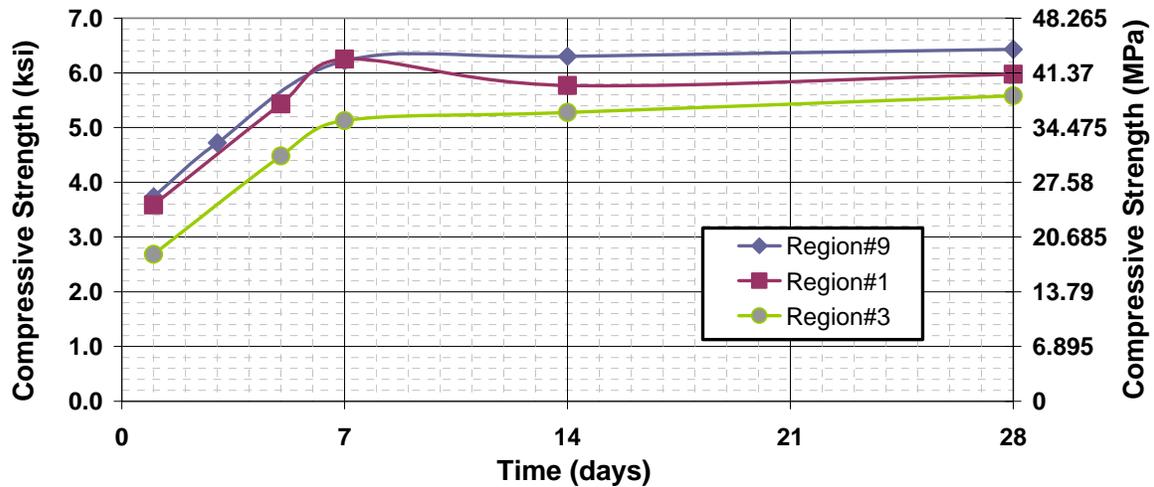
Figure 45: Development of compressive strength with age

4.6.2 Elastic modulus development

The increase in the static elastic modulus of concrete for Regions 1, 3 and 9 as a function of age after casting are plotted in Figure 46.a. The increase in static modulus after 1 day is shown in Figure 46.b for clarity. The trends in the modulus increase appear similar to those obtained from compressive strength. However, unlike strength gain, the elastic modulus increases most rapidly in the first day, following which there is noticeable decrease in the rate of change. The modulus appears to remain relatively constant after 7 days of age. Also, unlike the relative trends in strength development, the elastic modulus obtained from Region 1 is higher than the corresponding values from Regions 3 and 9. In the first 24 hours, Region 9 exhibits the fastest increase in elastic modulus. While initially after setting the elastic modulus from Region 9 is lower than the corresponding value from Region 3, the values

obtained from Region 9 after 1 day are higher than the corresponding values from Region 3. After 24 hours, Region 9 exhibits the fastest rate of increase in elastic modulus of all regions. The rates of increase in elastic modulus for Regions 1 and 3 are comparable after 1 day.
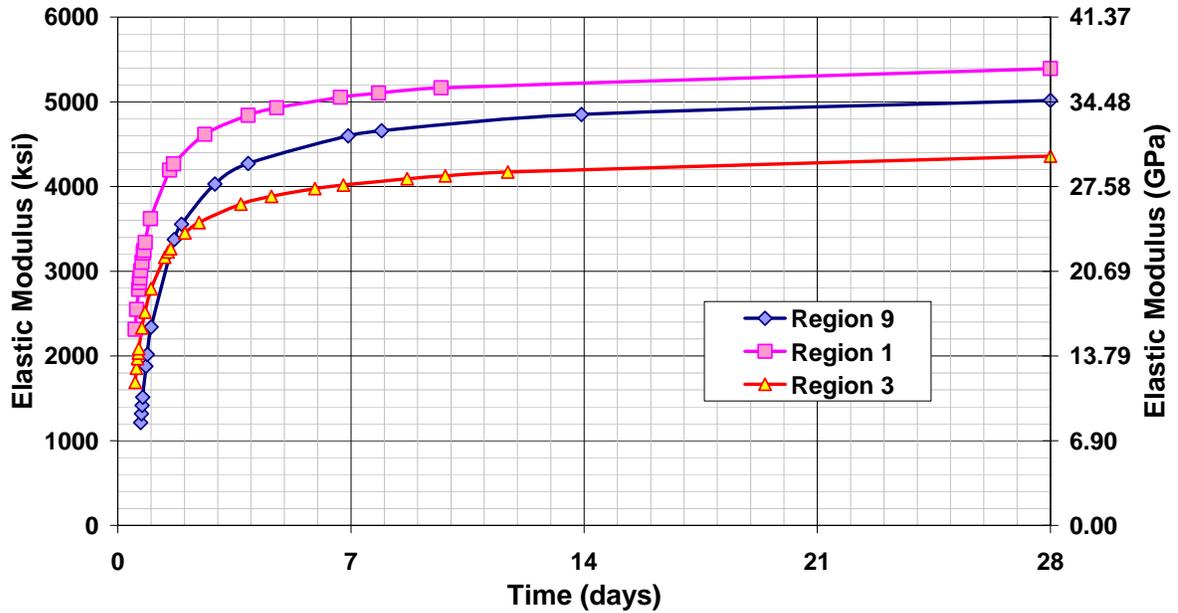
Figure 46.a: Development of Elastic Modulus with age
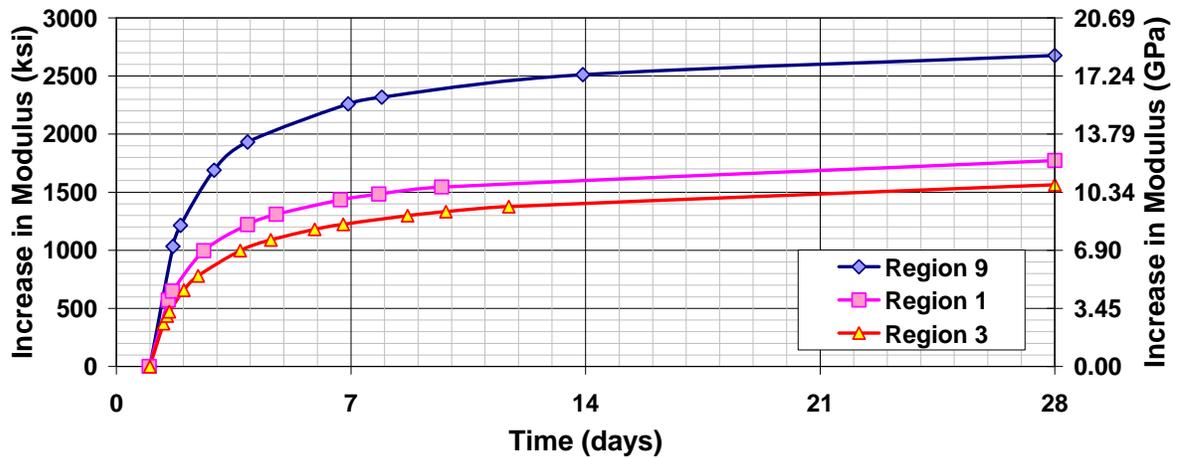
Figure 46.b: Increase in Elastic Modulus after one day.

4.6.3 Split cylinder tensile strength development

The change in split tensile strength of concrete for Regions 1, 3 and 9 as a function of age after casting are plotted in Figure 47. The trends in the tensile strength are similar to those obtained for compressive strength. There was a very rapid increase in tensile strength up to 7 days, following which the rate of strength gain decreased, approaching an asymptotic value at 14 days. It can be seen that the values of tensile strength form Regions 3 and 9 were

comparable in the first three days, following which the tensile strength from Region 9 were higher than the corresponding values from Region 3. The final values of tensile strength from Regions 1 and 3 were comparable. It should be noted that consistent with the relative trends of compressive strength with age, Region 3 had the lowest tensile strength and rate of increase at any given age, while Region 9 had the highest tensile strength and rate of strength gain.
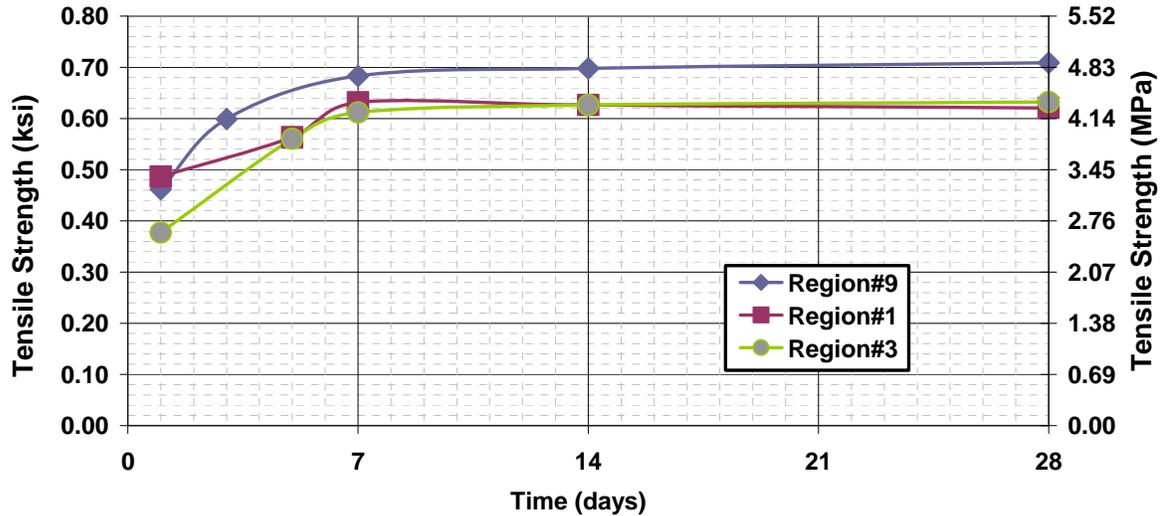
Figure 47: Development of split cylinder tensile strength

4.6.4 Discussion of Mechanical Test Results

The differences in the values of strength and elastic material properties of concrete for Regions 1, 3 and 9 obtained using identical specimens, which were cured under similar conditions are related to differences in the local materials. Few key differences in the materials are listed below.

1. The coarse aggregate in Regions 3 and 9 were gravel, while the coarse aggregate in Region 1 was crushed stone.
2. Region 9 used cement with blended silica fume while in Regions 1 and 3, silica fume was added to the mix separately.
3. Fly ash was used in Regions 3 and 9 while in Region 1, GGBFS was used.

The differences in the observed change in material properties of concrete for the different Regions can be rationalized considering concrete as a composite material comprising of aggregate and cementitious matrix. For a given concrete mixture composition the following can be stated:

1. At any age, the material property of the concrete composite (strength or elastic modulus) depends upon the properties of both the aggregate and the cementitious matrix;
2. Elastic modulus of the concrete composite depends upon the elastic interaction between the individual components and can be adequately predicted using the rule of mixtures.

66

3. The strength of the composite material depends upon the strength of the individual components and the strength of the interface bond between the aggregate and the matrix. The strength of the composite is therefore controlled by the strength of the weakest element in the composite.

4. The increase in material property with age is primarily controlled by the cementitious matrix. In the case of elastic modulus, an increase in the elastic modulus of the cementitious matrix can be directly related to changes in the elastic modulus of the concrete composite. The compressive strength however may not scale linearly with an increase in the strength of cementitious matrix because of the following reasons:

   a. Failure process is an inherently non-linear process, which does not scale linearly with the strengths of the components; and

   b. There may be changes in the mode of failure with an increase in the strength of the matrix. The predominant mode of failure may change from cracking along the interface to fracturing of aggregate.

4.6.4.1 Strength Gain with Age

Concrete with crushed aggregate has been shown to provide a higher compressive strength than gravel coarse aggregate. Crushed rock creates a much better bond between the paste and the aggregate than gravel. The smooth texture of the surface in gravel aggregate decreases the bond strength, which influences the strength [ACI-363 1992; Mehta and Aictin 1990]. The compressive strengths from Region 1, which contained crushed stone were however comparable to Region 9 with gravel aggregate. The crushed aggregate in Region 1 appeared to be angular and with larger aspect ratios, which would result in lower strength. Besides these differences in the local aggregate, other possible reasons for differences in the compressive and tensile strengths obtained from the different regions could be attributed to the differences in the form and composition of the cementitious material in each mix. The differences in the reactivity of blended silica fume and the silica fume added separately and between fly ash and GGBFS might contribute to differences in the rate of strength gain exhibited by the HP concrete mixtures from the three regions.

From the test results, a slight decrease in the strength (both compressive and tensile) was observed in Region 1. This loss in compressive strength of air-cured concrete is also referred to in the literature as "strength retrogression". Since GGBFS was used in Region 1 while, the other two regions used fly ash, the experimental evidence suggests that the combination of cement and GGBFS is more sensitive to strength retrogression. In some cases it has been shown that the observed strength retrogression was due to the drying of a very thin layer of the skin of the HPC. This drying resulted in a significant tensile stress gradient, sufficient to affect the compressive strength values [De Larrad and Aictin 1993]. Another reason that could be put forward in explaining strength retrogression would be the degree of desiccation due to drying, which influences the progress of hydration.

The failure surfaces of concrete specimens from the split tension tests for Regions 1, 3 and 9 are shown in Figures 48, 49 and 50, respectively. The differences in the shapes and type of aggregate are immediately obvious from the failure surfaces. Visual examination revealed that while at 1 day the fracture surface passed around the aggregate, by five days, cracking was predominantly through the aggregate. Inspection of the failure plane of Region 3 showed that some of the coarser aggregates, larger than 31.75 mm (1.25 in), were not

cracked even at later ages. This suggests a decreased bond between the aggregate and the matrix, which may potentially explain the lower values of strength obtained for this region.
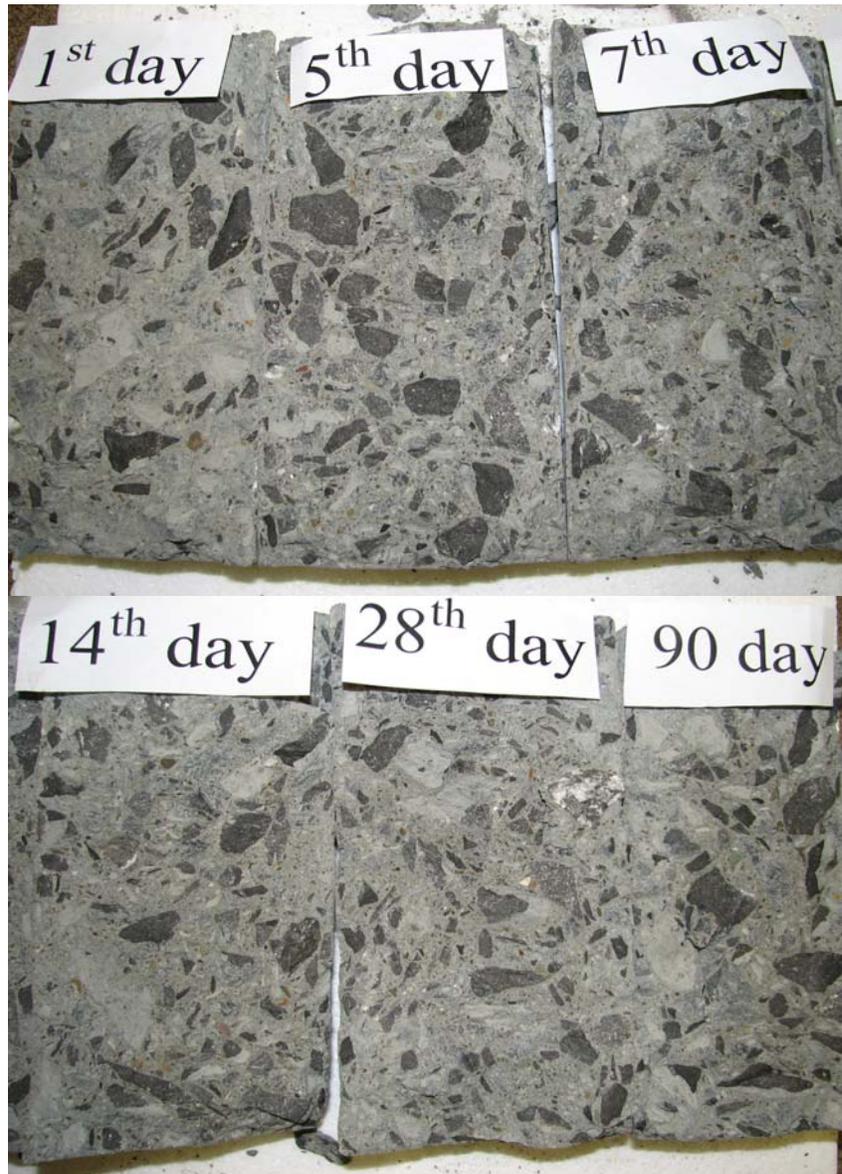
Figure 48: Failure surface of Region 1 specimens at various ages under split cylinder test
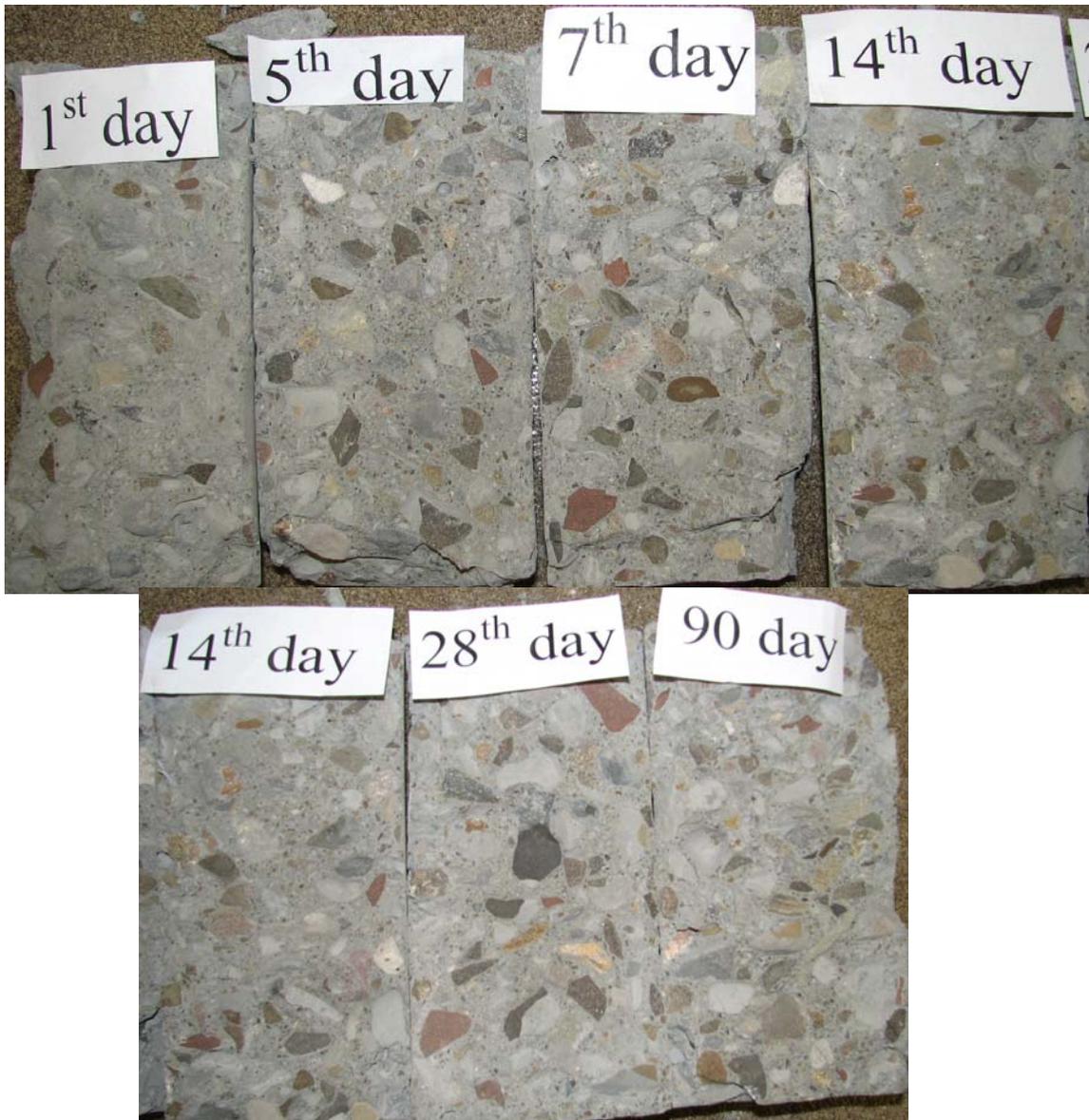
Figure 49: Failure surface of Region 3 specimens at various ages under split cylinder test
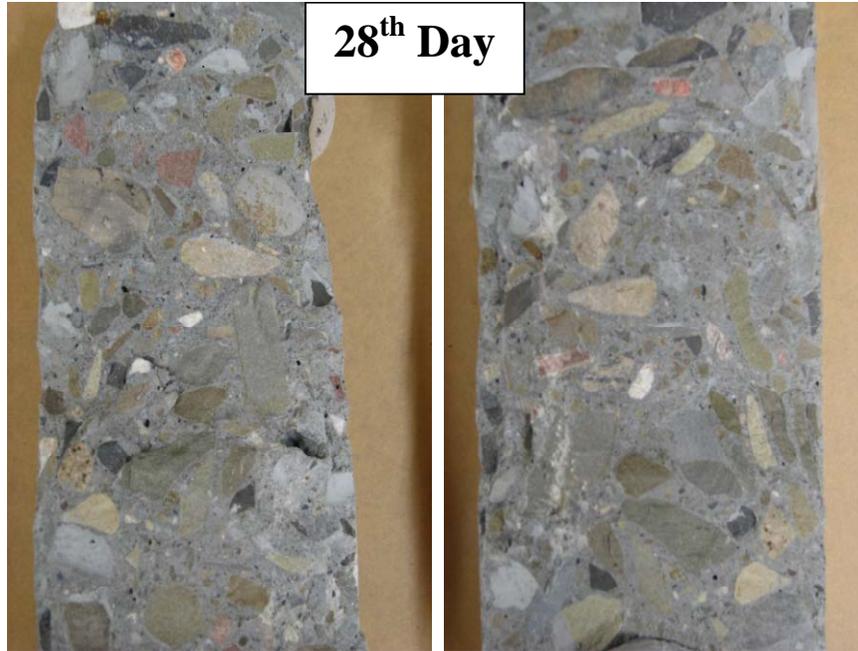
Figure 50: Failure surface of Region 9 specimens at 28th day under split cylinder test

Figure 51 shows the relationship between the ratio of split tensile strength to compressive strength and the compressive strength of concrete. It has previously been reported that as the compressive strength increases the ratio of tensile and compressive strengths decrease [Mehta and Aictin 1992, Arioglu et al. 2006] which also has been the general trend in the Regions.
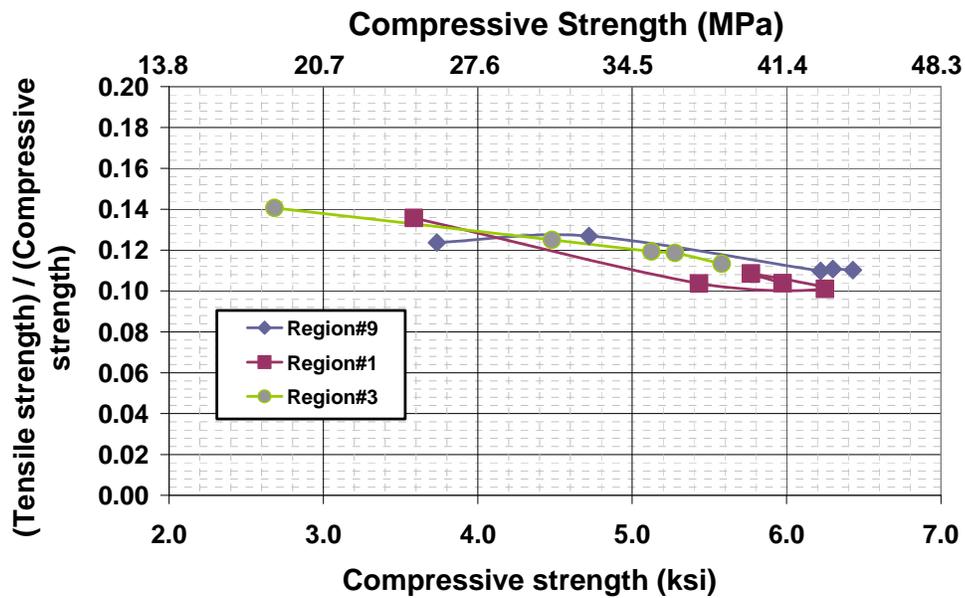
Figure 51: Variation of the relationship between tensile and compressive strength with compressive strength of the Regions

4.6.4.2 Increase in Elastic modulus with Age

For a given aggregate, increase in compressive strength of concrete is achieved by improving the mortar to achieve higher strength and mortar-aggregate bond. Increased performance of the mortar matrix also results in an increase in the elastic modulus of the composite concrete material [Myers 1999]. The results obtained in this study, however, are not in agreement with this observation, especially considering Regions 1 and 9. At any age, the regions could be arranged in descending order of elastic modulus as Region 1>Region 9>Region 3. The compressive strengths from Regions 1 and 9 were comparable (up to 7 days) and higher than the corresponding values from Region 3. Differences in aggregate and the cementitious materials in each Region may potentially explain the observed trend. The importance of coarse aggregate quality on elastic properties of HPC has been pointed out by Aitcin and Mehta (1992). Although information regarding the mechanical properties of the aggregates used in the Regions were not available, there is a possibility that the coarse aggregate in Region 1 (Type of rock: limestone) were stiffer. Too stiff an aggregate, though improving modulus, may cause stress concentration and initiate more micro cracking causing a decrease in strength [Zhou et al. 1995].

Regions 3 and 9 provide a basis of comparing the performance of silica fume added to the mix and silica fume blended with cement. In both Regions gravel aggregate were used and therefore the observed differences can be attributed to the form of silica fume used in the mix. The more rapid increase in both the strength and elastic modulus from Region 9 when compared to Region 3 suggests that blended silica fume is more reactive when compared with silica fume added separately.

The elastic modulus from Region 9 increases more rapidly than the observed rate of change in Regions 3 and 1. This suggests that the combination of GGBFS and silica fume is more reactive than the combination of fly ash and silica fume. The lower absolute value of elastic modulus from Region 9 when compared to Region 1 could be attributed to the difference in the aggregate used in the two regions.

4.6.5 Findings from Mechanical Tests

Based on the results presented here, the following conclusions can be drawn:

1. The results of compressive strength and elastic modulus of concrete indicate the importance of considering the local material properties. Differences in aggregate and cementitious material contribute to significant differences in values of compressive and tensile strengths, and the rates of increase in strength and modulus. Specifically,

   a. Crushed stone used for coarse aggregate resulted in the highest value of elastic modulus (from Region 1). However, these aggregate did not produce any differences in the compressive strength when compared with gravel aggregate (comparing Regions 1 and 9).

   b. Use of silica fume blended cement resulted in a significantly higher rate increase in the rate of strength and modulus gain with age when compared to silica fume added separately to the mix (comparing Regions 9 and 3, which have gravel coarse aggregate and fly ash as cement replacement)

   c. GGBFS is more reactive than fly ash resulting in a more rapid increase in modulus and strength.

d. Considering the relative increases in elastic moduli, blended silica fume provides the highest reactivity.

2. The general trend in the relationship between compressive strength and elastic modulus appear to be similar for concrete from all three regions. There is a decrease in the ratio of tensile to compressive strength with age.

3. Compressive strength from all three regions reaches a constant value by 14 days of age. The most rapid increase in compressive strength occurs within 7 days of age. In Regions 1 and 9, a minimum compressive strength of 20.7 MPa (3000 psi) was attained by one day while for Region 3 the 20.7 MPa (3000 psi) was attained between 1 and 2 days.

4. The elastic modulus from all three regions appeared to reach a constant value by 7 days. The most rapid increase in elastic modulus occurs up to 3 days of age.

4.7 Free and Restrained Shrinkage Measurements

Results from free and restrained shrinkage measurements for Regions 1, 3 and 9 are presented in this section. Both autogenous and drying shrinkage were continuously measured from 8 hours after mixing. Restrained ring tests were performed to evaluate the potential for restrained shrinkage cracking. The level of restraint to the concrete was varied using steel rings of different thicknesses. The steel rings were instrumented with strain gages to assess the evolution of stress in concrete due to the elastic restraint to free shrinkage. Specimens used in this study for free and restrained shrinkage measurements were stored in an environmental chamber, which was maintained at 30°C and 40% RH. The data from the different measurements are presented and analyzed in the subsequent sections.

4.7.1 Free Shrinkage

Free shrinkage measurements were obtained using specimens in which were allowed unrestrained volume change produced by shrinkage and thermal strains. Axial strains, corresponding to the unrestrained volume change was obtained from the prismatic specimens. Change in length of the prismatic specimens which were kept in a sealed condition was used to determine the autogenous shrinkage. In specimens, which were left to dry from all sides, the moisture profile across the cross-section can be assumed to be symmetric. The drying in such specimens can be assumed to be uniform at a given depth from the surface. Change in length obtained from such specimens could be attributed to loss of moisture resulting from a combination of autogenous and drying shrinkage.

The unrestrained ring specimens had identical dimensions of concrete as the corresponding dimension of concrete used in restrained ring specimens. After demolding, the boundary conditions of temperature and humidity for the unrestrained rings were also identical to the restrained rings; both were allowed to dry from the top and bottom surfaces while the curved inner and outer surfaces prevented any movement of moisture. The cross-sectional dimensions of the ring were identical to the cross-sectional dimensions of the prismatic specimen. However, since the ring specimen were only permitted to dry from the top and bottom surfaces, the resulting moisture profile would be different from the moisture profile in the prismatic specimen at a corresponding age. In the case of the ring, moisture

gradients would primarily exit in the vertical direction. The results from the unrestrained ring specimens cannot directly be compared to the results of the prismatic specimens. The radial strain resulting from a change in diameter in unrestrained ring specimens was therefore only used to provide a basis for evaluating the results of the restrained rings.

Equivalent shrinkage strain for both prismatic and ring specimens was computed from the measured deformation (diametric deformation for the rings and axial deformation for the prismatic specimens) using Equations 4 and 5.

$$\varepsilon_a = \frac{\Delta_a}{L_o} \tag{4}$$

$$\varepsilon_{rr} = \frac{\Delta_D}{D_o} \tag{5}$$

where, Δ_a and L_o are respectively the change in length and the initial length of the prismatic members, and Δ_D and D_o are respectively the change and the initial diametric lengths of the ring specimens.

The measured axial strain in prismatic specimens which were subjected to drying contains contributions from both autogenous and drying shrinkage and is referred to as *total shrinkage* (ε_{total}). The drying shrinkage (ε_{drying}) at any age was obtained by subtracting the autogenous shrinkage strain obtained from sealed specimens from ε_{total}.

$$\varepsilon_{drying} = \varepsilon_{total} - \varepsilon_{autogenous} \tag{6}$$

It is implicitly assumed that the autogenous and drying shrinkage are mutually independent and that drying of concrete does not influence the autogenous shrinkage.

4.7.1.1 Unrestrained Prismatic Specimens

The autogenous and total shrinkage strains as functions of age for Regions 1, 3 and 9 are shown in Figure 52. The shrinkage strains measured before demolding are shown separately in Figure 53 for clarity. Drying shrinkage obtained by subtracting the autogenous shrinkage from the total shrinkage is plotted in Figure 54 and listed in Table 19. The values listed in the table and used in the figures are the average of the measured strain from the two specimens.

Before demolding, since all specimens were prevented from drying, the measured volume change during this period could be attributed to autogenous shrinkage and thermal strains. It can be seen that there is significant volumetric shrinkage of concrete from all regions in the first day. There is however a significant difference in the volumetric strain for the three regions from an early age. Region 1 exhibits a significantly higher contraction up to 1 day when compared to the other two regions; Region 1 has the fastest increase and the largest magnitude of volume contraction in this period. The influence of expansion produced by the heat of hydration seems to be significant only in Region 9. In the first 24 hours, an initial expansion followed by contraction is observed in Region 9, while the other two Regions exhibit a continuous contraction. It should be noted that readings for length changes were initiated approximately eight hours after casting. In Regions 1 and 3, the temperature at the time of initiating readings was close to peak, following which it rapidly approached temperature of the chamber at 30°C. In Region 9, there is a slower rise in temperature and the maximum temperature during the temperature rise associated with the heat of hydration occurs after 8 hours resulting in a noticeable expansion.

After 1 day, the magnitudes of the total shrinkage for Regions 1 and 9 appear to be comparable at any age. While initially, the rate of total shrinkage from Region 3 is lower than the corresponding values from the other two regions, the values from all three regions are comparable at 3 days of age. After 3 days, Region 3 exhibits the highest total shrinkage when compared with the other two regions. The general trends from all three regions suggest a very rapid increase in total shrinkage immediately after subjecting the specimen to drying which last approximately 10 days, following which there is a decrease in the rate of strain. After 20 days, while there is a continued increase in total shrinkage, the trends in the measured strain suggest a steady linear increase with time.

After one day, Region 9 exhibits the most rapid increase in autogenous shrinkage. While there is a noticeable difference in the autogeneous shrinkage strains from Regions 1 and 9 at 1 day, the values from the two regions appear to be comparable after 20 days of age. Region 3 exhibits the slowest rate of increase in autogenous shrinkage and has the smallest magnitude of autogenous shrinkage strain at any age.

Trends in drying shrinkage, which is produced as a result of moisture loss due to evaporation, are very different from those observed in autogenous shrinkage. Region 3 exhibits the most rapid increase in drying shrinkage and has the largest value at any given age. While there is a high early rate of drying shrinkage observed in the first 3 days for Region 9, there is a noticeable decrease in the rate of drying shrinkage after 3 days. The drying shrinkage obtained from Regions 3 and 9 are comparable in the first 3 days. After 9 days of age, drying shrinkage strains from Regions 1 and 9 are comparable.
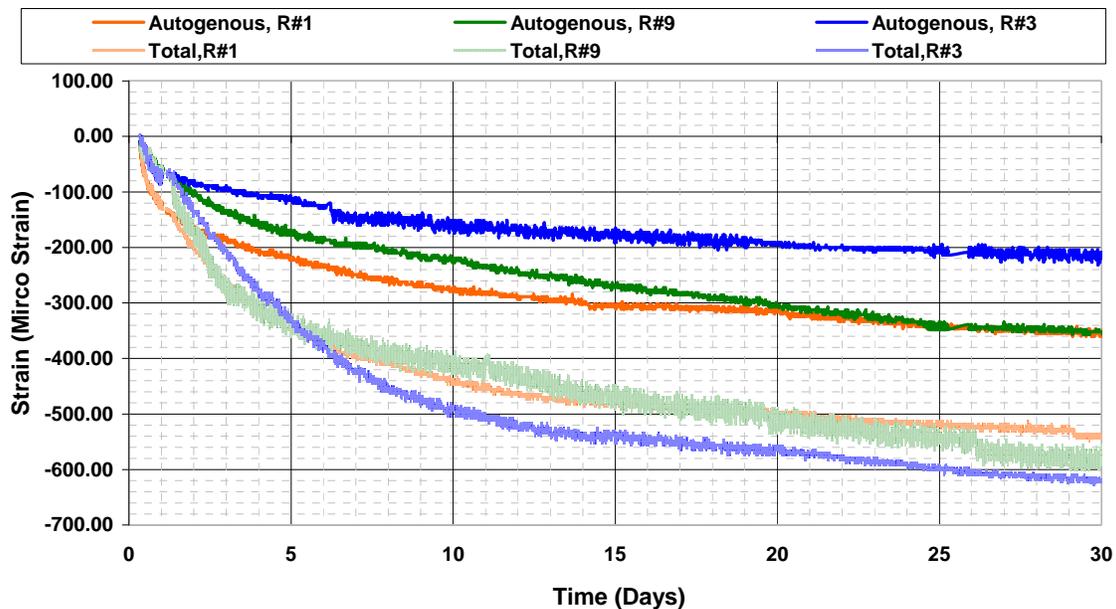
Figure 52: Total and Autogenous shrinkage strains for Regions 1,3 and 9
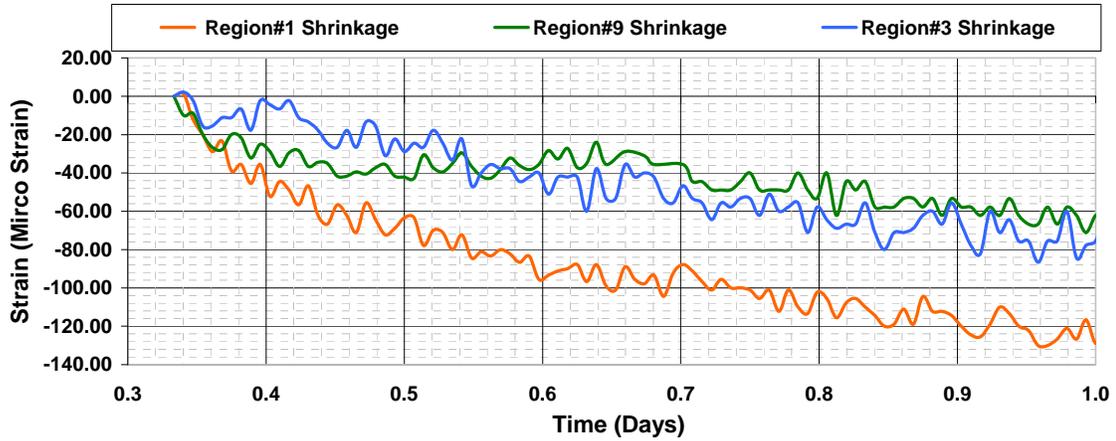
Figure 53: Shrinkage measured in the first 24 hours in unrestrained concrete Prisms for Regions 1, 9 and 3
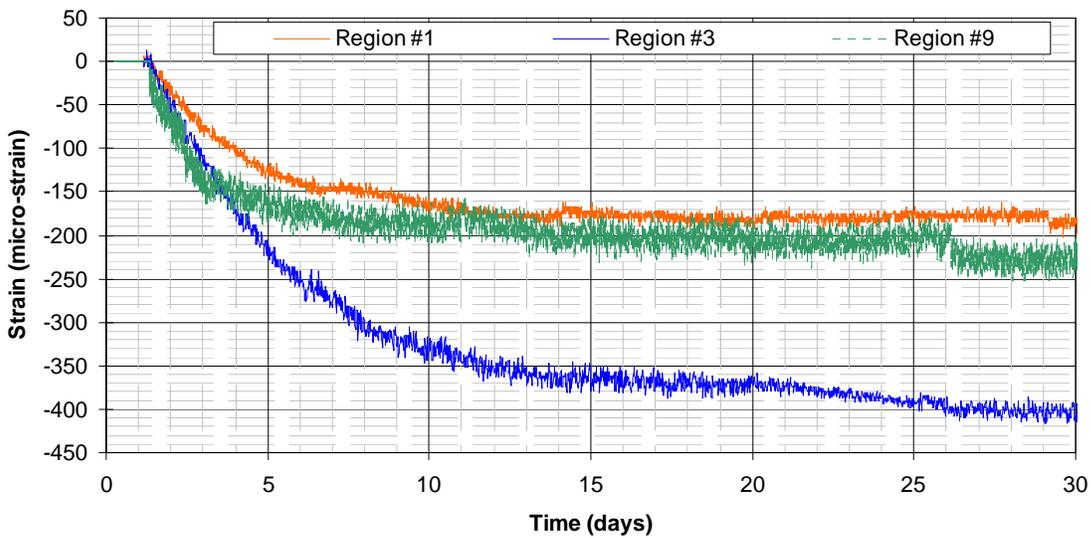
Figure 54: Drying shrinkage from unrestrained concrete Prisms for Regions 1, 3 and 9

Table 19: Tabulated values of Total, drying and autogenous shrinkage for regions 9, 1 & 3

		Time(days)					
		0	**1**	**3**	**7**	**14**	**20**
Region#9	Total Shrinkage	0	-75.55	-285	-383	-461	-509
	Autogenous Shrinkage	0	-75.55	-137	-196	-267	-299
	Drying Shrinkage	0	0	-148	-187	-194	-216
Region#1	Total Shrinkage	0	-144	-282	-397	-480	-510
	Autogenous Shrinkage	0	-144	-195	-257	-311	-326
	Drying Shrinkage	0	0	-86.66	-140	-169	-184
Region#3	Total Shrinkage	0	-91.66	-251	-460.33	-566	-589
	Autogenous Shrinkage	0	-91.66	-127	-167	-198	-216
	Drying Shrinkage	0	0	-124	-293.33	-368	-373

4.7.1.2 Unrestrained Concrete Ring Specimens

A comparison of the total shrinkage obtained from the ring specimens for Regions 1, 3 and 9 is shown in Figure 55. The radial strains up to 2 days are shown in Figure 55(a) for clarity. The shrinkage strain (expressed in microstrain) for each region at different ages are also given in Table 20. Average radial strain, obtained by averaging the values from the two ring specimens for each region were used in the figure and are listed in the table.

Considering the measured radial strains in the first 24 hours, there are some similarities between the observed trends in the strain measured from the ring and the prismatic specimens. Consistent with the observed trends in prismatic specimens, only Region 9 shows an expansion followed by contraction before demolding. Regions 1 and 3 show a continuous volumetric contraction. The influence of expansion produced by the heat of hydration seems to be evident in decreasing the influence of volumetric contraction produced by shrinkage in Region 9. However, unlike the trends obtained from prismatic specimens, the radial strain from Region 3 is larger than the corresponding value obtained from Region 9. This can be attributed to the different mass of concrete in the two specimen geometries, which produces differences in the thermal strains.

Considering the measured radial strains after the first day, the magnitude of radial strain from Region 9 is lower than the corresponding values from the other regions at any age. The largest difference in the radial strains from Regions 1 and 3 occurs at 24 hours after casting. The difference steadily decreases until the values for radial strain are comparable after 14 days.

An indication of the rate of increase in radial strain after demolding when the specimen are subjecting the concrete to drying is obtained from the plot of the increase in radial strain after one day shown in Figure 56. It should be noted that the temperature of the rings was constant after one day and the measured radial strain only corresponds to the volumetric contraction due to shrinkage. It can be seen that initially in the first 14 days, Regions 3 and 9 exhibit a higher rate of increase in radial strain when compared to Region 1. In all regions, the general trend suggests a slowing down in the rate of increase in radial strain after 14 days. The decrease in the rate is more noticeable for Region 9.

Comparing the radial strain produced by shrinkage after demolding the following can be inferred:

(a) Region 1 which has significant shrinkage at one day exhibits the slowest rate of increase in radial strain after one day.

(b) In Region 9, there is a very rapid increase in the radial strain up to 14 days after of age following which there is a steady decrease in the rate. The rates of shrinkage from Regions 3 and 9 are comparable up to 14 days of age.

Some of these observations may now be interpreted in terms of the observed trends in ε_{drying}, $\varepsilon_{autotgenous}$ and ε_{total} obtained from prismatic specimens. In Region 9, the rapid increase in radial strain in the first few days is due the large contribution from drying shrinkage which starts decreasing after 4 days. After demolding, following a rapid increase, ε_{drying} from Region 3 continues to increase at a steady rate. This contributes to the continued increase in the radial strain in the unrestrained rings. However, unlike the measurements from the ring specimens, where the values of radial strain are comparable, the ε_{total} from Region 3 was

larger than the ε_{total} from Region 1 after 14 days. This can be attributed to the difference in the magnitude of drying shrinkage in the two geometries. The volume change after demolding contains contributions from both autogenous and drying shrinkage. It should be noted that the radial strain obtained from the ring specimens after demolding would be different from the ε_{total} obtained from the prismatic specimens because of differences in geometry and the fact that in the rings drying is only allowed from the top and bottom surfaces while the prisms were allowed to dry from all sides.
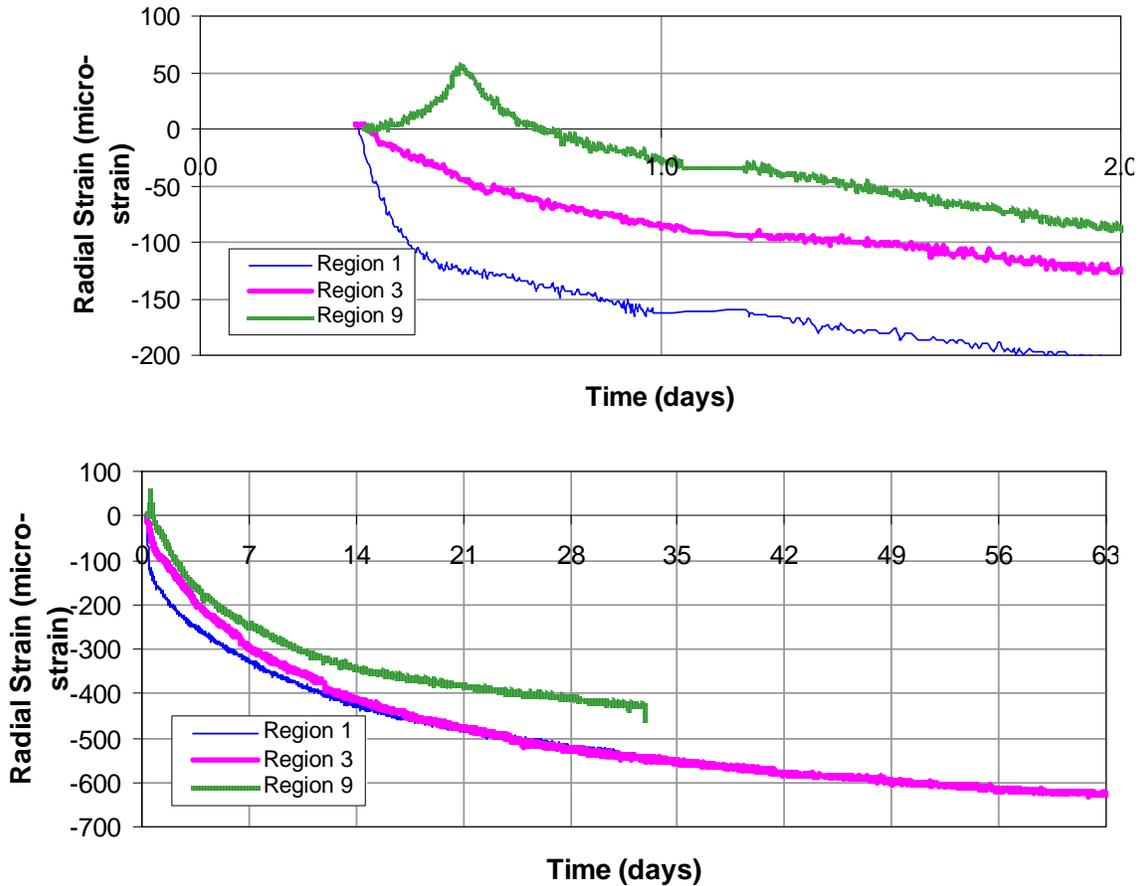
Figure 55: Comparison of the average radial strain from unrestrained concrete rings for Regions 1, 3 and 9.
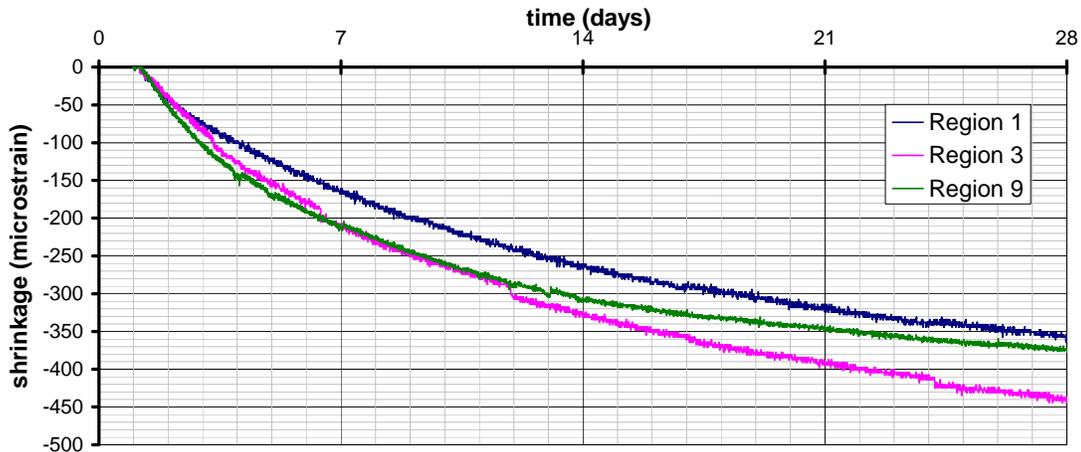
Figure 56: Comparison of the increase in radial strain after 1 day from unrestrained concrete rings for Regions 1, 3 and 9

Table 20: Tabulated values of radial strains for Regions 9, 1 and 3.

	Time(days)					
	0	**1**	**3**	**7**	**14**	**30**
Region#9	0	-62	-177	-273	-368	-443
Region#1	0	-152	-213	-300	-395	-490
Region#3	0	-87	-175	-283	-385	-496

4.7.2 Retrained Shrinkage

Typical temperature variation recorded from the steel rings for Regions 1, 3 and 9 are compared in Figure 57. It can be seen that immediately after casting, the temperature of the steel rings decreases below the datum temperature (temperature of the chamber maintained at 30°C). With time the temperature of the rings rise above the datum due to the heat released by the hydration of cement before approaching the datum. While the temperature profiles for Regions 1 and 3 are nominally identical, the temperature rise recorded in Region 9 is higher than the corresponding temperature rise in the other two regions; Further, the maximum temperature in Regions 1 and 3 is attained earlier in time than the temperature recorded in Region 9. In Regions 1 and 3 there is a 2 degree temperature rise which occurs approximately 7-8 hours after casting. In both regions, following the temperature rise, the temperature of the rings decreases to the ambient level before 24 hours. In Region 9, there is a significantly higher temperature rise, which occurs later in time when compared to the other two regions; the maximum temperature of 6 degrees occurs 12 hours after casting. The temperature of the rings is higher than the ambient level.
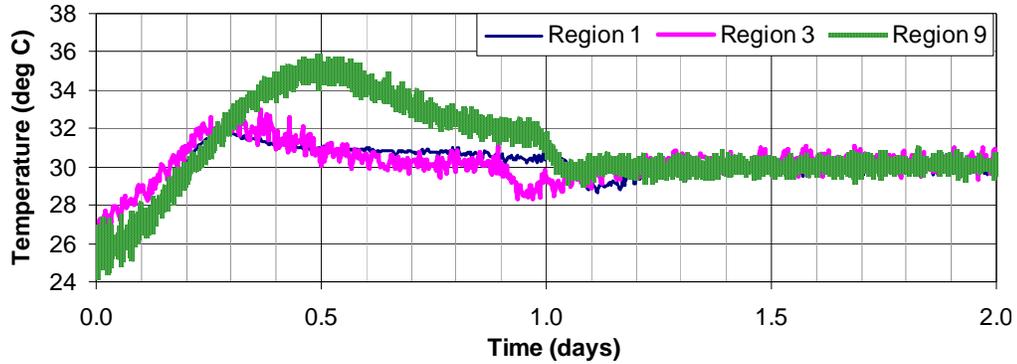
Figure 57: Temperature variation recorded from restrained rings for Regions 1, 3 and 9.

The strains measured from the 18 mm (¾ in) rings in the first 48 hours are shown in Figures 58 (a), (b) and (c) for Regions 1, 3 and 9, respectively. Since temperature variation of steel can produce changes in the measured strain, the total tangential strain measured on the steel ring is a combination of thermal expansion/contraction and the interfacial pressure exerted by concrete shrinkage and is given as

$$\varepsilon_{\theta\theta}^{total} = \varepsilon_{\theta\theta}^{\Delta T} + \varepsilon_{\theta\theta}^{P_i} \qquad (7)$$

where $\varepsilon_{\theta\theta}^{total}$ is the measured tangential strain, $\varepsilon_{\theta\theta}^{\Delta T}$ and $\varepsilon_{\theta\theta}^{P_i}$ are the tangential strains produced by a change in temperature and by the applied interface pressure, respectively. Immediately after casting, the temperature of steel rings, which were initially in thermal equilibrium with the environment (maintained at 30°C), drops by approximately 3 to 4 degrees Centigrade (5 to 9 degrees Fahrenheit). Therefore, the thermal strain at age zero (time of casting), is not equal to zero and corresponds to the strain produced by the decrease in temperature. As time progresses, both the steel and concrete temperatures increase. In the first few hours after casting, the stiffness of concrete is insignificant compared to the stiffness of steel. The steel ring therefore undergoes unrestrained thermal expansion. To provide a zero reference for the measured strain, strain was set equal to zero when the temperature during the initial rise was equal to the ambient temperature. At this stage concrete does not providing any restraint and since the temperature of the ring is equal to the datum, the thermal strain is zero and the measured strain would be identical to the true strain. The recorded strain should therefore be zero. In the case of Regions 1 and 3 the temperature of concrete reaches the datum temperature before demolding. In Region 9 on the other hand, the temperature of the steel ring is slightly higher than the datum at one day and it approaches the ambient temperature very rapidly after demolding. There are little or no changes in temperature after demolding. Therefore, the thermal strains produced after demolding are insignificant (remain close to zero). After the concrete attains thermal equilibrium, the increments in measured strains are equal to the increments of true strain and any changes in the strain are due to increase in interfacial pressure.

It is interesting to note that there is some compression in the steel rings at the time of demolding. The level of compression corresponds with residual stress in the steel ring following the temperature rise and the subsequent decrease to ambient level. The average residual strain in the steel ring is equal to 10.2 με, 12.5 με and 21.3 με for Region 1, 3 and 9, respectively. Region 9, which had the highest rise in temperature, also has the highest level

of residual compressive strain in steel ring at the time of demolding. Since the residual compression in the steel ring results in tension in the concrete ring, it can be concluded that concrete in Region 9 has the highest level of tensile stresses after the initial temperature rise and subsequent cooling of concrete.
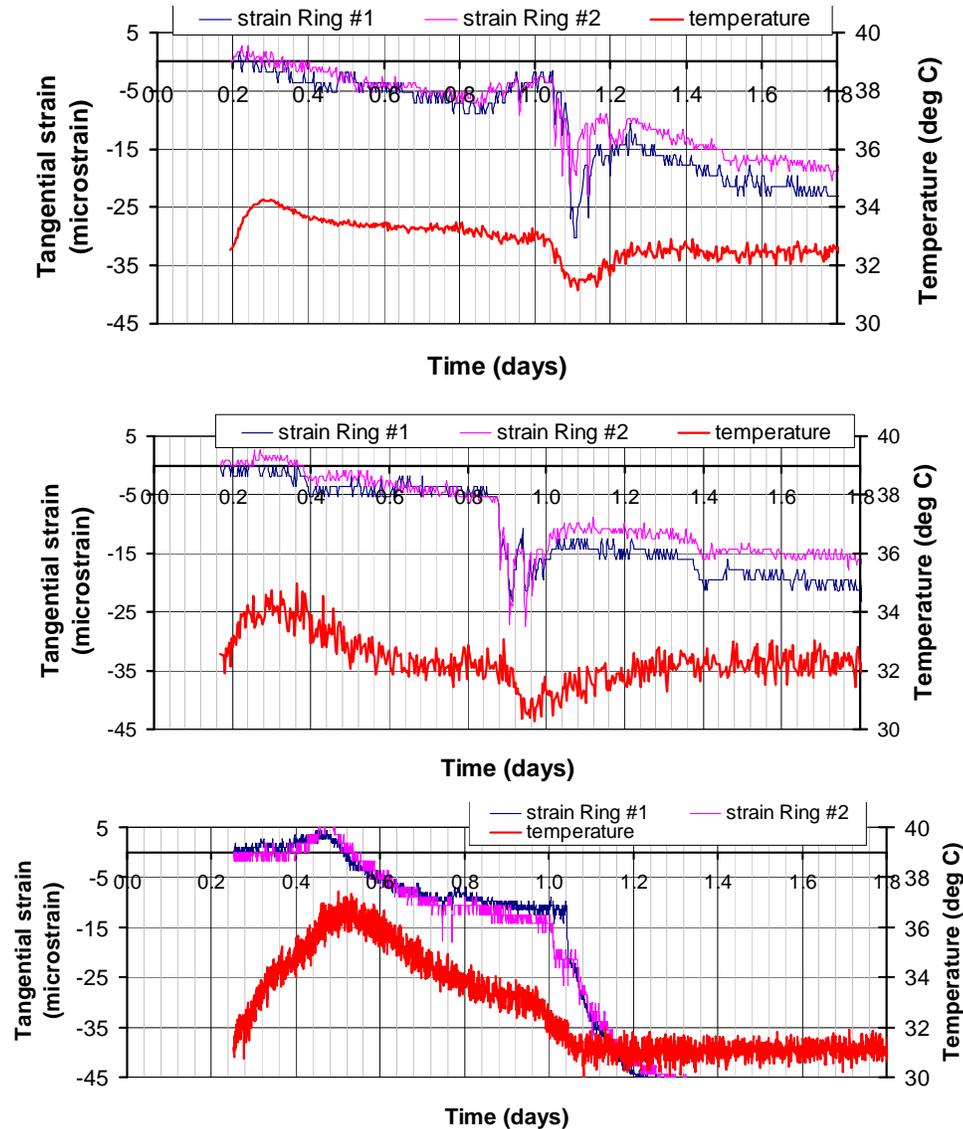
Figure 58: Radial strains and temperature in the first 2 days (a) Region 1; (b) Region 3; (c) Region 9.

The tangential strains recorded from the 12 mm (½ in) and the 18 mm (¾ in) steel rings for Regions 1, 3 and 9 are shown in Figures 59, 60 and 61, respectively. It can be seen that in all cases, there is a rapid increase in the level of compression immediately after demolding as the concrete starts to dry. There is however a decrease in the rate with time. Sudden jumps in strain indicate the formation of a stress-relieving crack in the concrete, which decreases the level of compressive stress in the ring (and hence the stress exerted by the concrete). The

time of cracking is shown marked on the graphs. The values of tangential strains and the age of concrete at cracking are summarized in Table 21.

Region#1

There is a large variability in the restrained shrinkage behavior obtained from the two 0.5 in rings. While one ring exhibited cracking, the second ring, which had a higher level of compressive strain did not exhibit any signs of cracking. Further, cracking in the 12 mm (½ in) ring was observed to occur earlier in time than the 18 mm (¾ in) rings. Ring #1 of 12 mm (½ in) thickness, exhibited signs of cracking at 15.9 days while the two 18 mm (¾ in) rings cracked at 17.9 and 25.8 days. The occurrence of a crack is indicated by a sudden decrease in strain and was also confirmed by visual observation of a crack on the concrete surface. It is interesting to note that immediately following the jump, there is still a significant level of compressive strain in the ring and the strain continues to decrease with time. The cracking in Ring #1 suggests that there was possibly a weak plane where the level of stress was sufficient to produce cracking in the mortar matrix This suggests that while a crack was formed, there was sufficient stress transfer across the crack, provided by crack bridging effect of aggregate, which did not allow the stress in concrete to decrease to zero. While the formation of the crack provides some stress relief, the ability of the material to transfer stress across the crack results in an increase in stress in the material produced by continuing shrinkage. The level of restraint provided by the ½ in ring is not sufficient that the increase in stress due to continuing shrinkage is greater than the residual strength provided by the bridging effect. The existence of crack bridging mechanisms could not be verified by visual observations from the surface of the specimen.

Region#3

The strains from both rings of a given thickness are comparable at all ages. None of the rings cracked up to 60 days indicating a very low potential for restrained shrinkage cracking.

Region#9

From Figure 61 and Table 21, all rings cracked within 30 days after casting. There was however considerable variation in the age of cracking. The first concrete ring restrained with a 18 mm (3/4 in) thickness cracked after only 12 days while the other ring cracked after 26 days. The two 12 mm (½ in) rings cracked after 21 and 30 days. In 12 mm (½ in) rings, Ring #1 which showed a faster rate of increase in tangential strain cracked earlier. The results from the 18 mm (¾ in) rings on the other hand are very consistent. The ring with the higher tangential strain cracks earlier.

Table 21: Time and strain at cracking in restrained ring tests for Regions 1, 3 and 9

Restrained Rings	Region #1		Region #3		Region #9	
	Time @ Cracking (days)	Strain @ Cracking (με)	Time @ Cracking (days)	Strain @ Cracking (με)	Time @ Cracking (days)	Strain @ Cracking (με)
Ring#1- 12mm (0.5")	15.9	-85	no crack up to 60 days	---	30.6	-133
Ring#2- 12mm (0.5")	no crack up to 35 days	---	no crack up to 60 days	---	21.6	-107
Ring#1- 18mm (0.75")	25.8	-58	no crack up to 60 days	---	26.2	-89
Ring#2- 18mm (0.75")	17.9	-62	no crack up to 60 days	---	12.3	-92
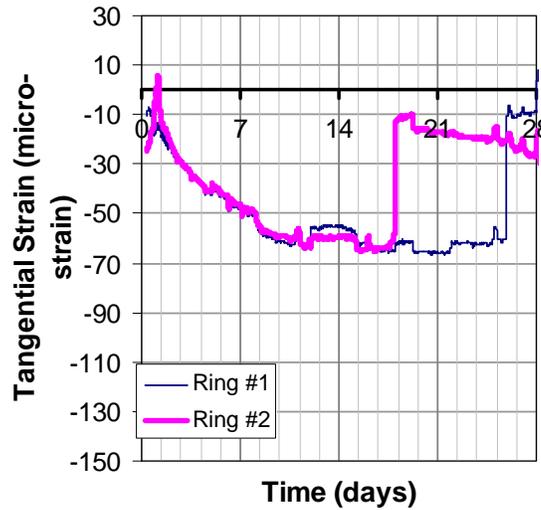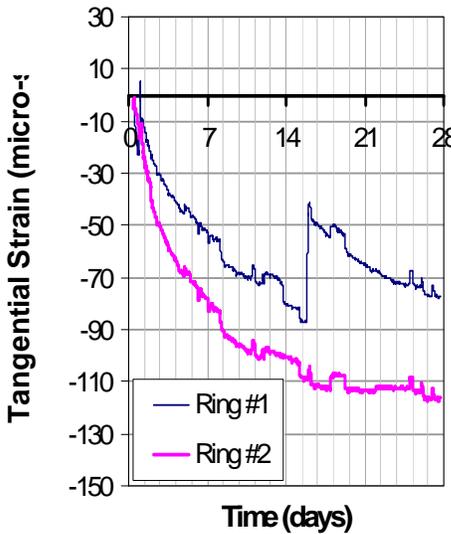
Figure 59: Tangential strain development in restrained rings for Region 1
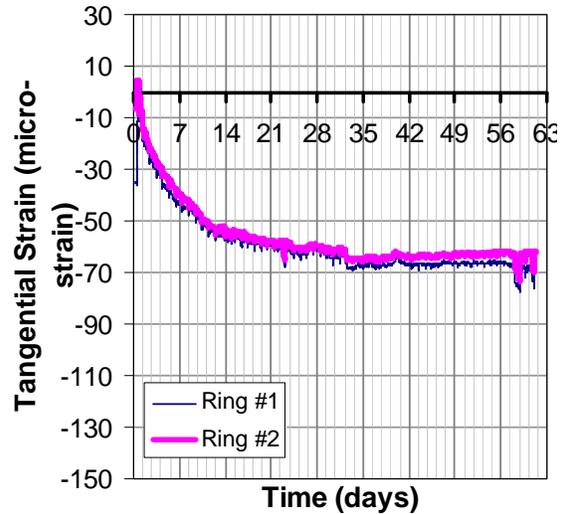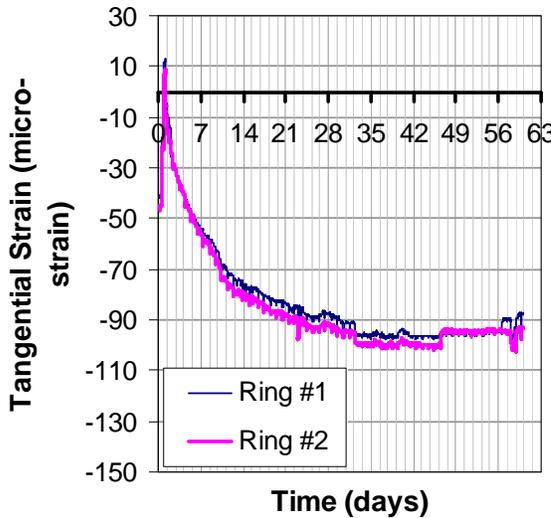
Figure 60: Tangential strain development in restrained rings for Region 3
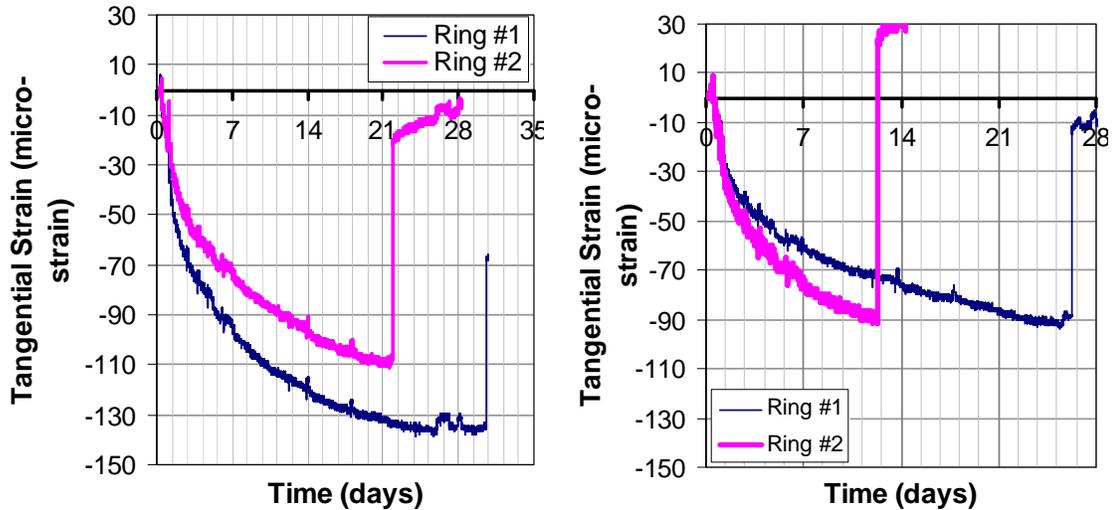
Figure 61: Tangential strain development in restrained rings for Region 9

Few observations which are common for all regions are listed below:

(1) The variability in the age of cracking is strongly influenced by variability in tensile strength between specimens. Evidence in support of this statement can be obtained by comparing the strains in ¾ in rings from Region 1. While the strains from both rings are comparable at all ages, cracking is produced at an earlier age in one ring. Further, in the ½ in rings from Region 9, Ring # 2 which had a slower rate of increase in tangential strain cracked earlier than Ring #1, which had higher tangential strain.

(2) Strains in ½ in rings are higher than the strains in ¾ in rings. This is consistent with the fact that ¾ in rings are stiffer and offer a higher level of restraint to free shrinkage of concrete. Therefore larger magnitude of applied larger stress is required to produce a unit change in the measured strain in the ¾ in rings.

4.7.3 Discussion of Shrinkage Tests

The observed trends in the autogenous and drying shrinkage provide an indication of the reactivity of the cementitious materials used in the three regions. Autogenous shrinkage is produced by a reduction in the free water in the cementitious material on account of the hydration reaction. Drying shrinkage on the other hand is a result of loss of the free water from the concrete produced by evaporation due to drying. Both drying and autogenous shrinkage are produced by a loss of water from the pore system of the cementitious matrix which in turn depends upon the pore structure. The results of the three regions can now be re-evaluated and compared to provide an insight into the role of the cementitious materials in determining the free shrinkage in concrete.

- After the concrete reached thermal equilibrium with the environment following the initial thermal expansion produced by the heat of hydration, Region 9 had the highest rate of increase in autogenous shrinkage. In this region, within the first 24 hours, the initial volume decrease produced by autogenous shrinkage was countered by the thermal expansion. The rapid increase in autogenous shrinkage after 24 hours indicates that there is a very rapid evolution of microstructure which produces a decrease in the free water within the cementitious matrix under sealed conditions. The large drying shrinkage

83

recorded in Region 9 in the first few days suggests that initially in the first few days the cementitious matrix has a large open pore structure and initially there is a large availability of free water. The subsequent reduction in the rate of drying shrinkage after few days suggests the evolution of microstructure, which decreases the free water and results in a finer pore structure, which does not allow easy movement of water within the internal structure. This suggests that the blended silica fume is very reactive in the first few days, which brings about rapid changes in the microstructure and a reduction in the available free water.

- While Region 1 had the highest magnitude of autogenous shrinkage it had the lowest drying shrinkage. A significant portion of the autogenous shrinkage in Region 1 occurs in the first day after casting. The rates of increase in autogenous shrinkage from Region 1 after 1 day are however lower than the rate of autogenous shrinkage in Region 9. This suggests that the combination of silica fume and GGBFS exhibits very high early reactivity within the first few hours after casting. The pore structure of the cementitious matrix, which forms after 1 day, is primarily composed of small sized pores which do not dry up easily.

- The results from Region 9 are in contrast with Region 3, which had the highest drying shrinkage and the lowest autogenous shrinkage. The high value of drying shrinkage suggests that there is a large availability of free water in the system and the presence of large diameter pores, which lose water rapidly upon drying. Further, low values of autogenous shrinkage indicate a slower rate of consumption of free water in the cementitious matrix and a slower rate of development of the microstructure under sealed conditions. These results suggest that cementitious material from Region 3 comprising of combination of silica fume and fly ash is the least reactive of other combinations of cementitious materials used in this study.

The trends in the autogenous and drying shrinkage are also consistent with observed increase in elastic modulus with age. Region 1 which had the most rapid increase in elastic modulus in the first 24 hours also exhibits the fastest rate of increase in autogenous shrinkage up to 24 hours. Consistent with this observation, Region 3, has the slowest rates of increase in elastic modulus and autogenous shrinkage at an age. Region 9 exhibits the fastest rate of increase in autogenous shrinkage after 24 hours which is in agreement with the highest rate increase in elastic modulus after one day. Autogenous shrinkage and development of material properties are directly related to the degree and rate of hydration, which in turn is related to the reactivity of the cementitious material. The differences in the cementitious materials used in the different regions, therefore, contribute to significant differences in the rates of elastic material properties and autogenous shrinkage.

The total shrinkage measured in the ring specimens from Regions 1 and 3 is comparable after 14 days, while the total shrinkage from Region 9 is lower than the corresponding values from the other two regions at any age. There is, however, a significant delay in the age of restrained shrinkage cracking for Region 3 when compared with the other two regions. Since the total volume change produced by total shrinkage in Region 3 is either comparable or higher than the corresponding value from the other two regions after 14 days, this suggests that tensile stress in the material for a given level of shrinkage is lower for Region 3 than for the other two regions. The elastic modulus from Region 3 was lower than the corresponding values from the other two regions at any age. Further, concrete which exhibited a high early

rate of modulus increase exhibited earlier cracking in ring tests (Region 1 and 9). Therefore there is a direct correlation between the increase of elastic modulus and age of cracking. It can be concluded that the potential for restrained shrinkage cracking would increase when there is a rapid increase in elastic modulus concurrent with an increase in volumetric contraction produced by shrinkage.

4.7.4 Analysis of Restrained shrinkage behavior

The restrained shrinkage test geometry can be idealized as a problem of compound cylinders, which is commonly analyzed in classical textbooks on Elasticity (Timoshennko and Goodier 1982). In this case, the steel and concrete rings are the inner and outer cylinders, respectively. Initially after casting the outer radius of steel ring is equal to the inner radius of the concrete cylinder. In concrete, volumetric changes are produced due to combined effects of shrinkage and temperature changes. Volumetric changes are also produced in the steel ring by temperature changes associated with the heat released by hydration reaction. When the volumetric changes in the concrete result in a decrease in the inner radius of the concrete ring relative to the outer radius of the steel ring, interfacial pressure in produced between the two materials (shown in Figure 62). For equilibrium, the interface pressure between the two materials produces tensile stress in the concrete ring while compressive stress is produced in the steel ring. The compressive stress in the steel ring is directly proportional to the interface pressure resulting from the restrained shrinkage of concrete. The increase in the free shrinkage of concrete should therefore produce a continuous increase the level of compression in the steel ring. Correspondingly there is also an increase in the tensile stress in concrete. The tangential strain in the steel rings is therefore indicative of the magnitude of tensile stress in concrete.
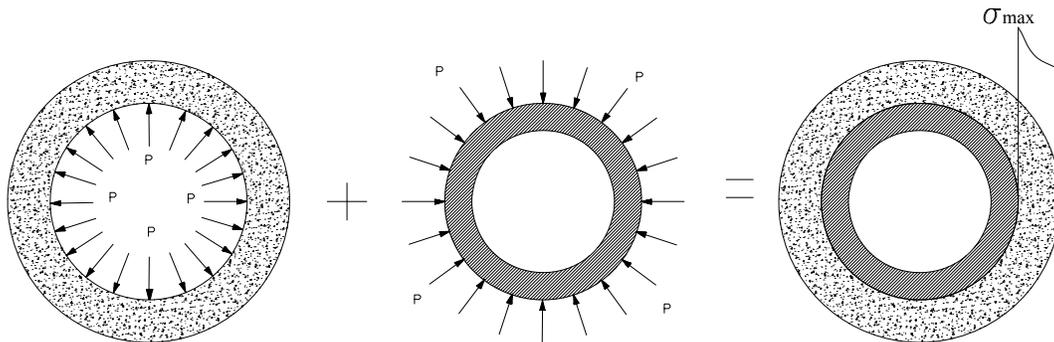
Figure 62: Schematic representation of the restrained ring as a compound cylinder

The actual interface pressure could be directly determined from the measured tangential strain in the steel cylinders. From classical elasticity, the relationship between the applied pressure on the outer surface of an elastic cylinder and the tangential strain on the inner surface of the cylinder is given as

$$P_i = -\left(\frac{b^2 - a^2}{2b^2}\right)\varepsilon_{\theta\theta}E_s \qquad (8)$$

where, $\varepsilon_{\theta\theta}$ is the measured tangential strain, b and a are the outer and inner radii of the steel cylinder, respectively and E_s and ν_s are the elastic modulus and Poisson's ratio, respectively of steel. It should be noted that equation 8 could be applied directly to evaluate the actual interface pressure from the measured tangential strain in the steel rings since the steel rings remain elastic throughout the test procedure.

Since the 18 mm (¾ in) rings provided consistent results, which allows for a relative comparison of the stress development in the three regions, further analysis of the different mechanisms which contribute to cracking is performed using only the results obtained from the 18 mm (¾ in) rings. Figure 63 shows the interface pressure between steel and concrete cylinders for all three regions. The magnitude of interface pressure provides a good indication of the difference in performance under conditions of restrained shrinkage. Since the magnitude of interface pressure is indicative of the tensile stress in concrete, it can be seen that there is a good correlation between the interfacial pressure and the observed age at cracking. Region 9 has a significantly higher residual stress after one day, which contributes a higher magnitude of stress at any age. Within the two rings tested for Region 9, Ring #2 exhibits the fastest rate of increase in interfacial stress, which leads to earlier cracking. Ring #1, on the other hand, which has a lower magnitude interfacial pressure at any age cracks at a later age. The level of the interfacial pressure at cracking in Ring #1 is higher than the pressure at cracking for Ring #2 due to the increase in strength of concrete with age. A larger tensile stress would be required to produce a crack at a later age. Region 3, which has insignificant level of residual stress after one day and a slow rate of stress development, does not exhibit any cracking. Comparing Regions 1 and 9, it can be seen that the interfacial pressure at cracking is higher for Region 9 than the corresponding pressure obtained from Region 1. It should be noted that Region 9 had the highest strength and of the three Regions and did not show any signs of strength retrogression.

Considering results of restrained ring tests, the tensile stress in concrete due to restrained free shrinkage depends upon two key factors: (a) the residual stress when the steel and concrete reach thermal equilibrium with the environment; and (b) the rate of stress increase due to the restraint to shrinkage. Each of these factors is now examined in detail.

To evaluate the rates of stress development in the different regions, the increase in the interfacial pressure relative to the residual pressure at one day is plotted in Figure 64. It can be seen that Region 3 has the slowest rate of increase in interfacial pressure. The rates of increase in the interface pressure are comparable for the Regions 1 and 9. There is however a significant difference in the age of cracking. For instance, while Ring#2 for Regions 1 and 9 have comparable rates of increase in interfacial pressure, the ring from Region 9 cracks earlier. The observed differences in the ages of cracking can be resolved if the initial stress at one day are also considered. The residual stresses for Region 9 are significantly higher than the corresponding stress for Region 1, which result in higher magnitude of stress.
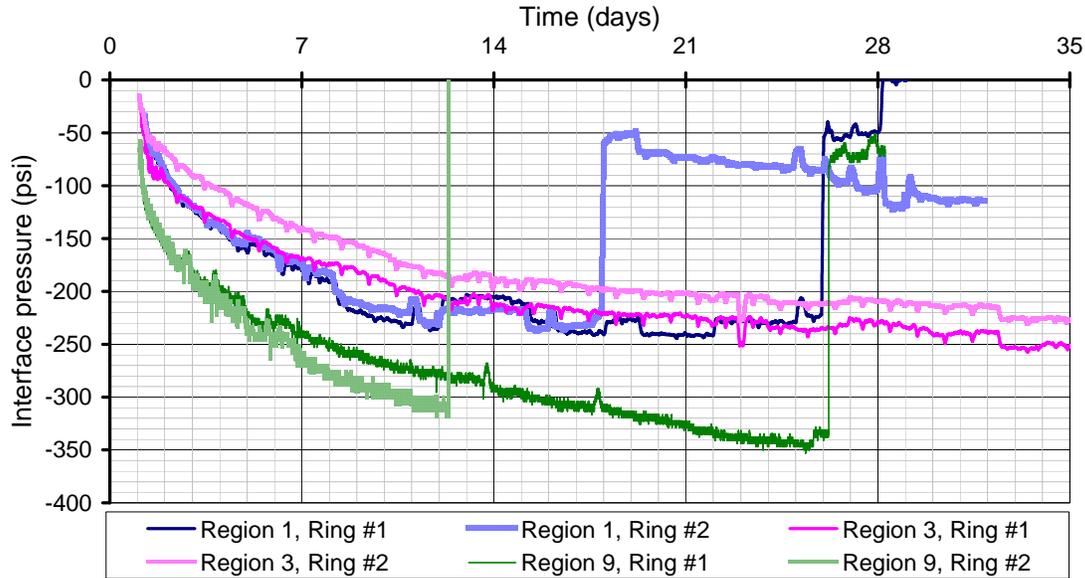
Figure 63: Interfacial pressure between the steel and concrete in the ¾ in rings for Regions 1, 3 and 9.

The available results can now be evaluated considering the factors which influence to the rate of stress increase in addition to the rate of volumetric contraction associated with shrinkage: (a) the magnitude of elastic modulus and (b) the rate of increase in the elastic modulus.

- The role of the absolute magnitude of elastic modulus can be evaluated comparing the rates of stress development in Regions 1 and 9. While the rates of increase of shrinkage strain and elastic modulus are higher for Region 9, the rate of stress increase from the two regions is comparable. This can be explained considering that the magnitude of elastic modulus from Region 1 is significantly higher than the corresponding value from Region 9, which results in a higher stress in the material for a smaller value of restrained strain.

- The role of rate of modulus increase can be evaluated by comparing the rates of stress development in Regions 3 and 9. The rates of increase in shrinkage strain from the two regions are comparable in the first 14 days. The difference in the absolute values of elastic moduli from the two regions is also not significant. The rate of increase in elastic modulus from Region 9 is however significantly higher, which contributes to a much higher rate of stress development when compared to Region 3.

The available results suggest that the potential for restrained shrinkage cracking depends upon the rates of increase in both shrinkage and elastic modulus. If only the increase in shrinkage is considered as the driving factor for predicting the restrained shrinkage cracking, as suggested by Hossain and Weiss (2003) then the differences in the stress development in Regions 3 and 9 cannot be explained satisfactorily.
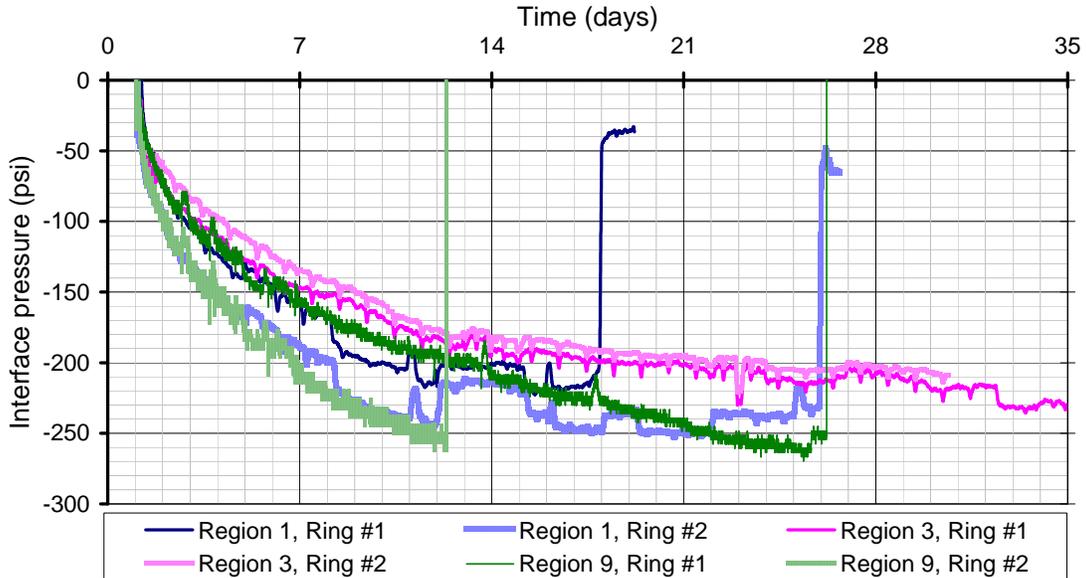
Figure 64: Rate of increase in interfacial pressure after 1 day for Regions 1, 3 and 9.

At the end of the first 24 hours there is a significant level of compressive stress in the steel rings in Region 9 when compared to Regions 1 and 3. The level of the residual compression in the steel rings is indicative of the magnitude of tension in concrete. It is clear that a higher temperature rise produced by heat released by hydration is associated with a higher magnitude of residual tension in concrete when the concrete and steel approach thermal equilibrium with the environment. After the steel and concrete rings reach thermal equilibrium with the environment, there is a residual level of compression in the steel rings, indicating that the concrete in tension. This suggests that following the initial heating and cooling, the combined action of shrinkage and thermal movement (expansion and contraction) would produce tension in concrete which is designed for composite action with steel. This is in agreement with the previous observation made from instrumented bridges where the initial expansion and contraction of steel and concrete were found to produce a residual compression in the top flange of the steel girder, thus producing tension in the concrete deck. Comparing the early response in the measured strains from the 3 regions it is obvious that the largest residual compression in the steel rings is produced in Region 9, which had the highest rise in temperature during early hydration.

The age of cracking for each region varied significantly for identical specimens for concrete from within each region. One reason for this discrepancy might be due to the large size of the coarse aggregate relative to the thickness of the concrete in the restrained ring specimen. As the aggregate size increases, a larger size of concrete is required to overcome the variations produced by the inhomogeneity resulting from the aggregate. In order to decrease the influence of the aggregate size a larger thickness and height of the concrete in the rings would be required.

4.8 Conclusions and Findings

Based on the results of the experimental investigation the following conclusions can be drawn

1. ***The results of shrinkage measurements indicate the importance of considering the local material properties.***

   a. Differences in <u>cementitious material</u> contribute to significant differences in values of autogenous and drying shrinkage. Specifically,

      i. The combination of silica fume and GGBFS used in Region 1 exhibited the highest autogenous shrinkage within the first day. This cementitious mixture however had the lowest drying shrinkage at any age when compared with combination of silica fume and fly ash used in the other regions.

      ii. The combination of silica fume and fly ash used in Region 3 produced the highest drying shrinkage and the lowest autogenous shrinkage at any age when compared to the other combinations of cementitious materials used in the other regions including a combination of silica fume and fly ash where cement blended with silica fume was used.

      iii. The combination of silica fume and fly ash where cement blended with silica fume used in Region 9 exhibits a delayed temperature rise due to heat of hydration when compared with the other two regions. The maximum temperature attained by concrete is also higher compared to the other two regions. Only cement blended with silica fume exhibited thermal expansion in the first 24 hours which decreased the net volumetric contraction resulting from autogenous shrinkage.

      iv. Once the concrete reached thermal equilibrium following the initial heating produced by heat of hydration, the fastest rate of increase in autogenous shrinkage was obtained from the combination of silica fume and fly ash, when the cement blended with silica fume was used. Cement blended with silica fume results in more rapid increase in autogenous shrinkage when compared to silica fume added separately to the mix.

   b. Differences in the <u>aggregate and the cementitious material</u> contribute to significant differences in the performance of concrete under restrained shrinkage. Specifically,

      i. The concrete mixture from Region 3 has a very low potential for cracking under restrained shrinkage. Although the concrete mixture exhibits a high rate of shrinkage, a slower rate of increase and a lower magnitude of elastic modulus contribute to a slower rate of stress development and a lower magnitude of stress under restrained conditions. The combination of silica fume and fly ash and the gravel aggregate result in a slower rate of increase and a lower magnitude of elastic modulus.

      ii. Experimental evidence suggests that there is higher potential for restrained shrinkage cracking when there is a rapid increase in elastic modulus concurrent with an increase in shrinkage. Region 9 which had higher increases in elastic modulus exhibit a faster increase in the actual interface pressure between steel and concrete rings in the restrained ring tests and hence an earlier age of cracking under conditions of restrained shrinkage. A combination of silica fume and fly ash, where silica fume blended with cement provides for the most rapid increase in elastic modulus and shrinkage.

      iii. While the combination of silica fume and GGBFS used in Region 1 did provide any significant improvements in the rate of modulus increase when compared

with the combination of silica fume and fly ash used in Region 3, the crushed stone used in Region 1 resulted in a higher magnitude of elastic modulus at any age. This resulted in a higher value of stress and hence cracking, even though the rate of shrinkage was the lowest in this region.

2. The observed autogenous and drying shrinkage obtained from the three regions point to differences in the reactivity of the cementitious materials. A faster increase in autogenous shrinkage suggests a higher reactivity of the cementitious materials in Regions 1 and 9. The trends in the autogenous and drying shrinkage are consistent with observed increase in elastic modulus with age. Concrete from Regions 1 and 9 also exhibited the fastest increase in elastic modulus with age.

3. The experimental evidence from the restrained response of concrete suggests the following:

    a. The stress in concrete for a given level of restraint depends upon the following: (1) the initial residual stress in steel and concrete after both materials undergo the initial thermal expansion due to heat of hydration; and (2) rate of stress development in concrete, which in turn depends upon the rate of increase in shrinkage, the magnitude and the rate of increase in elastic modulus.
    b. A larger temperature rise in the first day after mixing is associated with a larger magnitude of residual stress when the concrete reaches thermal equilibrium with the environment. The residual stress at one day contributes significantly to the total magnitude of the stress produced by shrinkage.
    c. The potential for restrained shrinkage cracking would increase when (a) *there is a rapid increase in elastic modulus concurrent with an increase in shrinkage*; or (b) *the increase in the shrinkage strain occurs when the material has a high elastic modulus*.

Section 5: Statement on Implementation

The research presented here provides an insight into the early age response of concrete in a steel girder bridge with a composite deck. The level of stress depends upon material, structural and environmental effects. Material composition and environmental conditions influence the expected levels of expansion and contraction. For a given material composition, the stress in the concrete deck depends upon the stiffness of the girders and the fixity conditions of the girders and the deck. Design practices which ensure that the thermal movements of the girders and the concrete deck slab are in phase throughout the length of the bridge would help minimize thermal-stress in concrete. Construction practices which would reduce total increase in temperature, and the rate of temperature decrease of concrete, relative to the top flange in the initial 48 hours after casting would decrease the early-age stress in concrete due to thermal movement. The temperature rise in concrete can be minimized if the temperature rise by hydration is out-of-phase with the daily temperature variation. This can be achieved by casting in the late afternoon or early evening as suggested by Wojcik et al. (2003). The level of shrinkage can be minimized through a control of material mixture design, use of admixtures and good curing practices.

Recommendations for minimizing the premature cracking in HP concrete decks related to restrained volumetric contraction are developed from the results of this investigation.

- It is important to reduce the total temperature rise and the temperature gradient across the steel girder to minimize the level of tensile stress in concrete in the first few days after casting, while the concrete goes through the heating and cooling produced by hydration heat. This would decrease the level of tensile stress in concrete due to restrain of thermal movement.

- The local materials should be carefully evaluated before use in HP concrete.
  - If silica fume is used it should only to be added separately to the mix, unless the reactivity of blended silica fume is established and found comparable to silica fume addition.
  - Only the use of Type I/II or Type II cement should be permitted.
  - When ground granulated blast furnace slag is used, it should be evaluated to ensure that it does not provide high early reactivity.

SECTION 6: REFERENCES

1. AASHTO/NSBA Steel Bridge Collaboration, Steel Bridge Bearing Design and Detailing Guidelines, p. 5, 2004.

2. ACI 209 R-92, Prediction of Shrinkage, Creep and Temperature Effects in Concrete Structures, American Concrete Institute, Farmington Hills, MI

3. ACI 363 R-92, *State-of- the-Art Report on High Strength Concrete,* American Concrete Institute, Farmington Hills, MI.

4. ASTM, Annual *Book of ASTM Standards, Vol. 04.02: Concrete and Aggregates*, Philadelphia, PA, 1994.

5. Aictin, P.C., and Mehta, P.K., (1990) "Effect of coarse aggregate characteristics on mechanical properties of high strength concrete," *ACI Material Journal*, Volume 87, No. 2, pp 103-107.

6. Alampalli, S., and Owens, F., (2000) "In-Service Performance of High Performance Concrete Bridge Decks," *Transportation Research Record,* Journal of the Transportation Research Board, Vol. 1696, No. 2, pp. 193-196.

7. Arioglu, N., Canan, G.Z., and Arioglu, E., (2006) "Evaluation of ratio between splitting tensile strength and compressive strength for concretes up to 120 MPa and its application in strength criterion," *ACI materials journal*, Vol. 103, No.1, pp. 18-24.

8. Browning, J., and Darwin. D., (2007) "Specifications o Reduce Bridge Deck Cracking," Bridge Views, Issue No. 46, p. 1-2

9. D'Ambrosia, M.D., Lange, D.A., Grasley, Z.C., Lee, C.J., Altoubat S. and Roesler, J.R., (2005), "Instrumentation and Analysis of High Performance Concrete Bridge Decks," TRB, January, Washington D.C., USA.

10. De Larrard, F., and Aitcin, P.C., (1993) "Apparent Strength Retrogression of Silica-Fume Concrete," *ACI Materials Journal*, Volume:90, No. 6, Pages:581-585

11. Darwin, D., Browning, J., Lindquist, W.D., (2004), "Control of Cracking in Bridge Decks: Observations from Field," *Journal of Cement Concrete and Aggregates*, ASTM, Vol. 26, Issue 2.

12. Farney, D.N., and Zoghi, M., (2006), "In-service Analytical Investigation of Precast Concrete Short Span Bridges with Integral Abutment Walls," *Advances in Structural Engineering*, Vol. 9, No. 2, pp. 213-227.

13. French, C., Eppers, L., Le, Q., and Hajjar, J.F., (1999), "Transverse Cracking in Concrete Bridge Decks," *Transportation Research Record*, Various Bridge Design Issues, Bridges, Other Structures, Hydraulic and Hydrology, Transportation Research Record, National Research Council, National Academy Press, Vol. 1688, pp. 21-29.

14. Holt, E., (2001), "Early Age Autogenous Shrinkage of Concrete," Espoo 2001, Technical Research Center of Finland, VTT Publications, Publication 446.

15. Hossain, A., Pease, B., and Weiss, W. J., "Quantifying Early-Age Stress Development and Cracking in Low w/c Concrete Using the Restrained Ring Test with Acoustic Emission," Transportation Research Record, Concrete Materials and Construction 1834, 2003, pp. 24-33

16. Issa, M.A., (1999), "Investigation of Cracking in Concrete Bridge Decks at Early Ages," *Journal of Bridge Engineering*, Vol. 4, No. 2, pp. 116-124.

17. Kada, H., Lachemi, M., Petrov, N., Bonneau, O., Aictin, P.C., (2002) "Determination of the coefficient of thermal expansion of high performance concrete from initial setting," *Materials and Structures*, Vol. 25, pp. 35-41.

18. Krauss, P.D., and Rogalla, E.A., (1996), "Transverse Cracking in Newly Constructed Bridge Decks," National Cooperative Highway Research Program Report 380, Transportation Research Board, National Research Council, Washington, DC.

19. Leslie, J.R. and Cheeseman, W.J., (1949) "An ultrasonic method for studying deterioration and cracking in concrete structures," Amer. Concrete Inst., Proceedings, Vol. 46, pp. 17-36.

20. Mohr and Hansen, W., (1997), "

21. Myers, J.J., (1999), "How to Achieve a Higher Modulus of Elasticity," *HPC Bridge Views*, FHWA, Sponsored, NCBC Co-Sponsored Newsletter, Issue No.5, Sept/Oct 1999.

22. Standard Specifications − Construction and Materials, New York State Department of Transportation, 2002,

23. Prenger, H.B., (1992), "Bridge deck cracking, Research report," Rep. No. MD-93-04, Maryland Department of Transportation, State Highway Administration, Baltimore, MD.

24. Ramey, G.E., Wolff, A.R., and Wright, R.L., (1997), "Structural design actions to mitigate bridge deck cracking," *Practice Periodical on Structural Design and Construction*, Vol. 2, No. 3, p 118-124.

25. Roeder, C., (2003), "Proposed Design Method for Thermal Bridge Movements," *Journal of Bridge Engineering*, Vol. 8, No. 1, pp. 12-19.

26. Schmitt, T.R., and Darwin, D., (1999), "Effect of Material Properties on Cracking in Bridge Decks," *Journal of Bridge Engineering*, Vol. 4, pp. 8-13.

27. Shah, S.P., Weiss, J.W., and Yang W., (1998) "Shrinkage cracking - can it be prevented?," *Concrete International*, v 20, n 4, p 51-55.

28. Timoshenko, S.P., and Goodier, J.N., (1970) "Theory of Elasticity," 3rd edition, McGraw Hill, New York.

29. Waszczuk, C.M., (1999) "Crack Free HPC Deck – New Hampshire's Experience," *Bridge Views*, Issue No. 4, Jul/Aug.

30. William, G.,W., Shoukry, S.N., and Riad, M.,Y., (2005), "Early Age Cracking of Reinforced Concrete Bridge Decks," *Bridge Structures*, Vol. 1, No. 4, pp. 379-396.

31. Wojcik, G.S., and Fitzjarrald, D.R., (2001). "Energy balances of curing concrete bridge decks," *Journal of Applied Meteorology*, 40 (11), pp. 2003-2025.

32. Wojcik, G.S., Fitzjarrald, D.R., and Plawsky, J.L., (2003), "Modelling the interaction between the atmosphere and curing concrete bridge decks with the SLABS model," *Meteorological Applications,* Vol. 10, pp. 165-186.

33. Zhou, F. P., Lydon, F. D., and Barr, B. I. G., (1995) "Effect of coarse aggregate on elastic modulus and compressive strength of high performance concrete" *Cement and Concrete Research*, Volume 25, No. 1, pp. 177-186.

Appendix A

List of bridges selected after Preliminary Review for Phase I evaluation

	BIN	28DayStrengthPour1	28DayStrengthPour2	DeckCracks	Description Cracks	Girder Spacing	Casting Date	Comments	
1	1000440	6525		Yes	Daigonal, Long	10.8	11/8/2000	Deck Survey DOT form show mainly longitudinal cracks. Positions of these cracks are well detailed. However, this report does not include any plan of superstructure slab, sidewalk reinforcement, girder elevation and details, or transverse section and details. Although, we may assume that these cracks are produced by negative bending moments close to girders.	
2	1000450	7194		No	no cracks	8.04	9/7/2001	Deck Survey DOT form informs the lack of cracks on this bridge deck. However, DOT Region 7 Cracked Decks Access document informs about the existence in the left side - 2/3 of the dist to pier of 3 short cracks about 1 ft long near fascia, and on the right side of one crack at the bridge rail join about 4 ft long and .003-.005 in wide.	
3	1000871	7310		No	no cracks	9.08	8/21/1999	**NO Deck Survey DOT form provided.**	Copy will be sent
4	1000872	6320		No	no cracks	8.65	6/11/1999	**Deck Survey DOT form does not show any crack for this deck.**	TRUE
5	1008840	6980		Yes	Longitudinal Crack	9.02	10/12/1999	Longitudinal cracks, there is not information about their approximate position in the deck. However, from Deck Survey DOT form we may assume that these cracks are produced by negative bending moments close to girders.	
6	1018970	6830		Yes	Transverse and Long. Cracks	--	10/24/1997	Pictures from Deck Survey DOT form show transverse cracks. One of these pictures also illustrates longitudinal cracks; we may assume that these longitudinal cracks may be produced by negative bending moments close to girders. DOT document for this bridge does not include any plan of superstructure slab, sidewalk reinforcement, girder elevation and details, or transverse section and details.	This is a prestressed Box beam bridge and should not be included.
7	1021350	6860		Yes	transverse	9.51	9/4/1997	Several transverse cracks along the length of the deck, there is not information about their approximate position in the deck. Pictures from Deck Survey DOT form show a severe transverse crack parallel to a deck joint. Deck Survey DOT from informs that the cause of this crack was the inclusion of the header pour with the approach slab.	
8	1023970	7295		Yes	Transverse Cracks	8.63	7/2/1998	Transverse cracks, they are spaced between 1 to 3 meters a long the deck; however there is not information about their approximate position in the deck.	
9	1044890	5990		No	Rough Surface Texture	7	7/17/1997	Pictures from Deck Survey DOT form show rough surface texture. This report also suggests that the cause of this rough surface texture was a deficient finish of this bridge. DOT form also informs that by the inspection day (5/8/01) there were no cracks on the deck.	
10	3335750	6880		No	no cracks	--	5/27/1999	**Deck Survey DOT form does not show any crack for this deck.**	
11	3337950	7860		Yes	Longitudinal Cracks	--	10/2/1997	Deck Survey DOT form informs of a full length longitudinal crack near the center line of the right travel line and longitudinal cracks up to 3 m. long and the beginning and end of left travel lane. Positions of these cracks are not well detailed. We may assume that these cracks are produced by negative bending moments close to girders. This report does not include any plan of superstructure slab, sidewalk reinforcement, girder elevation and details, or transverse section and details.	This is a prestressed Box beam bridge and should not be included.
12	3338130	5140		Yes	Longitudinal Crack	--	8/24/1999	Pictures from Deck Survey DOT form show longitudinal cracks. However, there is not either information about their approximate position in the deck or bridge plans of superstructure slab, sidewalk reinforcement, girder elevation and details, or transverse section and details. Although, we may assume that these cracks are produced by negative bending moments close to girders.	This is a prestressed Box beam bridge and should not be included.
13	3338480	5510		No	no cracks	6.75	7/25/1997	**Deck Survey DOT form does not show any crack for this deck.**	Only very minor mapcracking - not considered significant.
14	3338700	4320		No	no cracks	7.2	8/16/1999	**Deck Survey DOT form show two transverse cracks, although this deck is evaluated with a frequency rating number 7 (no cracks)**	These cracks were so small that I considered them insignificant in the rating
15	3338710	6613		No		6.89	9/28/2001	**NO Deck Survey DOT form provided.**	I looked at these two bridges after most of the rest - and entered the information directly into the databse - therefore no forms
16	3338720	5511		No	none	7.1	6/29/2001	**NO Deck Survey DOT form provided.**	I looked at these two bridges after most of the rest - and entered the information directly into the databse - therefore no forms
17	3340510	6120		No	no cracks	8.53	10/15/1998	**Deck Survey DOT form show longitudinal and diagonal cracks, although this deck is evaluated with a frequency rating number 7 (no cracks)**	These cracks were so small that I considered them insignificant in the rating
18	3340810	4710	4980	Yes	Longitudinal Cracks	--	10/20/1995	2 Spans bridge, however DOT Region7CrackedDecks Access file classifies this bridge as a single span bridge	This is a prestressed Box beam bridge and should not be included.
19	3369170	6010		Yes	Longitudinal Crack	6.23	9/17/1997	Longitudinal cracks, information about their approximate position in the deck enable us to assume that these longitudinal cracks were produced by negative bending moments close to girders.	

Appendix B

Data calculated from the image analysis of cracked cores is presented below. The data was collected by optically slicing the specimen in 1in slices and collecting the information from each slice. The information on the number of aggregates through which the crack passes through, the number of aggregates that the crack passes around and the average crack width in each slice of each specimen are presented in the tables below.

BIN 1000440: *Type of cracking Longitudinal crack*

Core #5
Side A
Length crack (in)   4.034

Depth (in)	# of aggregate that crack pass **through**	# of aggregate that crack pass **around**	Average crack **thickness** (in)
0 – 1	-	3	-
1 – 2	-	2	-
2 – 3	-	1	-
3 – 4	-	1	-

Side B
Length crack (in)   3.013

Depth (in)	# of aggregate that crack pass **through**	# of aggregate that crack pass **around**	Average crack **thickness** (in)
0 – 1	-	1	-
1 – 2	-	1	-
2 – 3	-	1	-

Core #8
Side A
Length crack (in)   5.529

Depth (in)	# of aggregate that crack pass **through**	# of aggregate that crack pass **around**	Average crack **thickness** (in)
0 – 1	-	2	0.04800
1 – 2	-	1	0.02800
2 – 3	-	3	0.04000
3 – 4	-	1	0.04000
4 – 5	-	3	0.04000
5 – 6	-	1	0.00800

Side B
Length crack (in)   4.472

Depth (in)	# of aggregate that crack pass **through**	# of aggregate that crack pass **around**	Average crack **thickness** (in)
0 – 1	-	2	0.01600
1 – 2	-	1	0.01600
2 – 3	-	1	0.01600
3 – 4	-	2	0.01600
4 – 5	-	-	0.00800

BIN 10008840

Type of cracking: *Longitudinal crack*

Core #5
Side A
Length crack (in)   7.039

Depth (in)	# of aggregate that crack pass **through**	# of aggregate that crack pass **around**	Average crack thickness (in)
0 - 1	-	-	0.02066
1 - 2	-	4	0.02066
2 - 3	-	3	0.01240
3 - 4	-	1	0.00826
4 - 5	-	-	0.01240
5 - 6	-	3	0.00826
6 - 7	-	-	0.00826
7 - 8	-	2	0.00826

Side B
Length crack (in)   8.120

Depth (in)	# of aggregate that crack pass **through**	# of aggregate that crack pass **around**	Average crack thickness (in)
0 - 1	-	1	0.04132
1 - 2	-	3	0.02342
2 - 3	-	3	0.00826
3 - 4	-	1	0.00826
4 - 5	-	-	0.00826
5 - 6	-	-	0.01240
6 - 7	-	2	0.01240
7 - 8	-	1	0.01240

Core #6
Side A
Length crack (in)   2.529

Depth (in)	# of aggregate that crack pass **through**	# of aggregate that crack pass **around**	Average crack thickness (in)
0 - 1	-	4	0.00820
1 - 2	-	-	0.00820
2 - 3	-	1	0.00820

Side B
Length crack (in)   4.074

Depth (in)	# of aggregate that crack pass **through**	# of aggregate that crack pass **around**	Average crack thickness (in)
0 - 1	-	-	0.00820

BIN 3369170

Type of Cracking: _Longitudinal crack_

Core #1

Side A

Length crack (in) = 1.232

Depth (in)	# of aggregate that crack pass **through**	# of aggregate that crack pass **around**	Average crack **thickness** (in)
0 - 1	-	-	0.00848

Side B

Length crack (in) = 1.162

Depth (in)	# of aggregate that crack pass **through**	# of aggregate that crack pass **around**	Average crack **thickness** (in)
0 - 1	-	2	0.00848
1 - 2	-	1	0.00848

BIN 1021350

Type of crack: *Transverse crack*

Core #1
Side A
Length crack (in)   6.565

Depth (in)	# of aggregate that crack pass **through**	# of aggregate that crack pass **around**	Average crack **thickness** (in)
0 - 1	-	3	0.01653
1 - 2	1	-	0.01033
2 - 3	-	-	0.01240
3 - 4	-	-	0.00826
4 - 5	1	-	0.01033

Side B
Length crack (in)   2.599

Depth (in)	# of aggregate that crack pass **through**	# of aggregate that crack pass **around**	Average crack **thickness** (in)
0 - 1	-	2	0.03306
1 - 2	-	2	0.01653
2 - 3	-	2	0.00826

Core #2
Side A
Length crack (in)   6.404

Depth (in)	# of aggregate that crack pass **through**	# of aggregate that crack pass **around**	Average crack **thickness** (in)
0 - 1	-	2	0.03279
1 - 2	-	-	0.01639
2 - 3	1	-	0.02459
3 - 4	1	-	0.00820
4 - 5	-	2	0.00820
5 - 6	1	-	0.016393

Side B
Length crack (in)   4.074

Depth (in)	# of aggregate that crack pass **through**	# of aggregate that crack pass **around**	Average crack **thickness** (in)
0 - 1	-	3	0.016393
1 - 2	-	1	0.016393
2 - 3	-	1	0.012295
3 - 4	-	2	0.016393
4 - 5	-	2	0.016393

BIN 1023970

Type of cracking: *<u>Transverse crack</u>*

Core #3

Side A

Length crack (in)   8.518

Depth (in)	# of aggregate that crack pass **through**	# of aggregate that crack pass **around**	Average crack **thickness** (in)
0 - 1	-	1	0.02066
1 - 2	-	3	0.02066
2 - 3	-	1	0.01446
3 - 4	-	-	0.00826
4 - 5	1	-	0.00826
5 - 6	1	1	0.01240
6 - 7	-	1	0.01240
7 - 8	-	1	0.00826

Side B

Length crack (in)   7.161

Depth (in)	# of aggregate that crack pass **through**	# of aggregate that crack pass **around**	Average crack **thickness** (in)
0 - 1	-	1	0.04132
1 - 2	-	1	0.00826
2 - 3	-	1	0.00826
3 - 4	-	1	0.00826
4 - 5	-	1	0.00826
5 - 6	-	2	0.00826
6 - 7	-	1	0.00826
7 - 8	-	1	0.00826

Core #4

Side A

Length crack (in)   7.776

Depth (in)	# of aggregate that crack pass **through**	# of aggregate that crack pass **around**	Average crack **thickness** (in)
0 - 1	-	1	0.02479
1 - 2	-	2	0.02479
2 - 3	-	2	0.02479
3 - 4	-	2	0.02479
4 - 5	-	1	0.01653
5 - 6	1	-	0.00826
6 - 7	1	-	0.00826
7 - 8	-	1	0.00826

Side B

Length crack (in)   8.410

Depth (in)	# of aggregate that crack pass **through**	# of aggregate that crack pass **around**	Average crack **thickness** (in)
0 - 1	-	1	0.03306
1 - 2	-	1	0.03306
2 - 3	-	1	0.020661
3 - 4	-	2	0.012397
4 - 5	2	-	0.016529
5 - 6	-	-	0.016529
6 - 7	1	-	0.016529
7 - 8	-	-	0.008264

Appendix C

Data obtained from the compression, tension and pulse velocity tests using specimens prepared form cores obtained from the uncracked areas of the bridge are given below.

BIN1000440

Compressive Strength

Core #	L average (in)	D average (in)	L/D	ASTM C39 correction factor	P (kips)	$f_c^{\prime}$ (psi)
1	3.56	3.95	0.90	0.83	77.15	5250.07
2	4.10	3.95	1.04	0.88	87.18	6273.39
3	4.18	3.98	1.05	0.89	91.19	6509.68
4	3.95	3.99	0.99	0.87	91.85	6368.59
6	4.19	3.95	1.06	0.89	77.63	5627.14
7	4.16	3.93	1.06	0.89	62.44	4584.41

average **5768.88**

Compressive Strength specimens with rebars

Core #	L average (in)	D average (in)	L/D	ASTM C39 correction factor	P (kips)	fc (psi)
3	4.64	3.98	1.17	0.91	78.63	5793.31
4	4.92	3.99	1.23	0.93	70.70	5241.90

average 5517.60

Split Tension Tests

Core #	L average (in)	D average (in)	L/D	P (kips)	ft'(psi)
1	2.40	3.95	0.61	9.28	623.51
6	2.56	3.95	0.65	10.39	653.23
7	2.31	3.93	0.59	10.15	711.56

average **662.77**

Ultrasonic Pulse-Velocity

Core #	L (in)	Time average (ms)	Ultrasonic pulse velocity (ft/s)
1	2.38	15.18	13070.93
3	4.64	29.16	13251.60
6	2.66	14.68	15082.88
7	2.28	14.88	12763.22
		Average	**13542.16**

Static Modulus (using ASTM C 469)

Core #	E (psi)
3	3.67644E+06
4	5.51539E+06

Core #3

y = 3.67334E+06x + 1.02721E+02
R^2 = 9.96989E-01

Stress (psi)

Strain (in/in)

Core #4

y = 5.51272E+06x + 4.90064E+02
R^2 = 9.99455E-01

Stress (psi)

Strain (in/in)
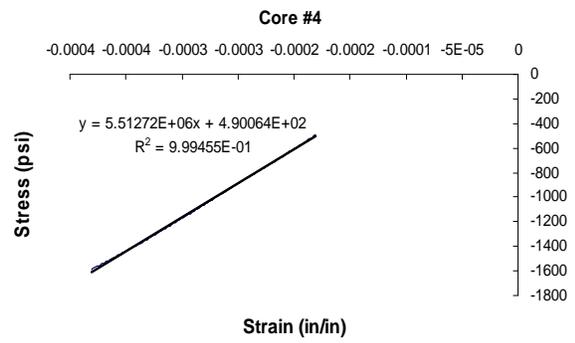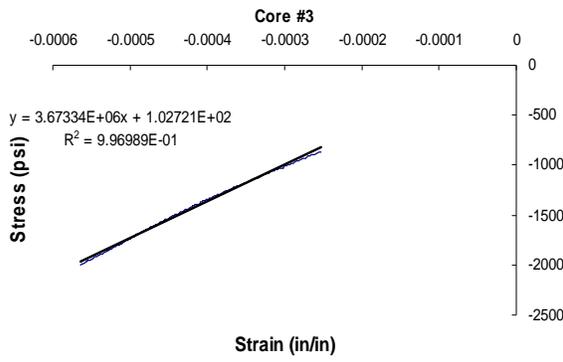
BIN1008840

Compressive Strength

Core #	L average (in)	D average (in)	L/D	ASTM C39 correction factor	P (kips)	*fc'* (psi)
1	2.77	3.94	0.70	0.73	87.47	5256.00
2	3.09	3.88	0.80	0.79	67.83	4521.25
3	2.91	3.94	0.74	0.75	90.85	5619.27
4	2.84	3.94	0.72	0.74	85.58	5227.66
					average	**5156.04**

Compressive Strength specimens with rebars

Core #	L average (in)	D average (in)	L/D	ASTM C39 correction factor	P (kips)	fc (psi)
2	4.89	3.88	1.26	0.93	91.12	7200.98
					average	7200.98

Split Tension Tests

Core #	L average (in)	D average (in)	L/D	P (kips)	ft'(psi)
1	2.16	3.94	0.55	8.82	661.55
3	2.06	3.94	0.52	9.54	748.08
4	2.63	3.94	0.67	11.95	736.24
				average	**715.29**

Ultrasonic Pulse-Velocity

Core #	L (in)	Time average (ms)	Ultrasonic pulse velocity (ft/s)
1	3.09	6.50	15596.61
2	12.40	26.54	15328.72
3	6.08	12.96	15391.59
4	3.50	7.24	15860.41
		average	**15544.33**

BIN3369170

Compressive Strength

Core #	L average (in)	D average (in)	L/D	ASTM C39 correction factor	P (kips)	fc (psi)
2	6.71	3.98	1.69	0.97	85.81	6741.45
3	3.35	3.99	0.84	0.81	115.36	7462.83
6	4.39	3.98	1.10	0.90	71.80	5190.45
7	4.63	3.99	1.16	0.91	84.78	6206.51
					average	**6400.31**

Compressive Strength specimens with rebars

Core #	L average (in)	D average (in)	L/D	ASTM C39 correction factor	P (kips)	fc (psi)
4	5.47	3.98	1.37	0.95	74.85	5714.69
5	5.54	3.99	1.39	0.95	67.14	5095.27
					average	5404.98

Split Tension Tests

Core #	L average (in)	D average (in)	L/D	P (kips)	ft'(psi)
3	3.16	3.99	0.79	13.76	695.56
4	2.93	3.98	0.74	13.51	738.88
5	2.21	3.99	0.55	10.07	727.70
6	2.06	3.98	0.52	9.09	705.88
				average	**717.00**

Ultrasonic Pulse-Velocity

Core #	L (in)	Time average (ms)	Ultrasonic pulse velocity (ft/s)
3	3.21	15.58	17174.80
4	3.01	14.96	16739.08
5	2.17	12.22	14764.05
6	2.07	11.84	14555.18
		average	**15808.28**

Static Modulus (using ASTM C 469)

Core #	E (psi)
4	3.35535E+06
5	3.46480E+06

Core 4

$y = 3.356387E+06x + 2.719674E+02$

$R^2 = 9.987026E-01$

Stress (psi)

Strain (in/in)

Core 5

$y = 3.451191E+06x + 1.086125E+02$

$R^2 = 9.987328E-01$

Stress (psi)

Strain (in/in)

106
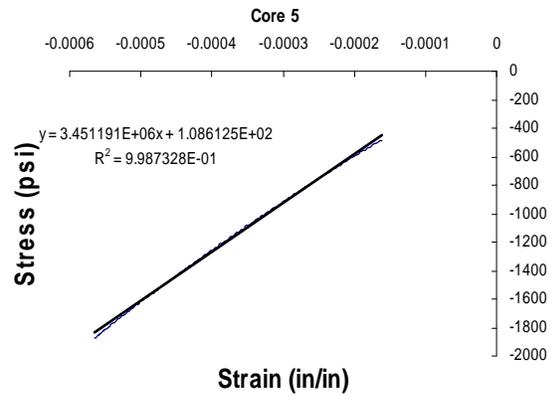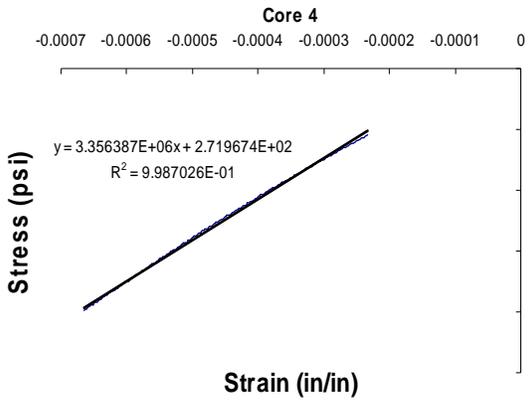
BIN1021350

Compressive Strength

Core #	L average (in)	D average (in)	L/D	ASTM C39 correction factor	P (kips)	*fc'* (psi)
3	3.54	3.93	0.90	0.83	112.31	7740.47
5	3.70	3.96	0.94	0.85	107.52	7413.99
6	6.37	3.96	1.61	0.97	74.94	5909.77
					average	**7021.41**

Compressive Strength specimens with rebars

Core #	L average (in)	D average (in)	L/D	ASTM C39 correction factor	P (kips)	fc (psi)
4	5.92	3.95	1.50	0.96	83.98	6577.23
6	6.37	3.95	1.61	0.97	74.94	5925.70
					average	6251.46

Split Tension Tests

Core #	L average (in)	D average (in)	L/D	P (kips)	ft(psi)
3	1.86	3.93	0.47	7.92	692.12
4	2.32	3.96	0.59	10.93	757.40
5	1.84	3.96	0.47	8.47	739.55
				average	**729.69**

Ultrasonic Pulse-Velocity

Core #	L (in)	Time average (ms)	Ultrasonic pulse velocity (ft/s)
3	2.08	12.00	14409.72
4	2.35	11.96	16339.19
5	0.84	6.06	11496.15
		average	**14081.69**

Static Modulus (using ASTM C 469)

Core #	E (psi)
4	4.24712E+06
6	2.91596E+06

Core 4

$y = 4.26763E+06x - 6.72714E+02$
$R^2 = 9.95049E-01$

Core 6

$y = 2.924989E+06x - 1.293296E+02$
$R^2 = 9.999264E-01$
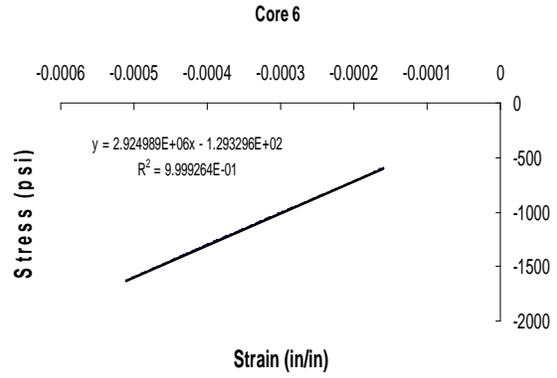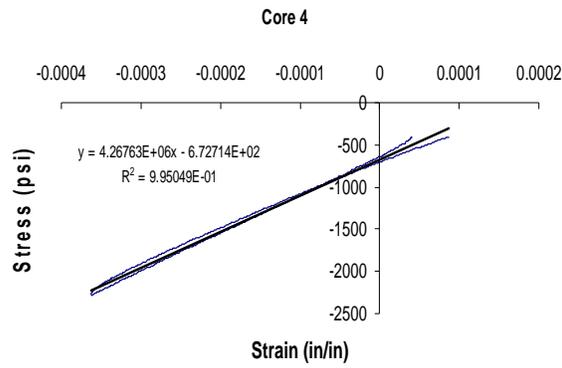
BIN1023970

Compressive Strength

Core #	L average (in)	D average (in)	L/D	ASTM C39 correction factor	P (kips)	*fc'* (psi)
1	2.83	3.98	0.71	0.74	119.63	7112.30
2	2.98	3.98	0.75	0.76	106.38	6507.37
5	3.15	3.98	0.79	0.78	68.81	4341.93
6	3.17	3.95	0.80	0.79	99.01	6367.53
					average	**6082.28**

Compressive Strength specimens with rebars

Core #	L average (in)	D average (in)	L/D	ASTM C39 correction factor	P (kips)	fc (psi)
6	4.62	3.95	1.17	0.91	85.39	6375.03
					average	6375.03

Split Tension Tests

Core #	L average (in)	D average (in)	L/D	P (kips)	ft'(psi)
1	2.43	3.98	0.61	9.88	652.22
2	2.42	3.98	0.61	9.39	621.44
5	1.86	3.95	0.47	8.78	759.56
				average	**677**.74

Ultrasonic Pulse-Velocity

Core #	L (in)	Time average (ms)	Ultrasonic pulse velocity (ft/s)
1	2.47	12.96	15862.91
2	2.43	13.30	15225.56
5	1.83	10.96	13914.23
6	4.60	29.98	12791.86
		average	**14448**.64

Static Modulus (using ASTM C 469

Core #	E (psi)
6	3.31534E+06

Core 6

$y = 3.31342E+06x - 3.09212E+02$

$R^2 = 9.99842E-01$

Stress (psi)

Strain (in/in)

-0.0005 -0.0004 -0.0003 -0.0002 -0.0001 0

0
-200
-400
-600
-800
-1000
-1200
-1400
-1600
-1800
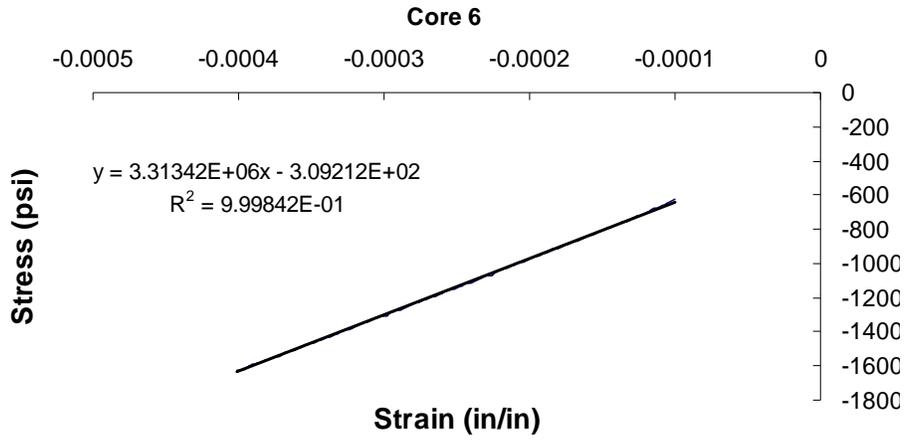
Appendix D: Installation of Sensors

DESCRIPTION

This appendix provides details on installation of strain and temperature monitoring sensors for reinforced concrete bridge decks, connection of the sensors with a data acquisition system, programming of the data acquisition system for periodic data collection and storage and installation of the data acquisition system. Sensors shall be attached to the rebars in the bridge deck and to the bottom surface of the top flange of the steel girders for monitoring strain and temperature.

The instrumentation for each bridge deck shall comprise of the following: (a) two embedded thermo couples placed inside the bridge deck; and (b) two thermocouples attached to the steel girders. In addition, two bridge decks will be instrumented using vibrating wire strain gages. The instrumentation when using strain gages shall comprise of the following: (a) two embedded vibrating wire strain gages placed in the bridge deck; and (b) two surface-mounted vibrating wire gages attached to the flanges of the steel girders. The details of placement and location of each of the sensors is given below.

Embedded thermocouples: Two thermocouples shall be located in the longitudinal direction (direction of traffic) approximately at the mid span location and close to the middle of the entire width of the bridge (as shown in Figure I.1). The gage located close to the top/bottom surface of the bridge deck shall be in the same plane as the top/bottom layer of steel reinforcement. The details for installing these sensors are provided in the next section. The details for installing these sensors are provided in the next section.

Thermocouples attached to steel girders: One surface mounted wire gages shall be attached to the bottom surface of the top flange of the steel girders in the longitudinal direction (direction of traffic) approximately at the mid span location and close to the middle of the entire width of the bridge. The strain gage attached to the steel girder shall be used to measure temperature changes on the steel girder. A second gage shall be attached to the girder to allow for monitoring the ambient air temperature.

Embedded vibrating wire gages: Two embedded vibrating wire gages shall be located in the longitudinal direction (direction of traffic) approximately at the mid span location and close to the middle of the entire width of the bridge (as shown in Figure I.1). The gage located close to the top/bottom surface of the bridge deck shall be in the same plane as the top/bottom layer of steel reinforcement. The details for installing these sensors are provided in the next section. In addition, a third embedded vibrating wire gage shall be in the transverse direction, located in-plane with the other two gages (shown in Figure I.1)

Surface mounted vibrating wire gages: Two surface mounted wire gages shall be attached to the steel girder. One gage shall be attached to the bottom surface of the top flange of the steel girders (as shown in Figure 2) in the longitudinal direction (direction of traffic) approximately at the mid span location and close to the middle of the entire width of the bridge (as shown in Figure 1). The second gage shall be attached to the bottom flange. The strain gages will be spot welded to the steel girders.

The data collection units for the strain gages and the thermocouples shall be programmed to collect and store data at 5 minute intervals. The date and time of each data sample shall also be stored.

CONSTRUCTION DETAILS

This work will consist of the following: attaching sensors to the rebars and the girders; connecting wires with the sensors; attaching wires to the bundled cable; and routing wires through the structure up to the data box.

The following sensors/probes shall be attached to the rebar prior to placing concrete.
>   Thermocouple Sensor
>   Vibrating-wire Strain Gage Sensor

The sensors shall be installed prior to pouring concrete as per the details provided below. It shall be ensured that during vibration of concrete, the vibrator wand shall not be used close to any of the sensors.

Installation of thermocouple sensor

Thermocouple Sensor Installation and Connection**. The thermocouple sensor installation shall comprise of attaching the thermocouple sensor and the lead-out wire to the rebar. The thermocouple sensor comprises of the thermocouple probe and the lead out wire. The thermocouple sensor lead-out wire shall be attached to the rebar using Nylon or plastic ties spaced no more than 0.3 m apart. The sensor shall be placed such that it is not in direct contact with the rebar.

Grouping Wires. A group of lead-out wires shall be routed to a common place as near as possible to the probe locations to simplify the wiring effort. All the wires shall be cut at the same point and insulation 6 mm in length shall be stripped off. The wire strands of the bundled cables shall also cut at one point and the insulation stripped off. The ends of the lead-out wires shall be connected to each of the bundled cable wires using a butt-crimp connector.

Numbering/Color Coding**. The number of each lead-out wire shall be recorded against the color of the bundled cable wire. Each connection shall be sealed with shrink-wrapped tubing, placed over the wires prior to using the butt-crimp connector. Finally, the joint shall be wrapped with liquid electric tape.

Installation of Strain gage sensor

The strain gage sensor comprises of the strain gage probe and the lead out wire. The strain gage sensor installation shall comprise of placing the strain gage probe as shown in Figure I.3 and attaching the lead-out wire to the rebar. The soft iron tie wire, the kind normally used for tying rebars shall be used to position the strain gage sensor as shown in Figure I.3. The tie wire shall be twisted 2 times around the body of the strain gage sensor at two locations about 3cm from the gage ends. The gage shall be positioned between the rebar and the wire ends shall be twisted twice around the rebar. The wires holding the gage shall be tightened and the gage shall be oriented such that it is parallel to the rebars. The strain gage sensor lead-out wire shall be attached to the rebar using Nylon or plastic ties. The sensor shall be placed such that it is not in direct contact with the rebar spaced no more than 0.3 m (1foot) apart. A single cable from each strain gage sensor unit shall be routed to the data box. During vibration, the vibrator wand shall not be used down onto the strain gage unit.
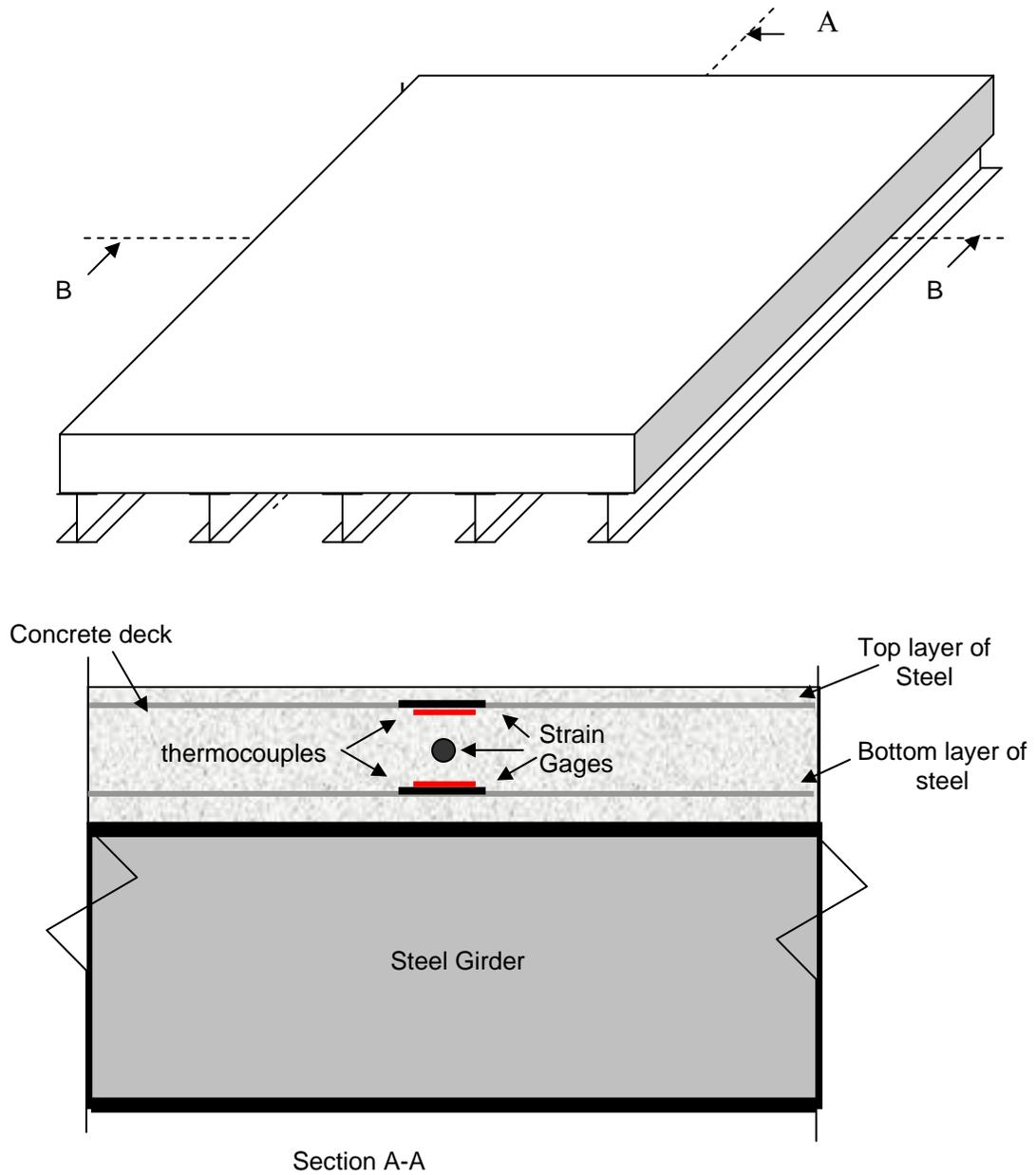
Figure I.1: The location and placement of the embedded vibrating wire strain gages.
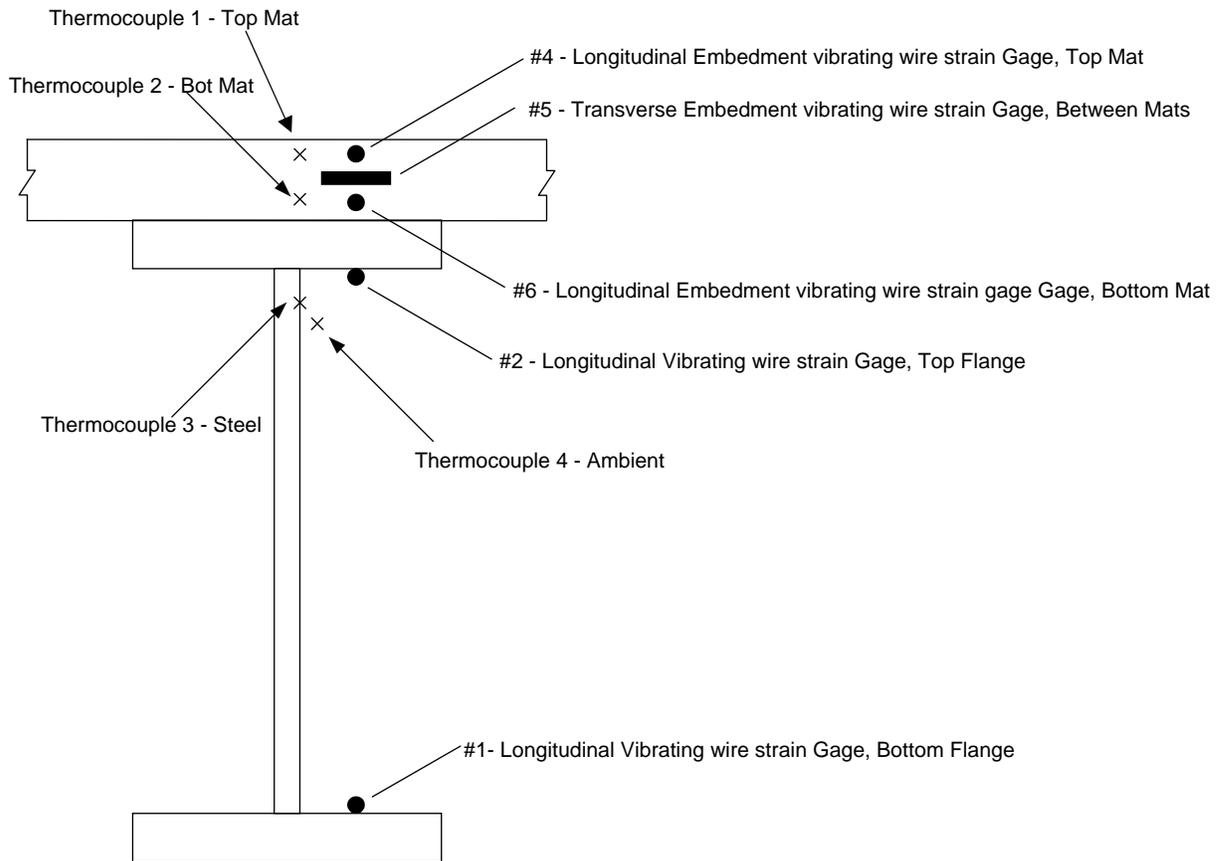
Figure I.2: Placement of surface mounted vibrating wire strain gages along section B-B.
(Courtesy Jon. Kunin, Research Group, NYSDOT)
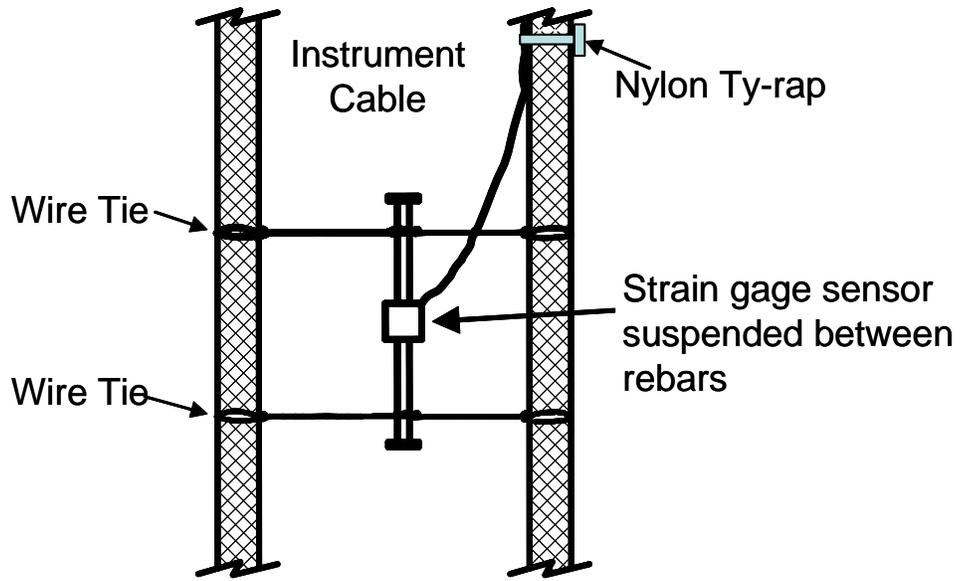
Figure I.3: Installation of the Strain gage sensor